Command Generation for Tethered Satellite Systems

A Thesis
Presented to
The Academic Faculty

by

Michael J. Robertson

In Partial Fulfillment
of the Requirements for the Degree
Doctor of Philosophy

George W. Woodruff School of Mechanical Engineering
Georgia Institute of Technology
April 14, 2005

Command Generation for Tethered Satellite Systems

Approved by:

Professor William E. Singhose, Advisor
School of Mechanical Engineering
Georgia Institute of Technology

Professor John Olds
School of Aerospace Engineering
Georgia Institute of Technology

Professor Ye-Hwa Chen
School of Mechanical Engineering
Georgia Institute of Technology

Dr. Arun Banerjee*Lockheed Martin*

Professor Imme Ebert-Uphoff
School of Mechanical Engineering
Georgia Institute of Technology

April 14, 2005

Date Approved _____

To everyone who has helped me along the way...

ACKNOWLEDGEMENTS

I would like to begin be thanking my advisor, Dr. William Singhose, and my committee. I would also like to thank the GEM Consortium (GEM Ph.D. Fellowship/ Ford Motor Company), Georgia Tech's Center for Enhancement of Teaching and Learning (STEP Fellowship), and NASA's Marshall Space Flight Center (Graduate Student Research Program) for providing my with funding throughout this endeavor. Finally, I would like to acknowledge all the wonderful lab mates and guest researchers I have had the opportunity to interact with, and learn from, throughout the years.

TABLE OF CONTENTS

LIST OF TABLES

LIST OF FIGURES

SUMMARY

Command generation is a process by which input commands are constructed or modified such that the system's response adheres to a set of desired performance specifications. Previously, a variety of command generation techniques such as input shaping have been used to reduce residual vibration, limit transient deflection, conserve fuel or adhere to numerous other performance specifications or performance measures.

This dissertation addresses key issues regarding the application of command generation techniques to tethered satellite systems. The three primary objectives of this research are as follows: 1) create analytically commands that will limit the deflection of flexible systems 2) combine command generation and feedback control to reduce the retrieval time of tethered satellites, and 3) develop command generation techniques for spinning tether systems.

More specifically, the proposed research addresses six specific aspects of command generation for tethered satellites systems: 1) creation of command shapers that can limit the trajectory tracking error for a mass under PD control to a pre-specified limit in real time 2) creation of commands analytically that can limit the transient deflection of a system with one rigid-body and one flexible mode during rest-to-rest maneuvers 3) command generation for a 2-D model of earth-pointing tethered satellites without tether flexibility, 4) command generation for a 2-D model of earth-pointing tethered satellites to reduce tether retrieval time and reduce swing angle, 5) command generation for a 3-D model of earth-pointing tethered satellites without tether flexibility, and 6) command generation for improved spin-up of spinning tethered satellite systems. The proposed research is anticipated to advance the state-of-the-art in the field of command generation for tethered satellite systems and will potentially yield improvements in trajectory tracking, retrieval time and final angular velocity in a number of practical satellite and tether applications.

CHAPTER I

INTRODUCTION

Recently, there has been a resurgence of interest in the exploration of space. The current administration has expressed the desire to return to the moon and is advocating a manned mission to Mars. The European Space Agency, the Japanese Space Agency and China have also expressed interest in missions to the Moon. Current and future missions can have scientific, commercial or military applications. While the potential benefits of space exploration are seemingly boundless, there are many major problems yet to be overcome. Some of the major problems this dissertation addresses include: reducing launch costs, extending the useful life of satellites, de-orbiting the satellite at the end of its mission, the precise maneuvering and control of satellites during their missions and reducing the negative physiological effects of extended periods in near zero-gravity environments for humans. Tethered satellite systems have been proposed to solve some of these problems. This dissertation intends to improve the state-of-the-art in satellite control in three major areas: deflection-limited rest-to-rest moves of flexible satellites, combined command shaping and feedback controller gains for reduced tether retrieval time and swing angle for nadir-pointing satellites, and command shaping retrieval profile used to spin-up spinning tethered satellite systems.

1.1 Tethered Satellite Systems

There is a significant amount of research in the area of controlling tethered satellite systems [77, 78, 69, 50, 41, 34, 29, 19, 10, 3]. Such systems can be used to conduct ionospheric [23, 24, 7] or gravity gradient experiments [23], carry out radio astronomy measurements, deploy or retrieve satellites [38], etc. While many of the initial applications were Shuttle-based [4, 49], space platform-based applications [17, 28, 39, 50] have also received attention. Electrodynamic tethers can be used to reboost, de-orbit, or maneuver satellites. Some of

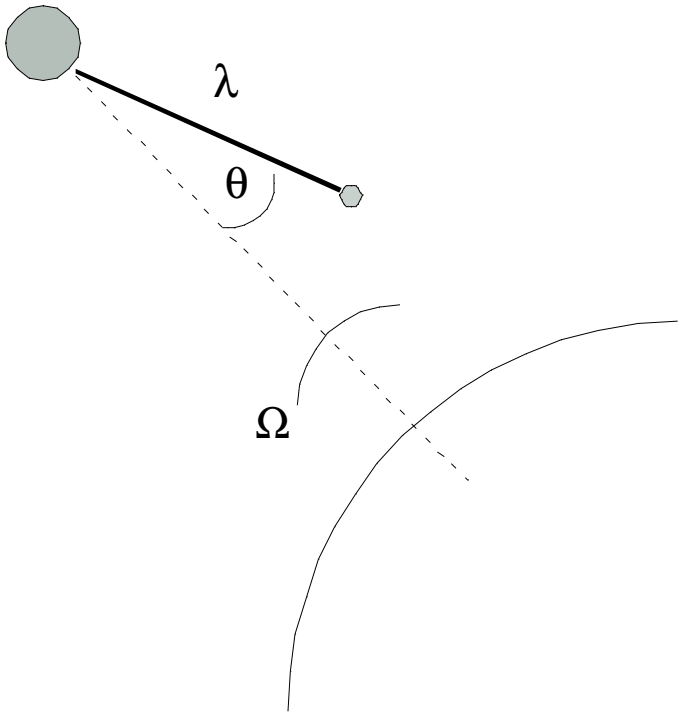

Figure 1: Nadir-Pointing Tethered Satellite System.

the most promising applications are in the area of spinning tethered satellite systems. These systems can be used to create artificial gravity fields or, when combined with electrodynamic tethers, can be used to propellantlessly boost satellites to higher orbits.

1.1.1 Nadir-pointing Tethered Satellite Systems

The simplest tethered satellite systems consist of a main satellite and subsatellite in nadir- or earth-pointing orbit. A sketch of this configuration is given in Figure 1. Often the main satellite's mass is assumed to be much greater than the subsatellite's mass. Under this assumption, the center of gravity of the system is not significantly affected by the deployment or retrieval of the subsatellite. To further simplify the model, the tether is often taken to be massless and rigid. Even using this greatly simplified model, the dynamics of the tethered satellite system are extremely complicated. The resulting equations of motion are highly nonlinear with coupling between the in-plane and out-of-plane swing angles [38].

Tethered satellite control is divided into three regimes: deployment, station-keeping and retrieval. The research indicates that deployment is stable as long as a critical speed is not

exceeded, stationkeeping is marginally stable and retrieval is always unstable [38]. Several researchers have investigated the dynamics and control of deployment [4, 16, 26, 32, 38, 41, 69] from both circular and elliptical orbits [56, 57]. Stationkeeping has also been well investigated [17, 30, 31]. Given the inherent instability, the majority of the effort has been in the modeling and control of the retrieval process. Control schemes such as sliding mode control [49], optimal control [18, 16, 41] and Lyapunov-based feedback controllers [16, 39, 75] have been suggested. Control schemes that incorporate the use of an endpoint thruster to increase tether tension have been shown to decrease retrieval time [3].

Researchers have also developed models to account for the tether dynamics. Models have ranged from those that exclusively account for tether flexibility [56, 48, 7], mass [45, 47], or extensibility [36] or both mass and extensibility but the tether is assumed to remain straight [3]. When the tether model includes flexibility, mass and extensibility, finite elements [17, 30] partial differential equations [26, 57, 77] and lumped parameter formulations [25, 39, 50] have been used. However, regardless of the complexity of the model, initial controller design was always completed using the simple massless, rigid, inextensible tether model. Even with this simple model, the fast tether retrieval with small swing angles is a challenging task.

1.1.2 Electrodynamic Tethered Satellite Systems

The potential uses and control challenges of electrodynamic tethers have been widely investigated. Electrodynamic tethers can provide a propellantless means of maneuvering spacecraft. Current induced in a conductive tether will interact with the earth's magnetic field to produce a force. The electrodynamic force is given by $ILXB$ where I is the current flowing through the tether, L is the length of the tether and B is the magnetic field. The more promising applications are satellite reboost [11, 76, 55], deorbit [1, 24, 15, 55] and orbital maneuvering [72]. For example, the space station is one of the most obvious candidates for electrodynamic reboost [76, 11]. This would reduce the cost of maintaining the desired orbit and the number of flights needed to replenish station's propellant. Electrodynamic de-orbit can be used to remove spent or nonfunctional satellites from Low Earth Orbit (LEO) [15].

There are four practical limits to electrodynamic tethers. First, the ionosphere is not sufficiently dense beyond LEO for any significant maneuvering. Second, achievable currents are currently only a few amperes, which result in low thrusts, so it can take many weeks to complete maneuvers. Third, the efficiency of the electrodynamic maneuvering depends on the orbital inclination. Fouth, the complex dynamics exhibited by the tether during the reboost make precise positioning can be extremely difficult.

1.1.3 Spinning Tethered Satellite Systems

In addition to nadir-pointing satellites, spinning tethered satellites have also been proposed. These satellites have a significant angular velocity about the center of mass in the orbital plane. A sketch of a typical spinning tethered satellite is shown in Figure 2. Spinning tethered satellites can be used to create artificial gravity fields [35, 36, 70] in an effort to reduce bone density loss and muscle atrophy in humans during extended missions. Spinning tethered satellites can also be used to transfer momentum between two spacecraft [14, 13, 22, 27, 46, 58]. By briefly linking a slow-moving object with a faster one, the slower object's speed may be increased as the faster moving object's momentum is transferred to it. For example, a spinning tethered satellite in LEO might snare slower moving objects and hurl them to increased speeds as shown in Figure 3.

There is a proposed system that combines an electrodynamic tether and a spinning tethered system. The Momentum Exchange/ Electrodynamic Reboost (MXER) system has been proposed to produce a propellantless boosting of payloads form a Low Earth Orbit (LEO) to a Geosynchronous Transfer Orbit (GTO) or a Trans-Lunar Injection (LTI) [20, 21, 68]. The MXER system could then use an electrodynamic reboost to restore its lost momentum. In theory, this could eliminate the need for upper-stage booster rockets and greatly reduce the cost of reaching GTO and beyond for commercial and scientific purposes.

The precise control of tethered spacecraft with flexible appendages is extremely difficult. The complexity is magnified many times when the satellite must interact with other satellites as in a momentum exchange via a tether. The Momentum Exchange Electronic Reboost Tether (MXER) concept encapsulates all of these challenging tasks. The spin-up process is

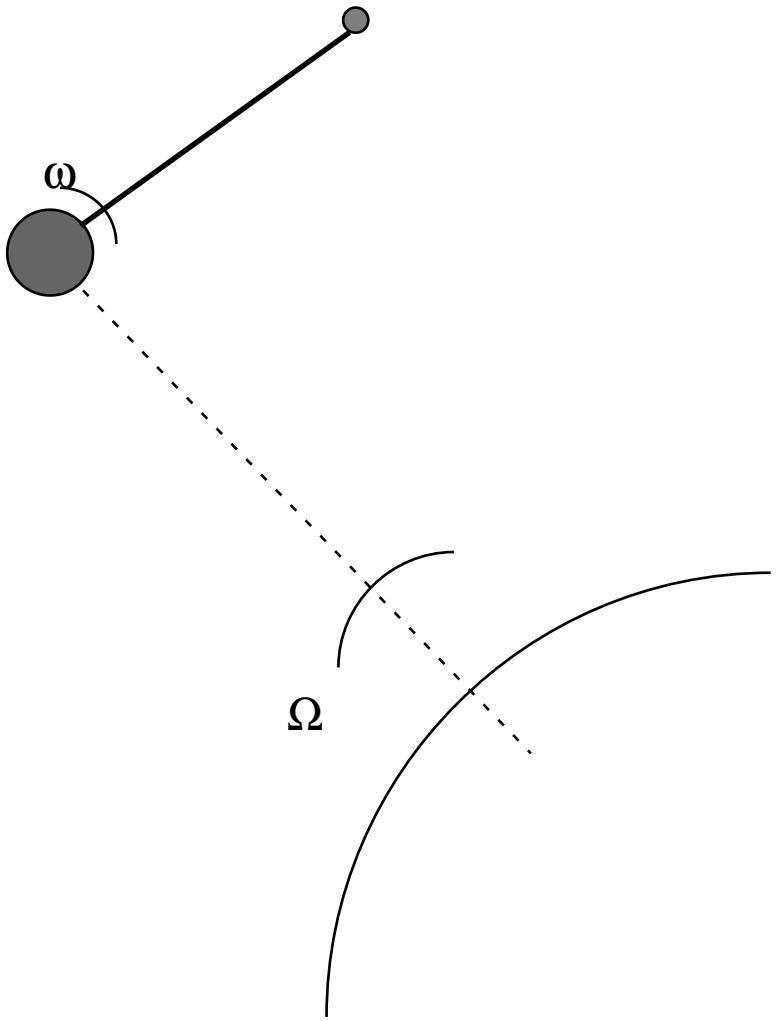

Figure 2: Spinning Tethered Satellite System.

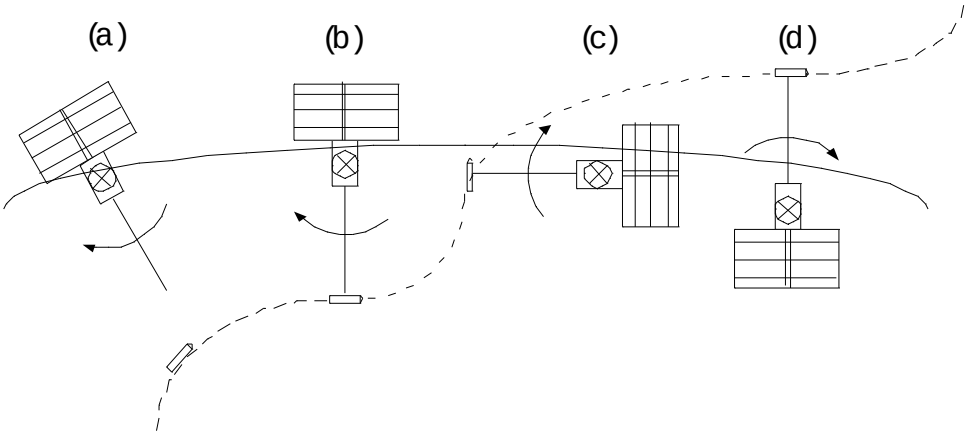

Figure 3: Momentum Exchange Using Spinning Tethered Satellite System.

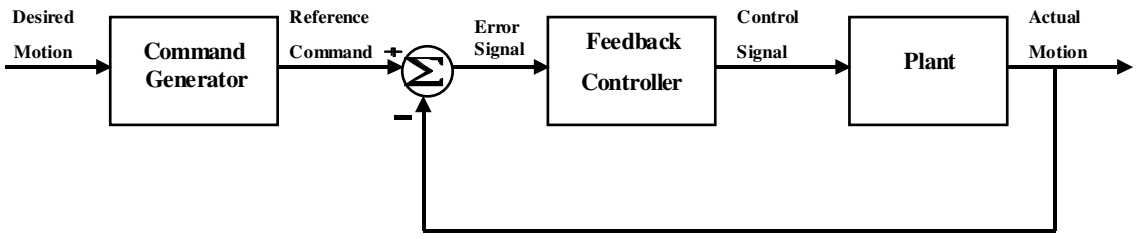

Figure 4: Diagram of Typical Control Loop.

of particular concern because the process may induce large amplitude vibrations.

1.2 Command Generation

Much work has been done to develop controllers for flexible systems. However, design and implementation of these controllers is often difficult and time consuming. Intelligent design of the command generator, often an overlooked portion of the complete control system, will aid in controlling the effects of the system's flexibility. A diagram of a typical control system is shown in Figure 4. The Plant block represents the physical system. The controller is a series of rules used to determine the action taken by the Plant. In this example, measurements of the plant's outputs are fed back to the controller and the control action is based upon the difference between the reference command and the measured output. The command generator is used to convert the desired motion to a reference command. A command generator is always present in some form, even if it is not intelligently designed. It should be noted that sensor dynamics and random disturbances are absent from this control system model. These effects have been left off for the sake of simplicity, but should always be considered when designing a control system.

The command generator is an important part of a computer-controlled system. Its function is to convert a desired trajectory, often provided by a human, to a command that the computer controller can understand. A human operator can also be the command generator, or the conversion from desired to reference trajectory may be a simple translation. For example, when steering a car, the driver is the command generator. The driver provides both the desired motion (path the car will follow) and the reference command to the control system (the steering wheel position.) An example of a simple translation is an analog to

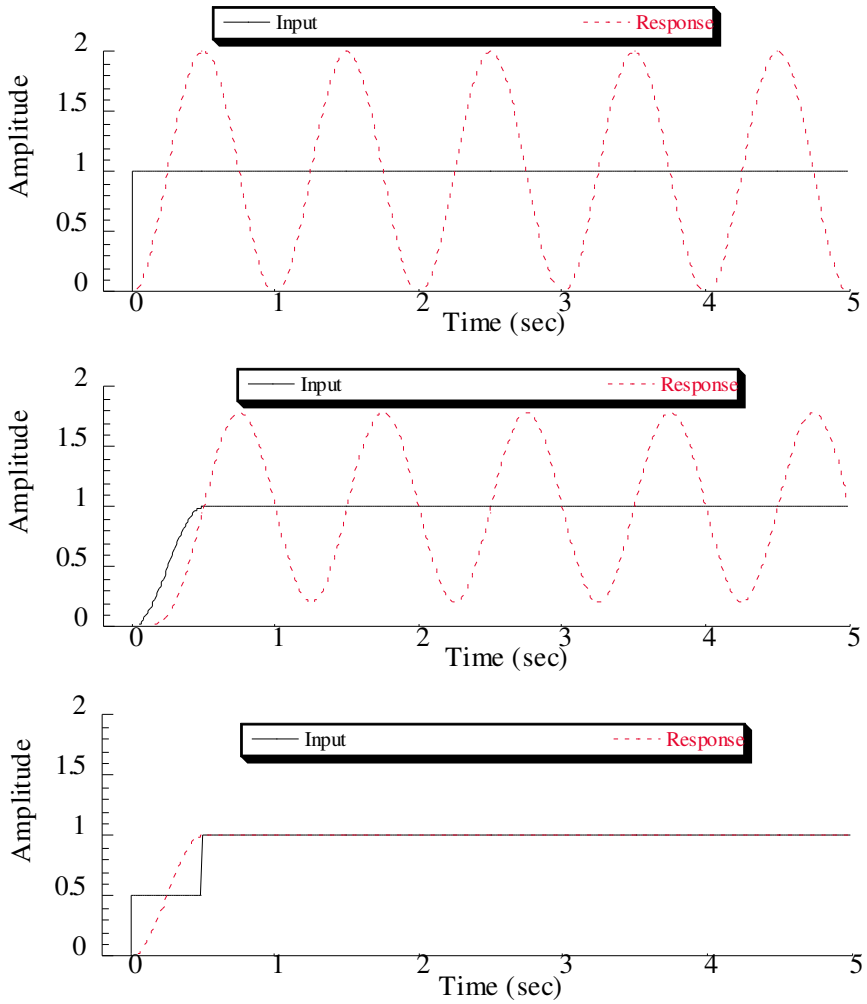

Figure 5: Response of Undamped Harmonic Oscillator.

digital conversion. These conversions are performed when a continuous desired trajectory is fed to a computer (digital) controller. In a modern "drive-by-wire" automobile, this is performed by converting an accelerator pedal position to a computer controlled throttle position.

To demonstrate the effect of the command generation on performance, consider a system that can be modeled as an undamped harmonic oscillator. The desired motion for this system is a change in position. The top graph of Figure 5 shows the system response to a step input. The system responds quickly, but a large amount of oscillation is induced. In an effort to eliminate the residual vibration, a smooth profile can be given to the system as shown by the middle graph of Figure 5. Using this command reduces the amplitude of

the oscillation by a small amount, but it increases the rise time of the system. Finally, a staircase command can be given to the system. This command consists of two equal amplitude steps with the second step delayed by half the vibration period. The staircase command eliminates the residual vibration at the expense of a small increase in the rise time. Notice that the rise time of the system is delayed by half a period of the vibration.

It is obvious from the example discussed above that the command given to the system can have a tremendous effect on the performance of the system. While we can design feedback controllers to accomplish a low-vibration move, it's derivation and implementation may be mathematically complex and require the use of sensors. In addition the feedback controller is often used to adhere to the reference command, stabilize the system and reduce the effects of disturbances. Developing these vibration-free reference commands would eliminate one design criterion for the feedback controller, thus simplifying it's design or choice of controller gains. The following section will outline how to create commands that will eliminate residual vibration and it will also detail the characteristics of these commands.

1.2.1 Input Shaping Review

Input shaping is a form of command generation that is designed to reduce *command-induced* vibration [59]. Input shaping can be implemented on any computer-controlled system with fairly well-known vibrational characteristics, such as number of modes of vibration, natural frequencies and damping ratio. Unlike traditional forms of command generation, it considers the system's natural tendency to vibrate when it develops the reference command for a system.

Input shaping is implemented by convolving a sequence of impulses, known as the input shaper, with a desired system command to produce a shaped input that is then used to drive the system. This process is demonstrated in Figure 6. The amplitudes and time locations of the impulses are determined by solving a set of constraint equations that attempt to control the dynamic response of the system. Examples of these constraint equations are limits on residual vibration, robustness to modeling errors and shaper gain.

The constraint on residual vibration amplitude can be expressed as the ratio of residual

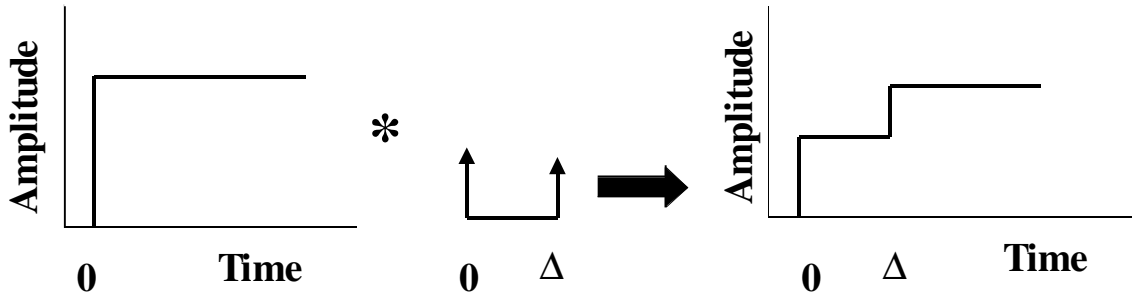

Figure 6: Input Shaping Example.

vibration amplitude with shaping to that without shaping. The percentage vibration can be determined by using the expression for residual vibration of a second-order harmonic oscillator of frequency ω and damping ratio ζ. The vibration from a series of impulses is divided by the vibration from a single impulse to get the percentage vibration [8]:

$$V = e^{-\zeta\omega t_n}\sqrt{[C(\omega,\zeta)]^2 + [S(\omega,\zeta)]^2} \tag{1}$$

where,

$$C(\omega,\zeta) = \sum_{i=1}^{n} A_i e^{-\zeta\omega t_i}\cos\left(\omega\sqrt{1-\zeta^2}t_i\right) \tag{2}$$

and

$$S(\omega,\zeta) = \sum_{i=1}^{n} A_i e^{-\zeta\omega t_i}\sin\left(\omega\sqrt{1-\zeta^2}t_i\right) \tag{3}$$

If the constraint equations only require zero residual vibration, then the resulting shaper is called a Zero Vibration (ZV) shaper and given by [67]

$$\begin{bmatrix} A_i \\ t_i \end{bmatrix} = \begin{bmatrix} \frac{1}{1+K} & \frac{K}{1+K} \\ 0 & \Delta T \end{bmatrix} \tag{4}$$

where

$$K = exp(-\frac{\zeta\pi}{\sqrt{1-\zeta^2}}) \tag{5}$$

and

$$\Delta T = \frac{\pi}{\omega\sqrt{1-\zeta^2}} \tag{6}$$

A ZV shaper will not work well on many systems because it will be sensitive to modeling errors [71]. While the wide-spread implementation of input shaping is a recent occurrence,

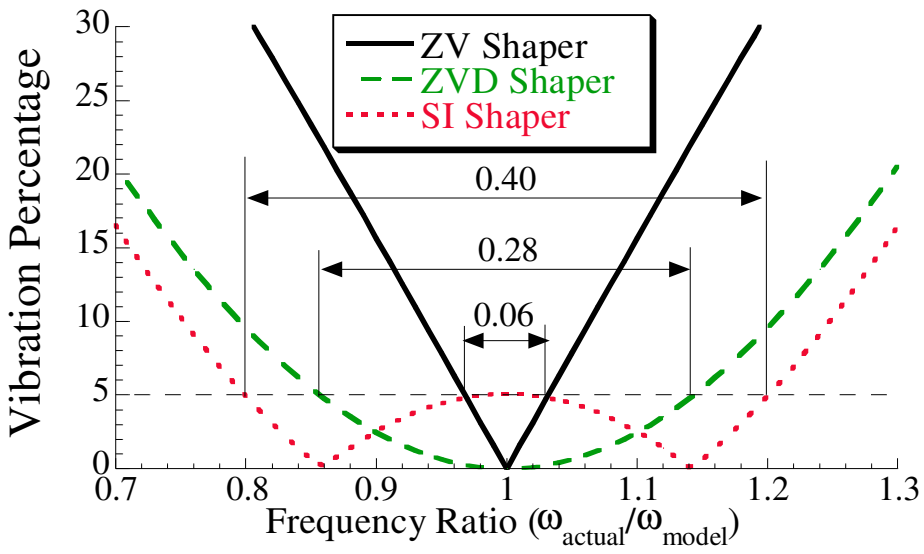

Figure 7: Sensitivity Plot.

the idea is not a new one. The earliest incarnation of ZV shaping was the technique of posicast control developed by O.J.M. Smith in the 1950's [67]. The method works well on systems when the natural frequencies are well known, but the commands are not very robust to modeling errors [71].

For input shaping to work well on most real systems, the constraint equations must ensure robustness to modeling errors. Singer and Seering developed a form of robust input shaping by setting the derivative with respect to the frequency of the residual vibration given in (1) equal to zero [59]. The resulting shaper is called a Zero Vibration and Derivative (ZVD) shaper. This derivative can be written

$$0 = \frac{d}{d\omega}\left(e_{-\zeta\omega t_n}\sqrt{[C(\omega,\zeta)]^2 + [S(\omega,\zeta)]^2}\right) \tag{7}$$

The shaper that meets the requirements of (1) and (7) can be expressed as

$$\begin{bmatrix} A_i \\ t_i \end{bmatrix} = \begin{bmatrix} \frac{1}{1+2K+K^2} & \frac{2K}{1+2K+K^2} & \frac{K^2}{1+2K+K^2} \\ 0 & \Delta T & 2\Delta T \end{bmatrix} \tag{8}$$

A sensitivity plot is used to measure of robustness to modeling errors and compare different shapers. Figure 7 shows a sensitivity plot. Here, the normalized frequency is on the abscissa while the Percent Residual Vibration is on the ordinate. The Percent Residual

Vibration, the ratio of the unshaped vibration to the shaped vibration, is calculated using (1) and multiplying by 100. To measure robustness, we determine the insensitivity of the command shaper. The insensitivity is the range of frequencies over which the residual vibration percentage is below a desired level. In Figure 7 a 5% residual vibration is considered to be the acceptable level. Using this as the standard level, a ZV shaper has an insensitivity of 0.06. This means that the shaper limits the residual vibration below the tolerable limit for $\omega_{actual} = \omega_{model} + / - 3\%$. The ZVD shaper, created using (7) has an insensitivity is 0.28. The price paid for this increase in robustness is the increase in shaper duration (Δ in Figure 6). The ZV shaper's duration is on the order of 1/2 the period of vibration while the ZVD's duration is on the order of 1 period of vibration.

The third shaper shown in Figure 7 is a Specified Insensitivity (SI) Shaper. This class of shapers limits the vibration percentage over a specified range of frequencies [66]. The range of frequencies to be suppressed can be expressed as percentages of a baseline frequency. Figure 7 shows an SI shaper with a 0.4 insensitivity. That is, it keeps the residual vibration at or below the tolerable limit for +/-20% of the modeling frequency. Note that there will be a small amount of vibration when the model is perfect. The SI shaper does not have a zero vibration constraint, merely a range of frequencies to suppress. SI shapers are most useful when the robustness requirements are significantly different than the ones available from standard shapers.

1.2.2 Negative Input Shapers

1.2.2.1 Unity Magnitude, Zero Vibration Shapers

The command shapers in the previous section were created using only positive impulses. The shaper duration can be decreased by using negative impulses, but the potential for actuator saturation and the excitation of un-modeled high modes exists. The Unity Magnitude, Zero Vibration Shapers shown in Figure 8 were created to minimize the undesirable consequences of using negative impulses [65]. For an undamped system, the time locations for the UM-ZV

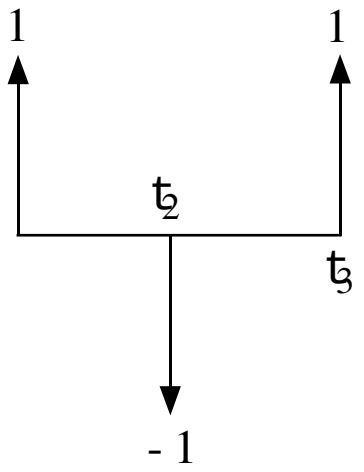

Figure 8: Unity Magnitude, Zero Vibration Shaper.

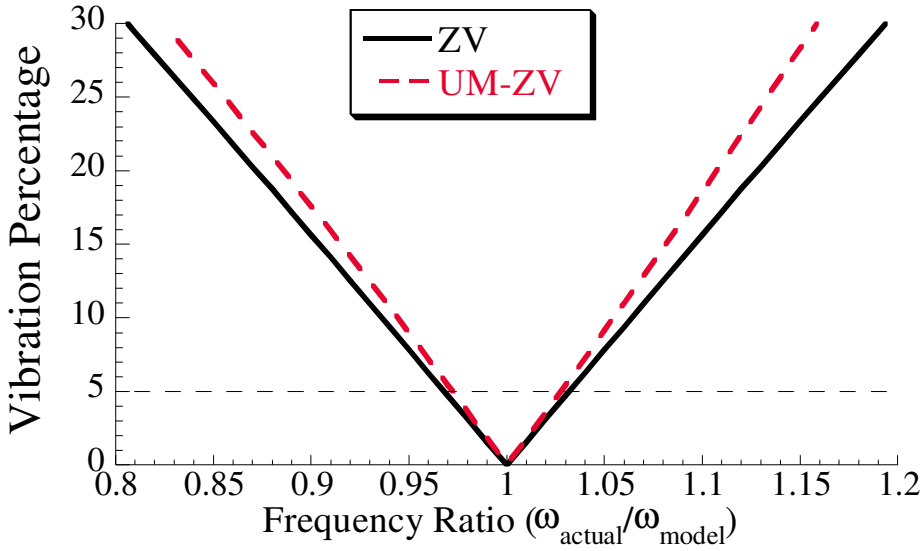

Figure 9: Sensitivity Plot of Zero Vibration Shapers.

shaper impulses are:

$$\begin{bmatrix} A_i \\ t_i \end{bmatrix} = \begin{bmatrix} 1 & -1 & 1 \\ 0 & \frac{T}{6} & \frac{T}{3} \end{bmatrix} \tag{9}$$

An optimization routine is needed to solve for the impulse locations for damped systems, but curve fits to those solutions are available [65]. The UM-ZV shaper's duration is approximately 33% shorter than the ZV shaper's duration.

Figure 9 shows a comparison of the sensitivity plots of the ZV and UM-ZV shapers. The UM-ZV shaper has an insensitivity of approximately 0.05. (Recall that ZV shaper's

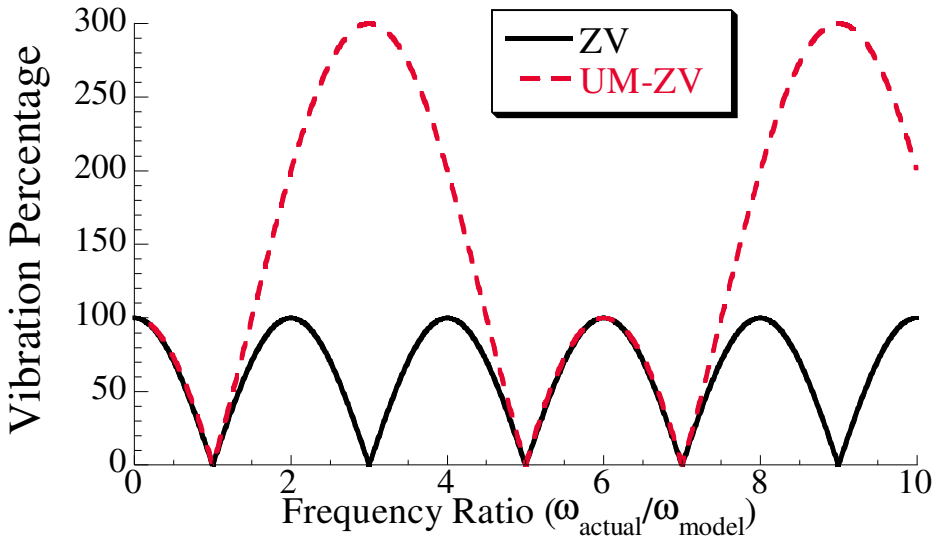

Figure 10: High Mode Sensitivity Plot of Zero Vibration Shapers.

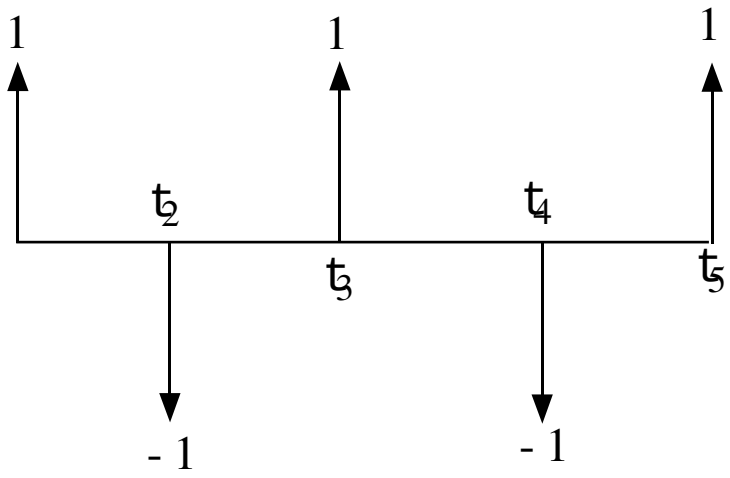

Figure 11: Unity Magnitude, Zero Vibration and Derivative Shaper.

insensitivity is 0.06.) Near the modeled frequency, the robustness of the ZV and the UM-ZV are virtually identical. Figure 10 shows that the similarities no longer hold at higher frequencies. The ZV shaper never exceeds the residual vibration of the unshaped input, and successfully eliminates vibration at odd multiples of the model frequency. The UM-ZV shaper, however, exceeds the vibration of the unshaped input by 300% at three times and nine times the model frequency. This would excite any un-modeled modes in those ranges.

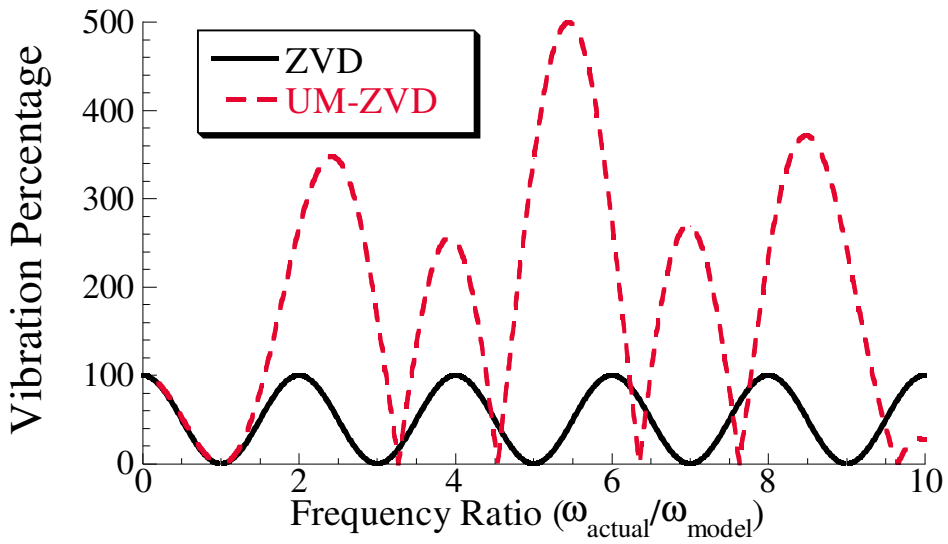

Figure 12: High Mode Sensitivity Plot of Zero Vibration Shapers.

1.2.2.2 Unity Magnitude, Zero Vibration and Derivative Shapers

Negative impulses can also be used to create robust input shapers. Figure 11 shows a negative Zero Vibration and Derivative (UM-ZVD) shaper. The insensitivity of the UM-ZVD shaper is 0.23, or only 18% less than the ZVD, while the UM-ZVD's duration is approximately 25% less than that of the ZVD shaper containing only positive impulses. However, the excitation of the high modes is even more pronounced with the UM-ZVD. Figure 12 shows the sensitivity plot for the ZVD and the UM-ZVD. The residual vibration of the UM-ZVD reaches a maximum of 500% of the unshaped vibration and exceeds the unshaped vibration by a significant amount at frequencies much higher than the model frequency. Despite the potential for high mode excitement, negative impulse shapers are a viable option when trying to balance the benefit of robustness with the cost of shaper duration.

1.3 Deflection-Limiting Commands

A significant amount of research has focused on developing reference commands for slewing flexible systems [6, 9, 5, 33]. One significant area of work has been the generation of on-off command profiles [33, 60, 54, 37]. Initial efforts created commands that eliminated residual

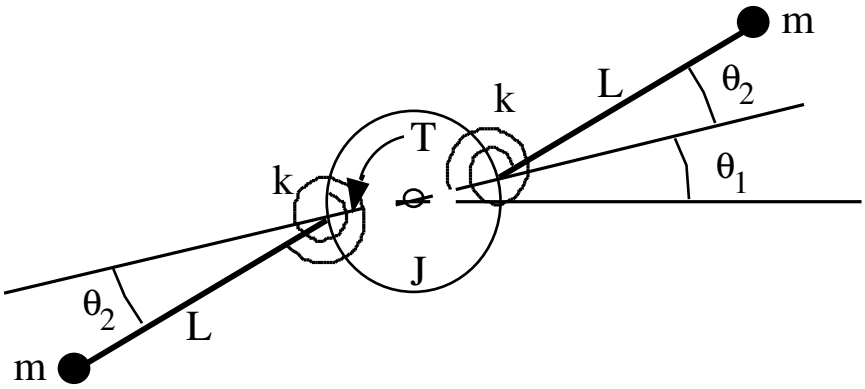

a)

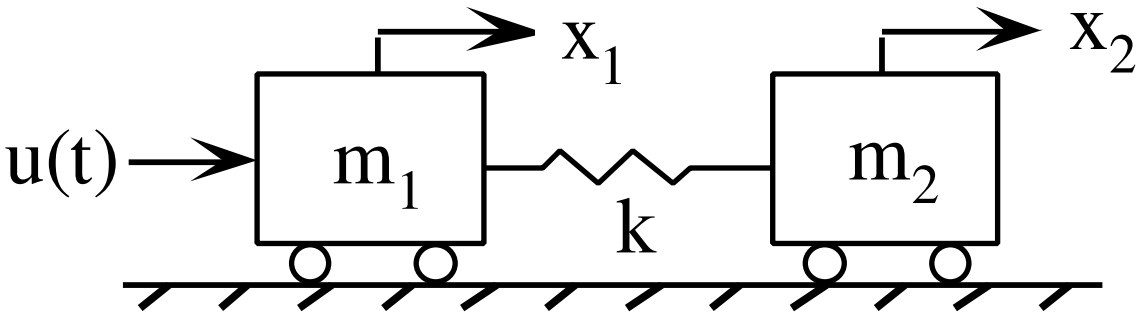

b)

Figure 13: Simple Models Used in Input Shaping.

vibration at the end of the move. While these commands successfully eliminated vibration, they could create large deflections during the move. In an effort to avoid the internal stresses that result from these deflections, commands have been developed that place a limit on the transient deflection [60, 12]. Most of the methods developed thus far require the use of a numerical optimization to produce the on-off command profile; the notable exception is a sub-optimal approach that produces a quasi bang-bang command [62]. Other techniques have been suggested to test the time-optimality of the optimization results [73, 43].

One of the great advantages of input shaping is that it requires only simple system models like the ones shown in Figure 13. Simple models can be used because input shaping can be made robust to modeling errors. The robustness allows the command profiles developed for simple systems to work effectively on more complex systems. The amplitudes and time locations of the impulses in an input shaper are determined by satisfying a set of constraint equations while minimizing the maneuver duration. Often a nonlinear optimization is used to solve for the input shaper. The constraints for deflection-limiting on-off shaping can be categorized as follows:

- Residual Vibration Constraints
- Robustness Constraints
- Requirement of Time Optimality
- Rigid-body Constraints
- Constraints on the Impulse Amplitudes
- Deflection Constraints

Residual Vibration Constraints

The constraint on residual vibration can be conveniently expressed as the ratio of residual vibration amplitude with input shaping to that without shaping by (1). The impulse amplitudes and time locations needed to make this equation zero can be determined, as in the Zero Vibration shaper.

Robustness Constraints

In addition to limiting residual vibration amplitude, most input shaping formulations require some amount of robustness to modeling errors. Although shapers such as the ZVD or SI have been shown to provide adequate robustness to modeling errors, the deflection-limiting commands in this example will use the ZV constraints. The use of ZV constraints is justified because the focus is the limitation of transient deflections, not residual vibrations. The additional robustness constraints are completely compatible with the deflection-limiting constraints described here.

Requirement of Time Optimality

Due to the transcendental nature of the residual vibration equation, there will always be multiple solutions to the constraint equations. To make the solution time optimal when subject to the residual vibration and robustness equations, the shaper must be made as short as possible. Therefore, the time optimality constraint is:

$$min(t_n) \tag{10}$$

where t_n is the time location of the final impulse.

Rigid-Body Constraints

To ensure that the system's mass center will move the desired amount, constraints must be placed on the rigid-body response. For example, the linearized equations of motion of the system shown in Figure 13a are:

$$\begin{bmatrix} J + 2m(R+L)^2 & 2m(R+L)L \\ 2m(R+L)L & 2mL^2 \end{bmatrix} \begin{bmatrix} \ddot{\theta}_1 \\ \ddot{\theta}_2 \end{bmatrix} = \begin{bmatrix} T \\ -2k\theta_2 \end{bmatrix} \tag{11}$$

where J is the moment of inertia of the main body, m is the mass of the particles at the end of the rod of length L, R is the distance from the center of the main body to the attachment point of the rods, k is the rotational spring constant and T is the torque on the main body. For rest-to-rest motion, the rigid-body constraints are:

$$\dot{\theta}_1(t_n) = 0 \tag{12}$$

$$\theta_1(t_n) = \theta_{1f} \tag{13}$$

where θ_{1f} and t_f are the desired final move angle and final time, respectively. Analogous equations are used to constrain the rigid-body motion in a system such as the one shown in Figure 13b.

Impulse Amplitude Constraints

The time-optimal control for rest-to-rest motion of the systems shown in Figure 13 subject to (1) and/or (7) has been shown to be a multi-switch bang-bang profile [44]. Therefore, the time-optimal input to the system under consideration must consist of alternating positive and negative constant-amplitude force pulses. A multi-switch bang-bang profile can be

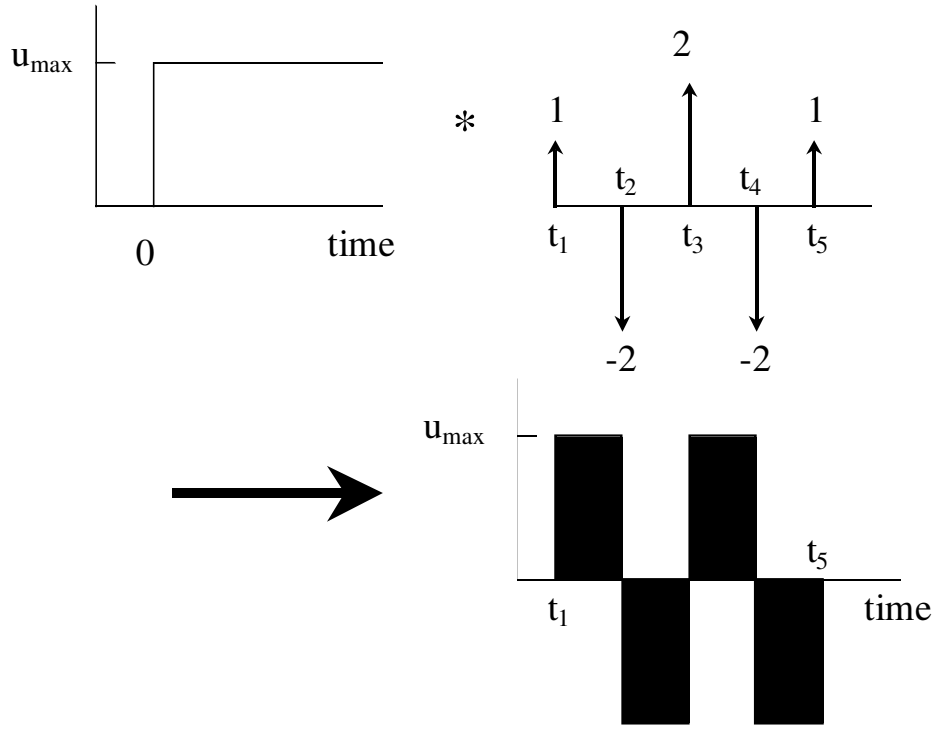

Figure 14: Using Input Shapers to Create On-Off Commands.

generated by convolving a step input with an input shaper of the form:

$$\begin{bmatrix} A_i \\ t_i \end{bmatrix} = \begin{bmatrix} 1 & -2 & 2 & -2 & \dots & -2 & 1 \\ 0 & t_2 & t_3 & t_4 & \dots & t_{n-1} & t_n \end{bmatrix} \tag{14}$$

where n is an odd integer. Figure 14 shows the result when a shaper of this type is convolved with a step input. The amplitude of the step input is equal to the maximum actuator effort, u_{max}. Equation (14 leads to the following constraints on the impulse amplitudes:

$$\begin{aligned} A_i &= 1 \qquad\qquad i = 1, n \\ A_i &= 2(-1)^{i-1} \quad i = 2, \dots, n-1 \end{aligned} \tag{15}$$

The constraints given by (10) and (15) are equivalent to requiring the time-optimal control given actuator limitations [44]. The requirement of (10) alone is not sufficient because the impulse amplitudes will be driven towards positive and negative infinity by the time-optimality requirement.

Deflection Constraints

The solution of (1), (10), (12), and (13) will lead to commands that eliminate residual vibration and have some level of robustness to modeling errors. However, the deflection

of the system during the move is uncontrolled. If the deflection is large, the system may be damaged, or the endpoint may deviate considerably from an intended trajectory. In order to control the level of deflection during the move, an expression for the deflection as a function of the input shaper must be obtained. The desired expression can be generated using superposition of deflections from individual step inputs [60].

While the deflection-limiting commands depend on the specific system under consideration, the derivation for an example of a benchmark model that is applicable to a wide range of systems is found below. An expression for the deflection of the system shown in Figure 13b is easily derived. The result is applicable to other systems with one flexible mode and a rigid-body mode, such as the system in Figure 13a. The Laplace transforms of the equations of motion for the system shown in Figure 13b are [60]:

$$F(s) = (m_1 s^2 + k)x_1(s) - kx_2(s) \tag{16}$$

$$0 = (m_2 s^2 + k)x_2(s) - kx_1(s) \tag{17}$$

Equation 17 can be solved for $x_2(s)$:

$$x_2(s) = \frac{k}{m_2 s^2 + k} x_1(s) \tag{18}$$

Combining (16) and (18) and assuming F(t) is a step input of magnitude u_{max} gives:

$$x_1(s) = u_{max} \left\{ \frac{m_2 s^2 + k}{s^2 \left[m_1 m_2 s^2 + (m_1 + m_2)\, k \right]} \right\} \tag{19}$$

The deflection for this system is the change in the natural length of the spring, which is defined as $D(t) = x_2(t) - x_1(t)$. Compression is a negative value; extension is positive. Therefore, from (18) and (19) we have:

$$D(s) = \left[\frac{k}{(m_2 s^2 + k)} - 1 \right] x_1(s) \tag{20}$$

substituting (19) into (20) yields:

$$D(s) = \frac{-u_{max} m_2}{m_1 m_2} \left\{ \frac{1}{s(s^2 + \omega^2)} \right\} \tag{21}$$

where,

$$\omega^2 = \left(\frac{m_1 + m_2}{m_1 m_2} \right) k \tag{22}$$

Taking the inverse Laplace transform of (21), assuming zero initial conditions, gives the deflection from a step input as a function of time:

$$D(t) = \frac{D_{max}}{2}[\cos(\omega t) - 1] \tag{23}$$

where ω is the natural frequency of oscillation and the maximum deflection magnitude, D_{max} is given by:

$$D_{max} = \frac{2u_{max}m_2}{k(m_1 + m_2)} \tag{24}$$

The coefficient in (23) is written as $D_{max}/2$ because the quantity enclosed in the brackets has a maximum magnitude of two. A deflection equation with a structure identical to (23) can be similarly derived for the system shown in Figure 13a.

Multiple versions of (23) can be used to generate a function that describes the deflection throughout a move containing many step inputs (a pulse in force is composed of two step inputs - one positive and one negative delayed in time). Assuming that the command profile consists of a series of pulses, the deflection throughout the move is given by:

$$D(t) = D_{(m)-(m+1)}(t) \qquad t_m \leq t \leq t_{m+1}, \quad m = 1, \ldots, n \tag{25}$$

where

$$D_{(m)-(m+1)}(t) = \sum_{1=2}^{m} A_i \frac{D_{max}}{2} \left[\cos(\omega(t - t_i)) - 1\right] \tag{26}$$

It is important to note the restriction presented by the qualifier in (25). The deflection which occurs between the first and second impulses of the input, $D_{1-2}(t)$, (the period during the first pulse) is given by (25) when m = 1. The deflection, $D_{2-3}(t)$, between the second and third impulses is given by (25) when m = 2. This is the coasting period between the first and second positive pulses. The deflection, $D_{3-4}(t)$, that occurs during the second pulse is given by (25) with m = 3, and so on. This process of generating the deflection function is illustrated in Figure 15. Equation (25) amounts to a piecewise-continuous function composed of n finite length segments; each of the segments has a limited range of applicability. Note that the magnitude of deflection caused by a series of pulses can exceed D_{max} if the deflection components from individual pulses interfere constructively.

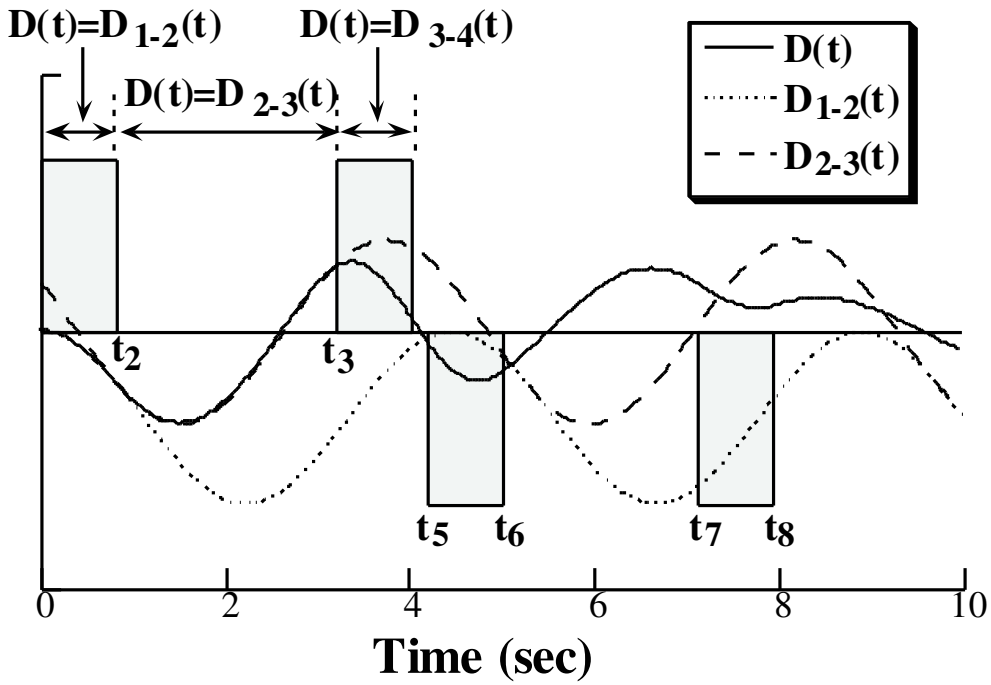

Figure 15: Piecewise Deflection.

Given an expression for the deflection as a function of the impulse time locations, such as that given in (25), deflection-limiting command profiles can be designed by using the deflection expression as a constraint equation. There are several ways of enforcing the deflection constraint. One simple method uses deflection sampling [60]. Basically, the deflection expression is sampled at several points within the time interval of the command profile. At these points, the deflection expression is required to be below the desired level. If the sampling points are sufficiently close together, then the deflection will be effectively limited to the desired value. Given the complexity of the problem, an optimization routine is traditionally used to produce a deflection-limiting command profile.

At this point, a few comments on optimization should be made. Optimization has the objective of maximizing the return from, or the minimizing the cost of, the operation of a process while satisfying the physical constraints of the system. These processes may be physical, economic or social. Traditionally, an optimization problem consists of three parts: a performance index, constraint equations, and initial and boundary conditions.

There are a few difficulties associated with using optimization routines. First, a solution

Table 1: Optimization Results Given Different Initial Guesses.

	t_1	t_2	t_3	t_4	t_5	t_6,t_7	t_8	t_9	t_{10}	t_{11}	t_12
IG_1	0	1.5	1.8	2.2	2.7	4.2	5.4	6.2	6.6	7.2	8.6
OR_1	0	0.655	1.738	2.949	4.206	4.315	4.424	5.681	6.897	7.976	**8.630**
IG_2	0	1.3	1.8	2.2	2.7	4.0	5.3	5.7	6.2	6.6	8.0
OR_2	0	1.077	1.838	2.158	2.659	3.900	5.140	5.641	5.962	6.722	**7.799**

to a problem may not exist. The solution may call for inadmissible control or cause the system to follow an inadmissible trajectory. Second, the optimal solution may not be unique. While non-unique solutions create computational problems, they may allow the engineer to consider factors other then the performance index when choosing a solution. When multiple solutions exists, the solution may be subject to local minima. An often over-looked and under-appreciated, step in an optimization routine is the selection of the initial guess.

1.3.1 Initial Guess Algorithm for creating deflection-limiting commands

A method for generating initial guesses is needed because a nonlinear optimization routine is used to determine the time locations of the switches in an On-Off command. Table 1 shows the optimization result (OR) for two solutions to the same problem formulation. Note that the initial guesses (IG) make a significant impact on the solution that is returned by the optimization program. The solution returned by the first set of initial guesses is 10% longer that the solution returned by the second set of initial guesses.

This section reviews a method for creating initial guesses for optimization routines that solve for deflection-limiting on-off command profiles [51]. The method utilizes the input shaping process and relies on characteristics of deflection-limiting commands that were previously discussed. The method produces initial guesses that facilitate convergence to the time-optimal solution for the deflection-limiting problem formulation. A numerical optimization is used to obtain the command profile.

Because the optimization routine is subject to local minima, convergence to the time-optimal solution is dependent on the initial guess. The method for generating initial guesses for deflection-limiting commands is as follows: 1) given the system description generate the time-optimal command, 2) generate the fuel-efficient command by using the time-optimal

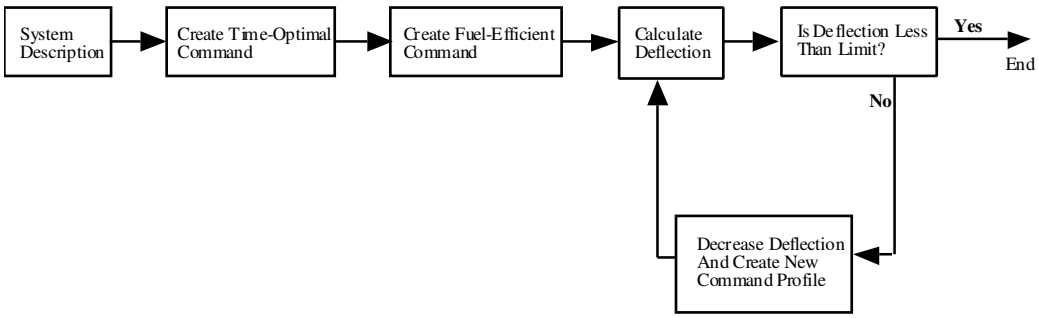

Figure 16: Flow Chart for the Initial Guess Algorithm.

solution as the initial guess, and 3) incrementally decrease the allowable deflection until the desired level is reached. The flow chart for this algorithm is shown in Figure 16. Given the system description, the time-optimal command for a rest-to-rest move can be determined using methods such as those proposed by Tuttle and Seering [73]. From that point the algorithm can iterate through until the deflection limit is reached.

Using this approach, deflection-limiting commands can be developed for the generic mass-spring-mass system shown in Figure 13b. Following the bench-mark examples in the literature, the system parameters (m_1, m_2, k, F) were assumed to be unity and the slew distance was set to 5 units. For these parameters the system has a natural frequency of 0.2251 Hz and the force-to-mass ratio is 0.5. The number of pulses was fixed at 4 and the incremental reduction in deflection step size was 0.02. Several iterations of the command profile and the corresponding deflections are shown in Figure 17.

As previously reported, the first pulse accelerates the system until the deflection limit is reached [60]. Additional pulses keep the system at or near the deflection limit until the slew is completed. Figure 17 shows that as the length of the first pulse is shortened, the deflection is decreased. Furthermore, increasing the coast period between the first and second pulse also decreases the system's deflection. While the results shown here are only for four-pulse profiles, similar results can be produced for 6, 8, or any numbered pulse profile.

1.3.1.1 Design Considerations for the Initial Guess Algorithm

There are two major design considerations when implementing the Initial Guess Algorithm: the number of pulses and the deflection step size. Implementation of the algorithm can

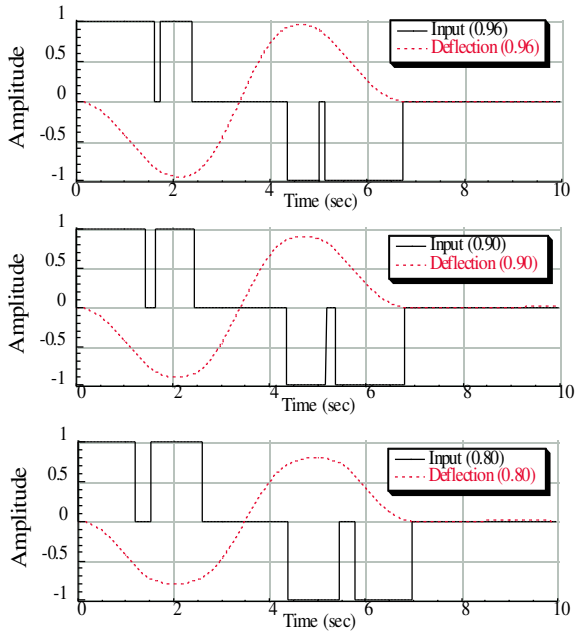

Figure 17: Using Initial Guess Algorithm to Create Deflection-Limiting Commands.

be simplified if the number of pulses is made to be independent of the system parameters. This can be done by fixing the number of impulses in the shaper. If the number of pulses is greater than the optimal solution, then the solution can converge to the time-optimal solution. However, the solution will be lengthened if the number of pulses is less than the optimal solution.

If the deflection is limited to an amount significantly less than the fuel-efficient deflection, then the final command will be composed of a greater number of pulses than the fuel-efficient profile [60]. Breaking up the fuel-efficient profile into the desired number of pulses before starting the deflection-limiting portion of the algorithm will speed up the convergence. It is always better to have more pulses than needed because the impulses can be cancelled out when they are not needed.

The deflection step size the algorithm takes in finding the intermediate solutions has an effect on the speed of convergence. It is easier to find the intermediate solution when small step sizes are used. However, the number of intermediate solutions needed to reach the final deflection limit is increased. When large step sizes are used, the number of intermediate solutions is decreased but the chance of a failed optimization or the solution converging to

a non-minimum-time solution is increased.

The size of the step is relative to the rate of change of the pulse profiles. The impulse time locations change slowly relative to the deflection limit for deflections from 100% to 60% of the vibration-free move [60]. In this range, a deflection step size of 2-5% will converge quickly to a solution. For deflections less than 0.6 the time locations change quickly and a small step size, 1%, should be used. When developing commands with no *a priori* knowledge of their structure, the algorithm should start with a small step size and a large number of pulses.

1.3.2 Digital deflection-limiting commands

The previous section documented the difficulties that arise when deflection-limiting commands are designed using a nonlinear optimization. An algorithm was proposed to simplify the process, however, it still required a significant amount of user input. Input shapers can be designed in the digital domain, rather than the continuous domain, to eliminate the need for a nonlinear optimization [40, 74, 53]. This characteristic of digital shaping is extremely useful. Eliminating the need for the nonlinear optimization greatly simplifies the process used to create the commands.

Nonlinear optimization solvers must be used to design most continuous shapers; however, the optimization problem is simplified for digital shapers. For example, suppose a digital ZV shaper is desired. A ZV shaper has three constraints: two zero vibration $\mathrm{C}(\omega, \zeta) = 0$, $\mathrm{S}(\omega, \zeta) = 0$, from (2) and (3) and the unity magnitude constraint which requires the impulse amplitudes to sum to one.

For a continuous shaper, the impulse locations t_i are considered to be arbitrary. Because the impulse locations are not fixed in time, the exponential terms as well as the sine and cosine terms in (2) and (3) are nonlinear which requires the use of nonlinear optimization routines. On the other hand, a digital shaper requires that each t_i be fixed by the sampling period $\Delta\mathrm{T}$. As a result the exponential terms and the sine and cosine terms become known constants. The a_i terms remain as the only unknowns and appear linearly in the constraints. Once $\Delta\mathrm{T}$ is chosen, only the number of time steps, n, remains as a nonlinear element. If

n is held constant then the constraints are completely linearized such that constraints (2) and (3) become simply

$$a^T c = 0 \tag{27}$$

and

$$a^T s = 0 \tag{28}$$

where a is a vector of impulse amplitudes which corresponds to a_i in (2) and (3), and s and c are vectors containing the remainder of the constraint equations. The digital shaper is thus defined as a vector of amplitudes, a, the components of which are evenly spaced in time by ΔT.

A similar approach can be used to linearize the deflection equations [52]. This eliminates the need for the initial guess and assures convergence. The constraint equations for the digital deflection-limiting commands are the same as those for the continuous case, the differences are in the formulations of the constraint equations.

The major difference between the continuous and digital deflection-limiting constraint equations is the impulse time locations [52]. In the continuous case, there are no restrictions on the locations of the impulses. For digital commands the impulse times locations are set as an integer multiple of the controller update speed. Other differences come in the formulation of the constraints on impulse amplitudes and the deflection constraints. When producing the continuous deflection limiting commands, the command was forced to be an On-Off profile. This was done for three reasons. First, the On-Off profiles were shown to be the fuel-efficient form. Second, On-Off profiles did not excite higher modes and limited the occurrence of actuator saturation. Third, forcing the command to this form facilitated convergence to a solution. In the digital case, the amplitudes are simply constrained to have a magnitude no greater than unity:

$$-1 \leq a_i \leq 1 \tag{29}$$

Deflection sampling was used to calculate the deflection in the continuous case. The deflection was required to be below the desired level at all the sampled points. A minimum

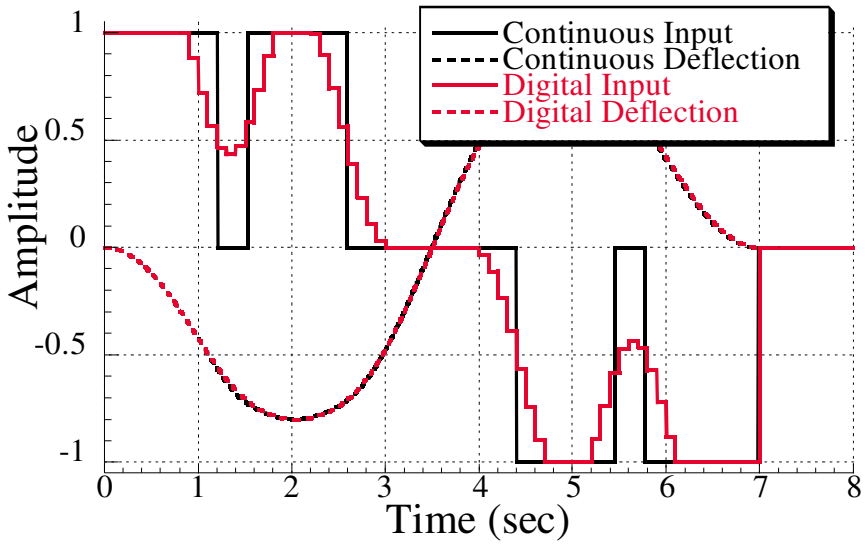

Figure 18: Comparison of Continuous Time and Digital Deflection-Limiting Commands.

sample point space had to be determined in order to ensure that the deflection never exceeded the desired level. The digital deflection limiting constraints are calculated at every digital time spacing. It is highly unlikely that the deflection will significantly exceed the limit given the closeness of the time spacing.

Figure 18 shows a comparison of the continuous and the digital deflection-limiting commands. While the input commands are different, they result in similar deflection profiles. It should also be noted that the digital command is less than one time spacing longer than the continuous command. While creating the deflection-limiting commands in the digital domain has eliminated the dependence on initial guess and reduced some of the difficulties associated with nonlinear optimizations, it still requires significant computational effort.

1.4 Dissertation Outline

This dissertation improves the state-of-the-art in satellite control in three major areas:

- Deflection-limiting commands for the rest-to-rest moves of flexible systems
- Combined design of command shaping and feedback control for tether retrieval of nadir-pointing satellites

- Increased rotation rate and decreased vibration during the spin-up of spinning tethered satellite systems

The remaining chapters of the dissertation are organized as follows: Chapter 2 details the derivation of Analytic Deflection-Limiting commands. These commands can be created without a numerical optimization, greatly simplifying the process. Also in this chapter is an experimental verification of the deflection-limiting commands and new analysis tools for rest-to-rest command profiles. Chapter 3 contains the retrieval of nadir-pointing tethered satellite systems using the two-dimensional massless, inextensible tether model. Here the combination of command shaping with feedback controller gain selection for reduced retrieval time is described. Chapter 4 extends the research in Chapter 3 to three dimensions. The coupling between the in-plane and out-of-plane swing angles will be investigated and a new method for controlling out-of-plane oscillations is introduced. Chapter 5 introduces a spinning tethered satellite system and investigates the use of command shaping to reduce vibration during the spin-up process and increase the overall spin rate at the conclusion of the spin-up process. Finally, Chapter 6 summarizes the dissertation and outlines extensions of this research and other future work.

CHAPTER II

ANALYTIC DEFLECTION-LIMITING COMMANDS

Deflection-limiting commands have been shown to be extremely useful. These commands can move a flexible system without residual vibration while simultaneously limiting the transient deflection to a prescribed level. Unfortunately, deflection-limiting commands have traditionally been created using numerical optimization methods. In order for these pre-computed commands to reach their full potential and utility, the commands must calculated before hand, and stored for later use in real time. However, unless all of the possible move distances and deflection limits are known *a priori*, such as in repetitive motions, this is not a viable option. For systems where both computational power and data storage space is lacking, creating the commands as needed or storing a large number of commands is not possible. Therefore, the need exists for a simple method for creating deflection-limiting commands.

This chapter presents methods for creating deflection-limiting commands analytically. That is, the commands can be described by simple closed-form expressions. First, a new tool for creating command shapers that limit the tracking error of a mass under PD control will be presented. Next, a procedure to produce commands for a benchmark mass-spring-mass system will be presented. The commands can be made robust to modeling errors and a sensitivity analysis of the commands will be presented. Experiments on a large bridge crane will verify the utility of the commands. Finally, the deflection-limiting shapers developed for rest-to-rest moves will be used to limit tether deflection during electrodynamic reboost.

2.1 Specified Deflection, Zero Vibration Commands

It is an extremely common practice during the initial phases of controller design to model satellites as point masses. This is done do eliminate the negative effects of flexibility and concentrate on the overall control scheme. In this stage of the design, trajectory tracking

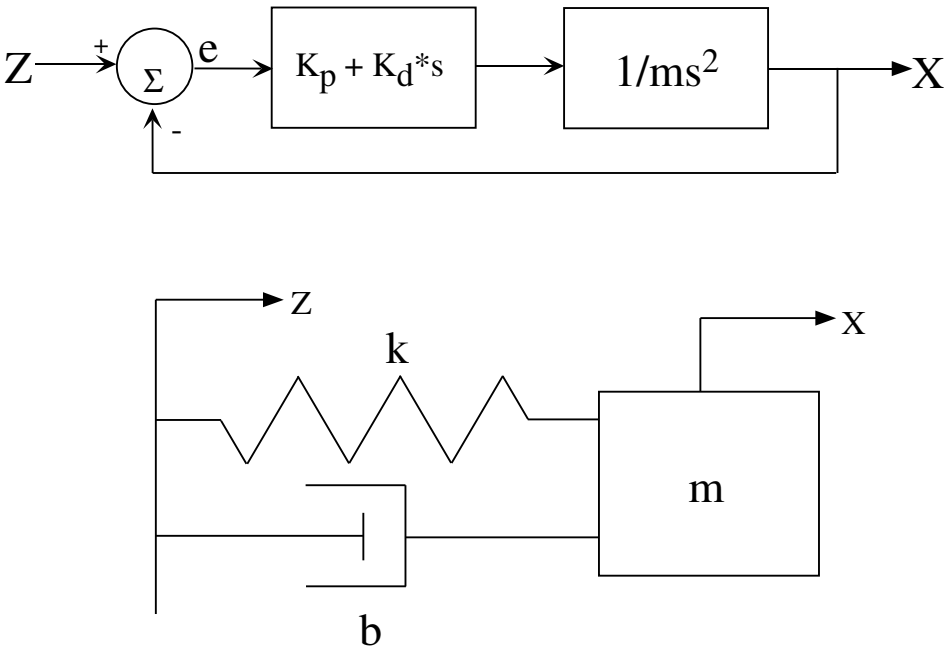

Figure 19: Mass under PD Control.

is of great concern. One of the most common and simple controllers in the Proportional and Derivative (PD) controller. When PD control is used to control the motion of a point mass, the block diagram shown in Figure 19 results. This block diagram is equivalent to the position input system shown in Figure 19. The feedback controller is the source of the flexibility. Command shaping has been shown to improve the trajectory tracking of flexible systems [64], but the trajectory tracking error was not limited to a specific amount. This section presents a method for producing command shapers for the system shown in Figure 19 that will limit the tracking error to a specific ratio of the unshaped tracking error.

2.1.1 Vector Diagrams

The direct solution of (1) is not the only way to create input shapers. Vector diagrams can be used to create the impulse sequence [63]. A vector diagram is a graphical representation in polar coordinates (r-θ space) of the impulse sequence. Figure 20 shows an example of a vector diagram representation of a two-impulse sequence applied to an undamped system. On a vector diagram, the magnitude of the vector, A, is equal to the impulse amplitude and the angle of the vector $\theta = \omega t$, where ω is the natural frequency of the system in rad/s

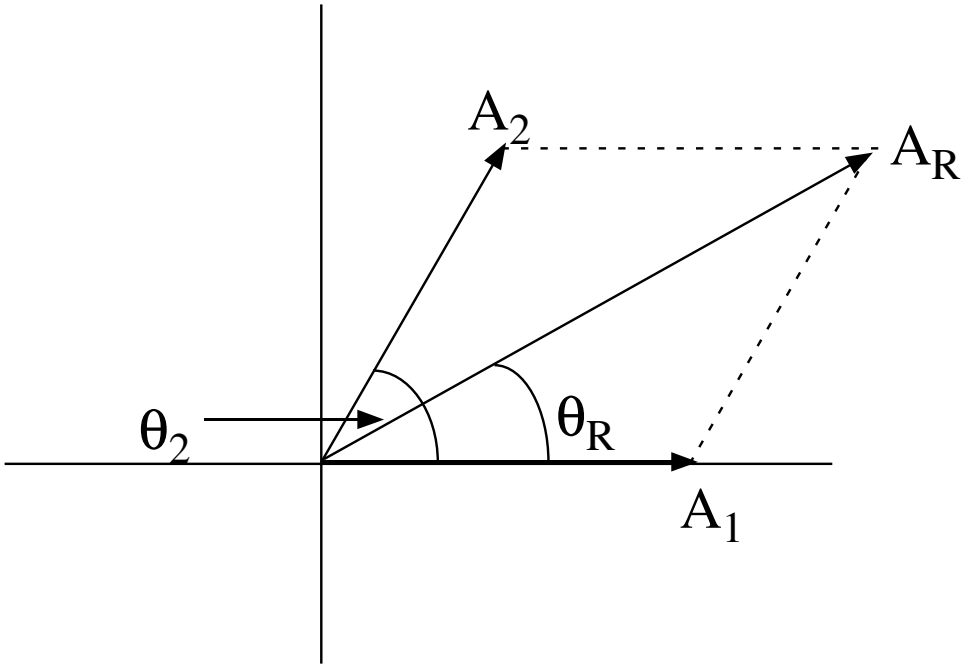

Figure 20: Vector Diagram.

and t is equal to the time location of the impulse. The amplitude of the resultant vector, A_R, for the impulse sequence equals the amplitude of the residual vibration.

Intelligent use of the vector diagram can lead to the rapid creation of residual-vibration-reducing impulse sequences with minimal computational effort [63]. The residual vibration can be eliminated by adding a single vector (impulse) to cancel A_R. The augmented sequence of impulses will then cause zero residual vibration.

2.1.2 Deflection Vector Diagrams

The Deflection Vector Diagram (DVD) is a modification of the vector diagram and is developed specifically for the equivalent systems shown in Figure 19. The DVD differs from the Vector Diagram in that the DVD tracks the transient deflection in addition to determining the residual vibration from an impulse sequence. On a DVD, the maximum amplitude of the resultant vector during the impulse sequence is equal to the maximum possible ratio of the shaped to unshaped deflections.

The use of the DVD is best demonstrated assuming step changes in input position, z. As a simple case, assume the damping (derivative gain) to be zero. To create a DVD

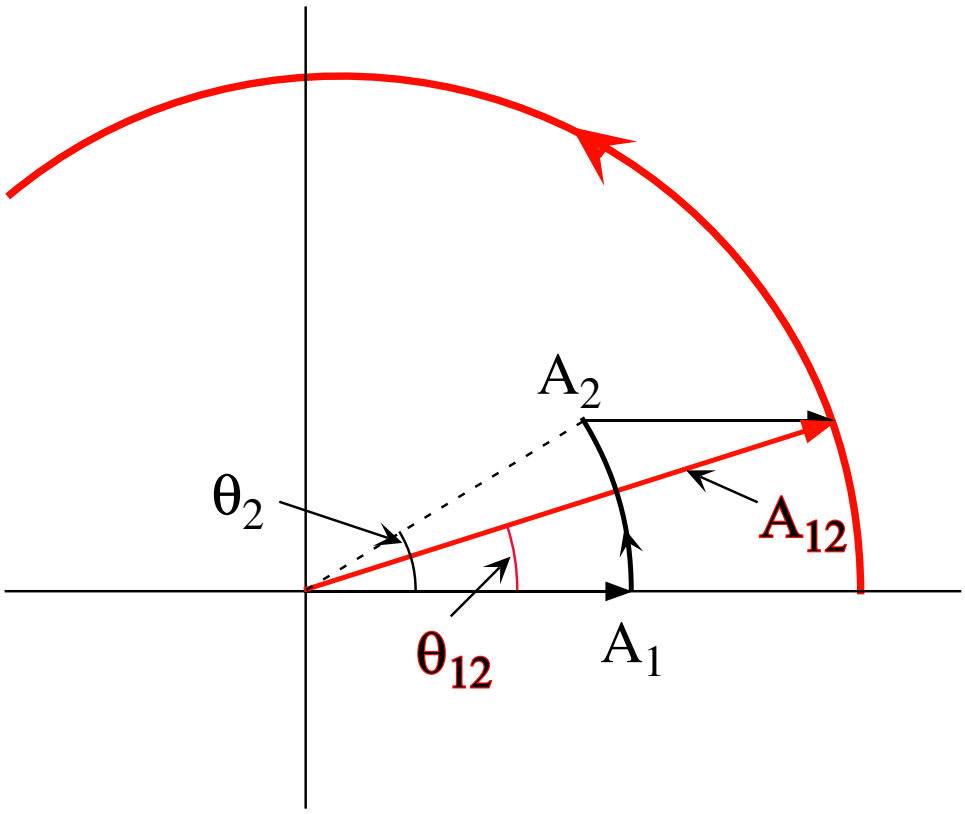

Figure 21: Deflection Vector Diagram.

representation of an impulse sequence (assuming t_1=0), first draw impulse A_1 horizontally on the x-axis starting at the origin. Second, rotate this vector θ_2, where $\theta_2 = \omega t_2$, then add A_2 in the horizontal direction to the rotated A_1. (Note: For a damped system, the amplitude of the arc will decay as it rotates according to $e_{-\zeta\omega_n t}$.) This results in the new deflection represented by vector A_{12} with phase θ_{12}. After t_2, a new arc of radius A_{12} is traced on the DVD starting from θ_{12}. This process is shown in Figure 21 for the impulse sequence used in Figure 20. Continue this process until all additional impulses are plotted. The amplitude of the resultant vector for the entire impulse sequence gives the amplitude of the residual vibration, just like on a vector diagram. However, the maximum possible transient deflection amplitude is given by the maximum amplitude of the resultant vector that occurs anywhere *during* the plotting of the impulse sequence.

The magnitude of the *maximum* transient deflection is equal to the magnitude of the resultant vector on the DVD. So, to limit the transient deflection to a specific limit, all that

needs to be done is limit the amplitude of the maximum resultant vector to a specific limit. This limit can be displayed graphically as a circle whose radius is equal to the deflection limit on the DVD. To design shapers to limit the transient deflection below a specific value on the DVD, draw a circle whose radius is the deflection limit and determine an impulse sequence whose vector sum is zero (for zero vibration) and whose intermediate sums stay within the circle.

To develop the mathematical background for the DVD, start with the derivation of the deflection for the system shown in Figure 19. The equation of motion for system can be written,

$$m\ddot{x} + b\dot{x} + kx = b\dot{z} + kz \tag{30}$$

Taking the Laplace of (30) (assuming zero initial conditions) and solving for $X(s)$,

$$X(s) = \frac{(b/m)s + k/m}{s^2 + (b/m)s + k/m} Z(s) \tag{31}$$

Noting that deflection, $D(s)$, is $X(s) - Z(s)$

$$D(s) = X(s) - Z(s) = \frac{-s^2}{s^2 + (b/m)s + k/m} Z(s) = \frac{-s^2}{(s + \zeta\omega_n)^2 + \omega_d^2} Z(s) \tag{32}$$

where,

$$\omega_n = \sqrt{k/m} \tag{33}$$

$$\zeta = \frac{b}{2\sqrt{km}} \tag{34}$$

and

$$\omega_d = \omega_n \sqrt{1 - \zeta^2} = \sqrt{\frac{k}{m} - \frac{b^2}{4m^2}} \tag{35}$$

Assuming that $z(t)$ is a step input of unity magnitude

$$D(s) = X(s) - Z(s) = \frac{-s^2}{s^2 + (b/m)s + k/m} \frac{1}{s} = \frac{-s}{(s + \zeta\omega_n)^2 + \omega_d^2} \tag{36}$$

and taking the inverse Laplace yields

$$d(t) = e_{-\zeta\omega_n t} \left[-\cos\omega_d t + \frac{\zeta}{\sqrt{1 - \zeta^2}} \sin\omega_d t \right] \tag{37}$$

Reducing the above equation to a single cosine yields

$$d(t) = e_{-\zeta\omega_n t} \left[-\sqrt{1 - \frac{\zeta}{1 - \zeta^2}} \cos\omega_d t + \phi \right] \tag{38}$$

where,

$$\phi = \arctan \frac{\zeta^2}{\sqrt{1-\zeta^2}} \tag{39}$$

Equation 38 shows that the deflection time response for a step input is a damped sinusoid with the maximum deflection equal to the magnitude of the step input. For the undamped case, the deflection resulting from a step shaped with an impulse sequence can be derived as

$$d(t) = \sum_{i=1}^{n} -A_i \cos \omega(t - t_i) \tag{40}$$

where A_i and t_i are the amplitude and time location, respectively, of the i^{th} impulse.

For $t < t_1$

$$d(t) = 0 \tag{41}$$

for $t = t_1$

$$d(t) = -A_1 \tag{42}$$

for $t_1 < t < t_2$

$$d(t) = -A_1 \cos \omega(t - t_1) = -A_1 \cos \omega t - \phi_1 \tag{43}$$

for $t_2 < t < t_3$

$$d(t) = -A_{12} \cos \omega(t - t_2) + \phi_{12} \tag{44}$$

where

$$A_{12} = \sqrt{(-A_1 \sin \omega(t_2 - t_1))^2 + (-A_1 \cos \omega(t_2 - t_1) - A_2)^2} \tag{45}$$

and

$$\phi_{12} = \frac{A_1 \sin \omega(t_2 - t_1)}{A_1 \cos \omega(t_2 - t_1) + A_2} \tag{46}$$

for $t_3 < t < t_4$

$$d(t) = -A_{123} \cos \omega(t - t_3) + \phi_{12} \tag{47}$$

where

$$A_{123} = \sqrt{(-A_{12} \sin \omega(t_3 - \phi_{12}))^2 + (-A_{12} \cos \omega(t_3 - \phi_{12}) - A_3)^2} \tag{48}$$

and

$$\phi_{123} = \frac{A_{12} \sin \omega(t_3 - \phi_{12})}{A_1 \cos \omega(t_3 - \phi_{12}) + A_3} \tag{49}$$

This pattern can be repeated until the end of the impulse sequence is reached. The A_{ijk} are the ratios of the shaped to the unshaped deflections. The amplitudes of these A_{ijk} can be formulated as an additional constraint and the impulse amplitudes and time locations can be determined for Specified Deflection shapers. However, an alternative to the direct solution of the above equations is a graphical solution using the Deflection Vector Diagram.

2.1.3 Specified Deflection, Zero Vibration (SD-ZV) Shapers

Specified Deflection, Zero Vibration (SD-ZV) command shapers eliminate residual vibration and limit the transient deflection. The transient deflection's amplitude is expressed as a ratio of the shaped system's deflection to the unshaped system's deflection. Figure 22 plots the traditional ZV and ZVD shapers on the DVD and shows that ZV commands limit the transient deflection to 50% of the unshaped command, while ZVD commands limit the transient deflection to 25%.

SD-ZV commands for the undamped case were created via direct solution of the deflection equations for deflections ranging from 45% to 20% of the unshaped command. The shaper durations for 3 impulse and 4 impulse SD-ZV shapers are shown in Figure 23. Four impulse SD-ZV shapers are noticeably shorter than 3 impulse shapers for deflection limits less than 30%. The trade-off is that 4 impulse shapers are slightly more difficult to create graphically, via direct solution of the constraint equations, or through the use of a numerical optimization.

Figure 24 shows the sensitivity curves for a SD-ZV (deflection - 25%) and a ZVD shaper. A sensitivity curve is a plot of the percentage residual vibration (vibration with shaping divided by the vibration without shaping) versus the normalized frequency (the actual frequency, wa, divided by the modeling frequency, wm). Insensitivity, I, is defined as the range of frequencies over which the residual vibration amplitude is below a desired level. The toleration limit considered here is 5%. The SD-ZV shaper is not as robust as the ZVD shaper. Its 5% Insensitivity is 0.10, while the ZVD has an insensitivity of 0.29. However, while designed for the same deflection limit as the ZVD, the SD-ZV command's duration is only 0.834T, where T is the period of vibration, or approximately 17% shorter than the

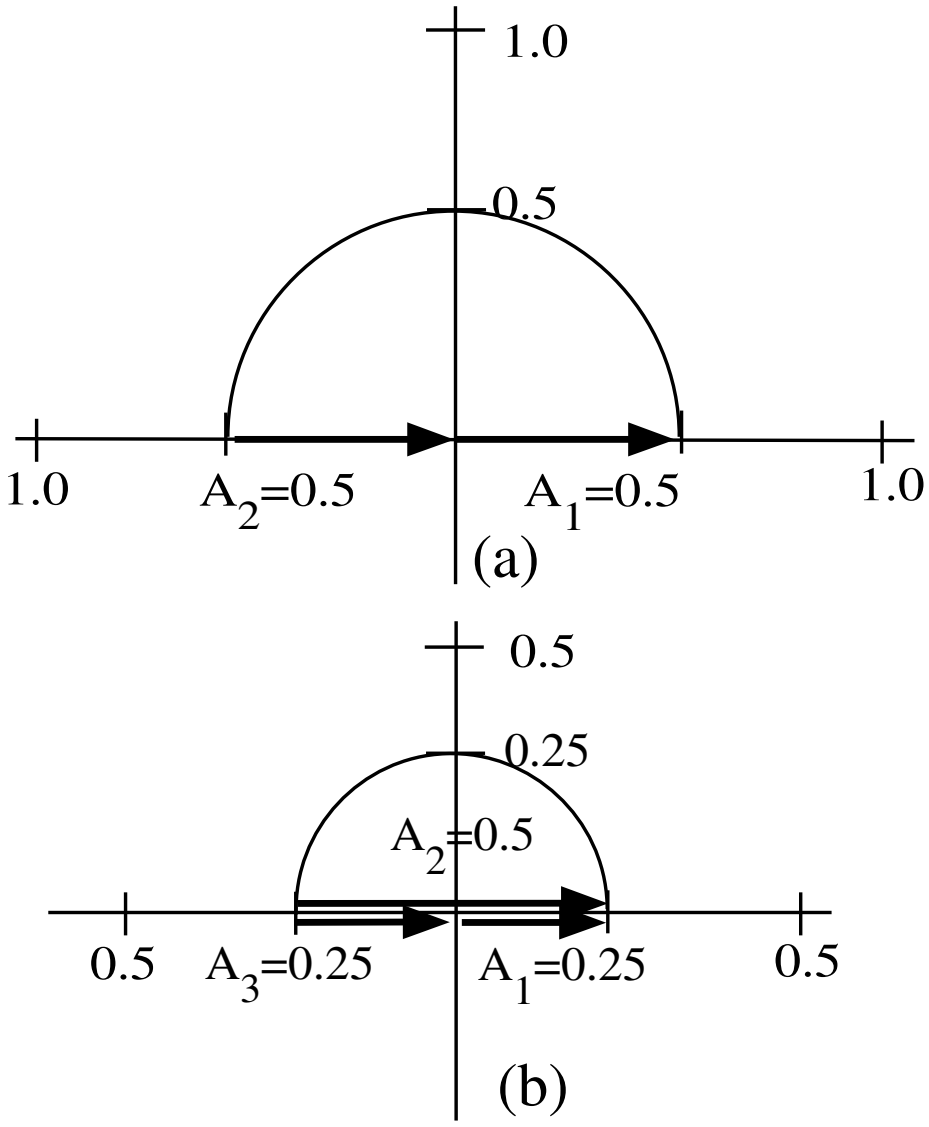

Figure 22: ZV & ZVD Deflection Vector Diagrams.

ZVD command.

Figure 25 shows the sensitivity curves for a SD-ZV shaper whose duration is 1.04T, which is approximately equal to the duration of a ZVD shaper. This command has an Insensitivity of 0.35 and a deflection of 20%. So, for similar shaper durations, the 4 impulse SD-ZV command is more robust and limits the transient deflection to a lower value than the ZVD. For a deflection limit of 0.25, the SD-ZV shaper is not as robust, but has a shorter duration than the ZVD shaper. And for a shaper duration equal to T, the SD-ZV shaper is more robust and has a lower deflection limit.

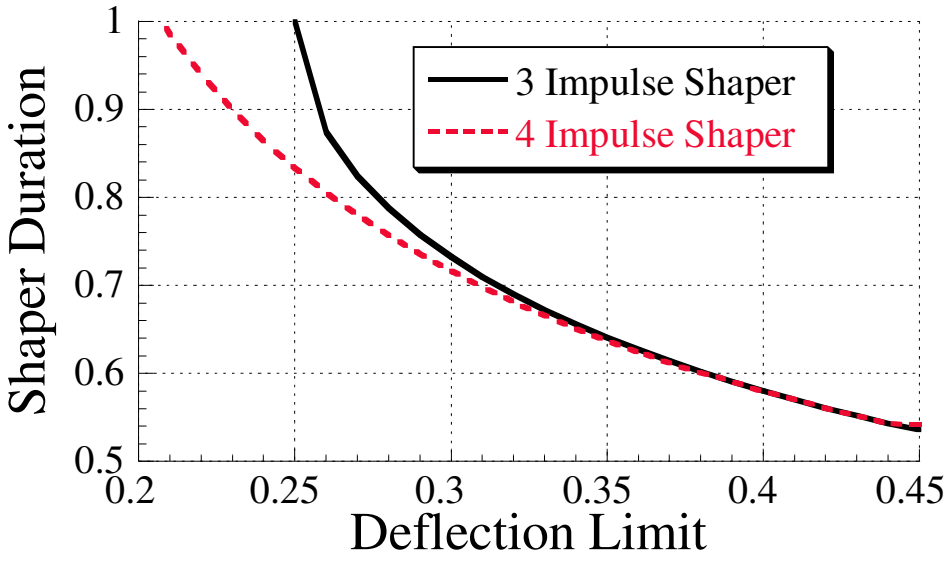

Figure 23: SD-ZV Command Duration.

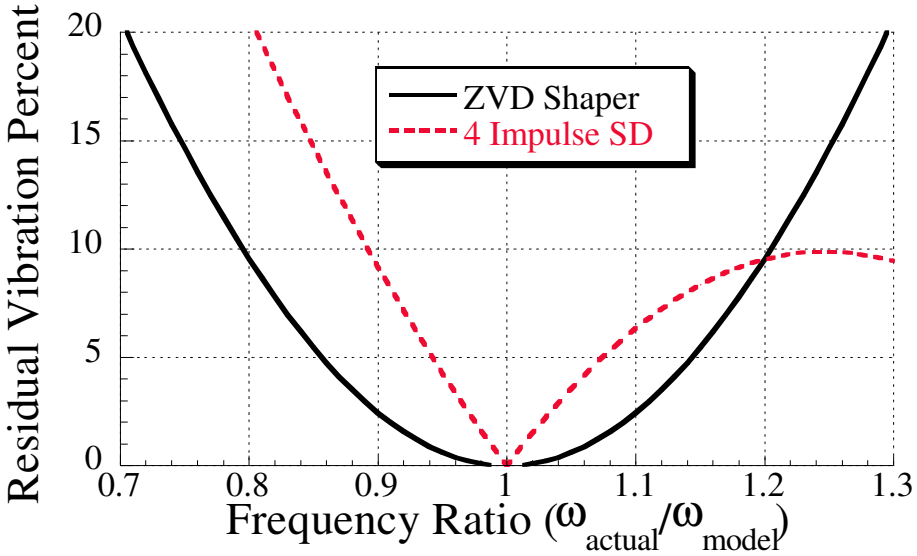

Figure 24: SD-ZV (0.25) Sensitivity Curve.

2.1.4 Simulation Results

While step commands were used to develop SD-ZV commands, the percent reduction in transient deflection is maintained for any arbitrary command. This is because any command can be decomposed into a series of step commands. Simulations were conducted using a trapezoidal position command consisting of a 1 second rise, a 2.5 second dwell, and a 1

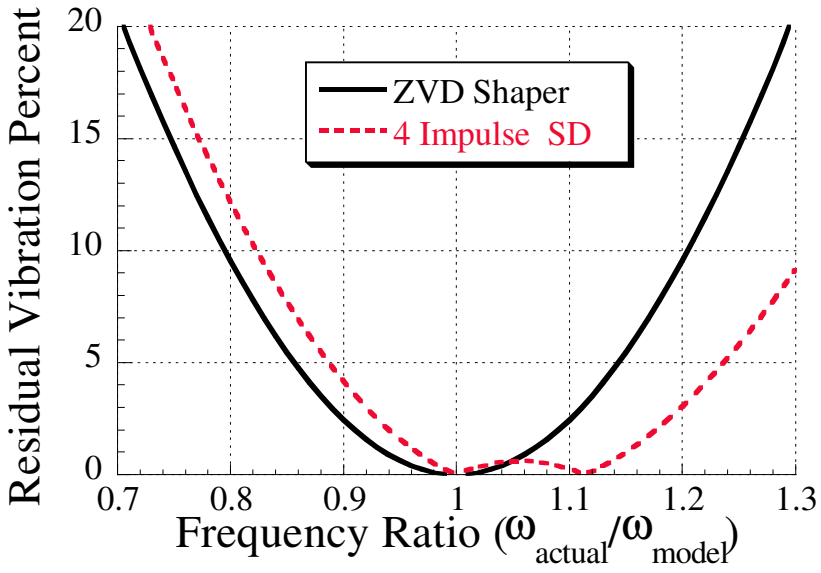

Figure 25: SD-ZV (Duration 1.04T) Sensitivity Curve.

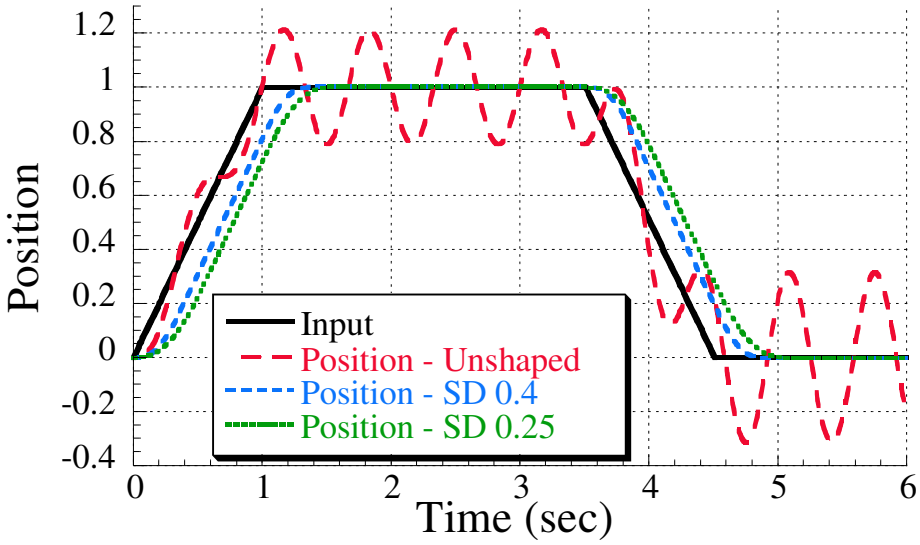

Figure 26: Undamped System's Position Response.

second return. This command is used to drive an undamped 1.5 Hz, system. Figure 26 shows the system's response to the unshaped and shaped commands. Note that both SD-ZV commands discussed result in zero residual vibration. Also, note that the SD-ZV 0.25 response is slightly longer than the SD-ZV 0.40 response.

Figure 27 shows the deflection during the move. The SD-ZV shapers keep the deflection below the desired limit. Note that the unshaped deflections from each portion of the move

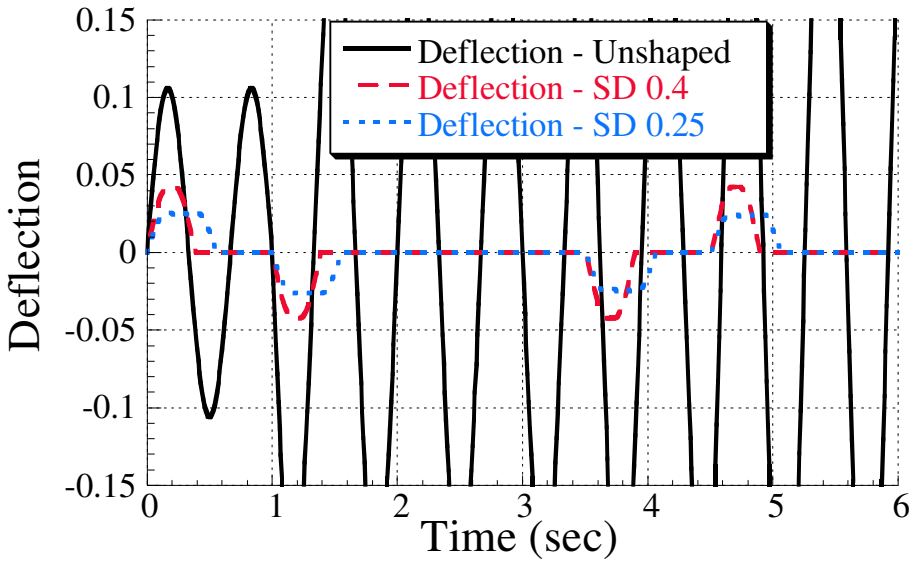

Figure 27: Undamped System's Deflection.

combine constructively. That is, the deflections caused by the initial rise portion combines with the deflections induced during the dwell and return portions of the move. Hence the increasing amplitudes of vibration for the unshaped command. The deflections for the shaped commands are eliminated at the conclusions of each segment of the reference command, so there is no addition of deflection amplitudes. Consequently, the SD-ZV shapers limit the deflection to the specified limit of each individual command segment, which gives the appearance of limiting the deflection to ratios smaller than the ones for which they were designed during the dwell and return portions of the move.

Next, the SD-ZV commands were simulated on a 1.5 Hz system with a damping ratio of 0.05. The same rise-dwell-return reference command was used. The command was shaped using 3 impulse SD-ZV shapers designed for teh new system parameters. Figure 28 shows the system's response, while Figure 29 shows the deflection during the move. Again, the SD-ZV shapers keep the deflection below the specified limit.

SD-ZV are used to limit the tracking error for a mass under PD control. Real satellites will have some flexibility and cannot be modeled as point masses. For more representative models, more complicated shaping schemes will be needed. The next section presents a method for limiting the deflection of a system containing one rigid-body and one flexible

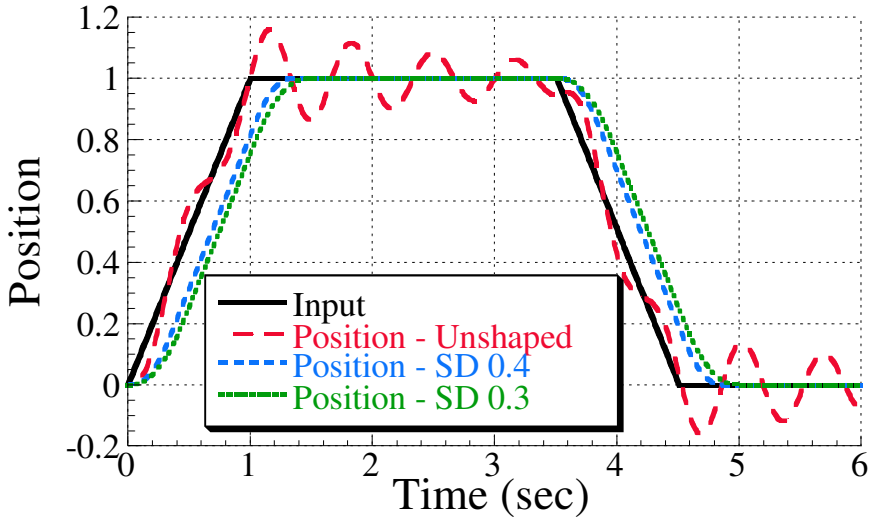

Figure 28: Damped System's Position Response.

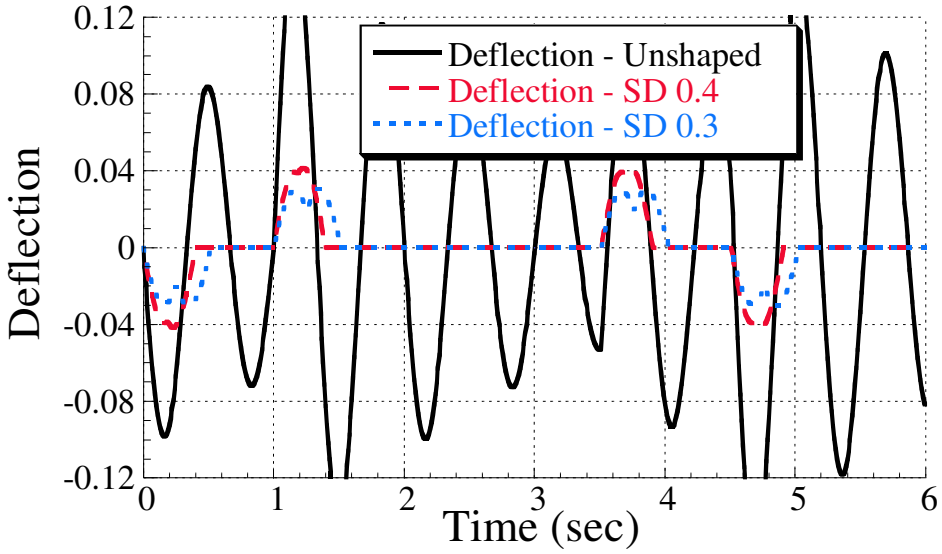

Figure 29: Damped System's Deflection.

mode.

2.2 Analytic On-Off Commands

Deflection-limiting commands were originally created to fill a need in the motion control of flexible systems [12, **?**]. For example, Figure 30 shows a sketch of the Waves in Space Plasma (WISP) system [2]. The WISP system consists of two 150 m long antenna booms

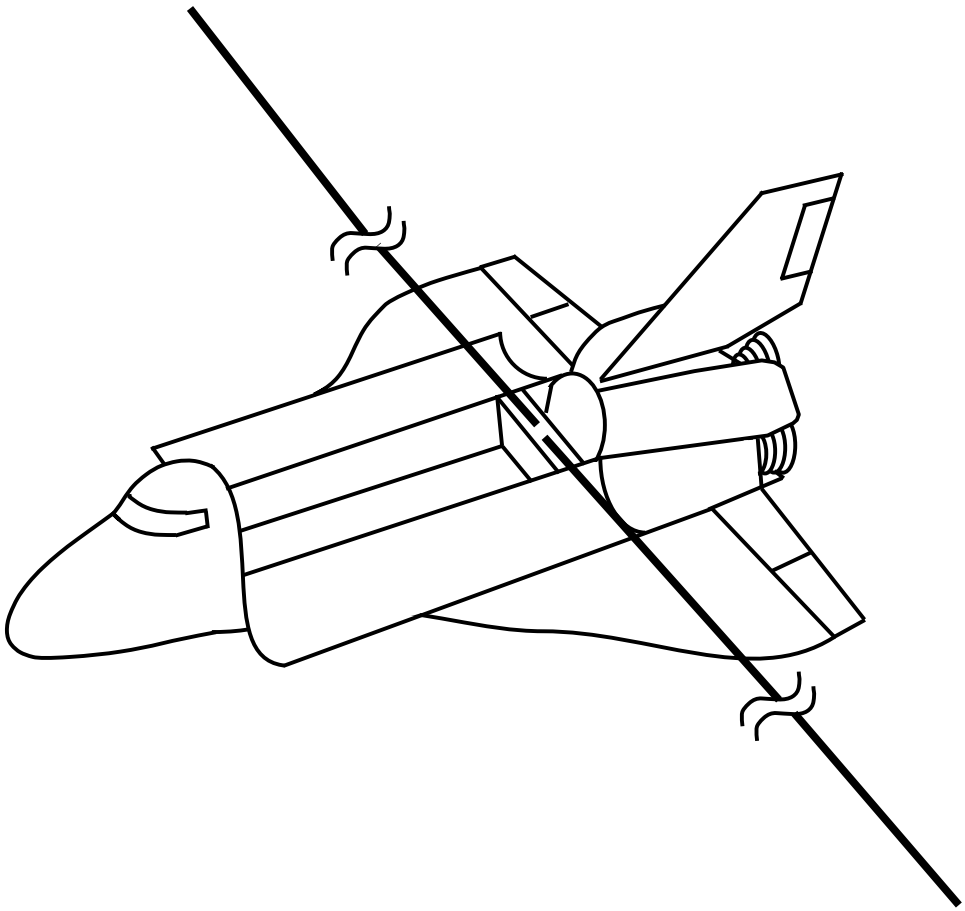

Figure 30: WISP System.

attached to the Space Shuttle. When the system is moved using using shuttle thrusters, large deflections can occur at the endpoints, as shown in Figure 31. Command shaping can be used to eliminate the residual vibration and reduce the deflection. There has been a significant amount of research in creating vibration-free rest-to-rest moves of flexible systems [6, 9, 5, 33, 54]. Traditionally, these commands were created using numerical optimization techniques. One approach, however, created these commands analytically [62, 66]. In this approach, the command for a rest-to-rest move was divided into three transitions: first is the transition from rest to acceleration, next is the transition from acceleration to deceleration and finally the transition from deceleration to rest. These transitions are shown schematically in Figure 32. If there is zero vibration after each transition, there will be no vibration for the complete move. Vibration-free transitions can be easily produced using traditional input shaping techniques. The time between the transitions can be determined

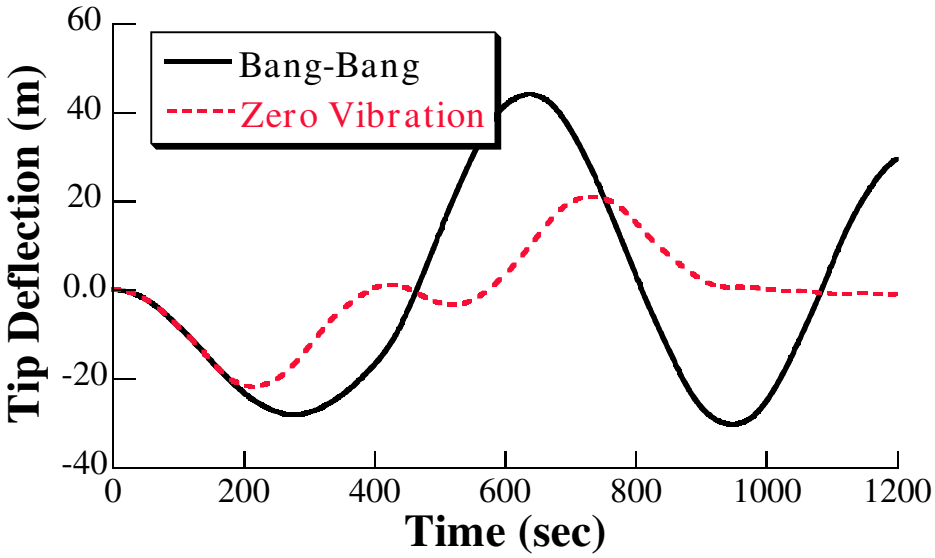

Figure 31: Deflection Response WISP of System.

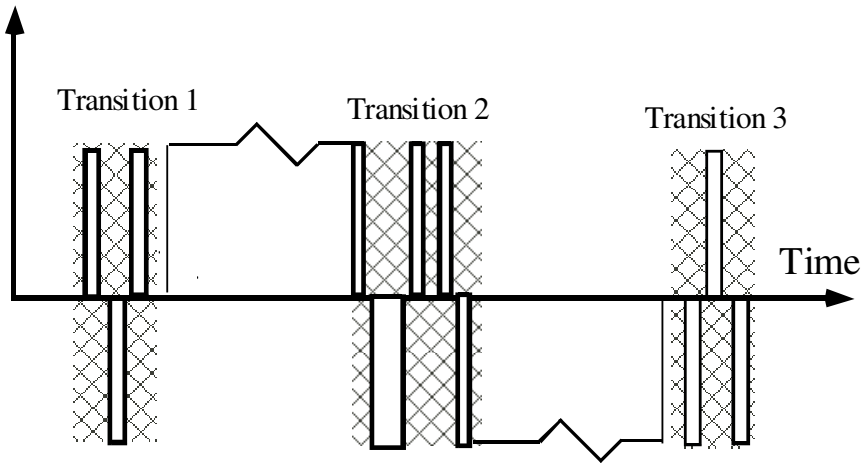

Figure 32: Creating Analytic On-Off Commands.

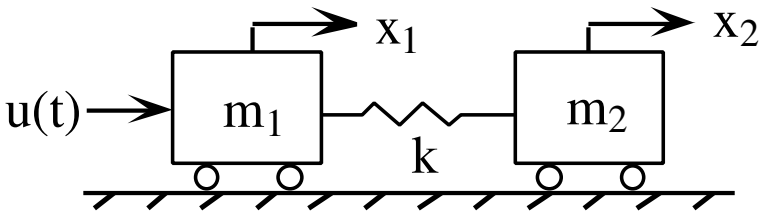

Figure 33: Benchmark Mass-Spring-Mass Model.

by integrating the rigid-body equations of motion. This two-stage solution process provides an avenue for obtaining solutions in closed form.

For example, consider the benchmark system of Figure 13b, re-plotted here as Figure 33 with all parameters set to unity. This creates a system with a force-to-mass ratio of 0.5 and a natural frequency of $\sqrt{2}$ rad/s (0.2251 Hz). If transitions 1 and 3 are accomplished with a Unity Magnitude, Zero Vibration (UM-ZV)shaper [65] defined as,

$$\begin{bmatrix} A_i \\ t_i \end{bmatrix} = \begin{bmatrix} 1 & -1 & 1 \\ 0 & T/6 & T/3 \end{bmatrix} \tag{50}$$

and transition 2 is accomplished with a Zero Vibration (ZV) shaper defined as

$$\begin{bmatrix} A_i \\ t_i \end{bmatrix} = \begin{bmatrix} -1 & -1 \\ 0 & T/2 \end{bmatrix} \tag{51}$$

where T is the period of vibration, then the entire command shaper can be described by

$$\begin{bmatrix} A_i \\ t_i \end{bmatrix} = \begin{bmatrix} 1 & -1 & 1 & -1 & -1 & 1 & -1 & 1 \\ 0 & t_2 & t_3 & t_4 & t_5 & t_6 & t_7 & t_8 \end{bmatrix} \tag{52}$$

with t_6, t_7 and t_8 defined by symmetry. To completely define the command shaper, t_4 must be determined. This can be achieved by considering the constraint on the rigid-body motion to yield

$$t_4 = \frac{-T}{12} + \sqrt{\frac{t}{12}^2 + \frac{x_d}{\alpha}} \tag{53}$$

When convolved with a step, the shaped input is a series of pulses, as shown in Figure 34. The resulting command for a move distance of 5 unit is shown in Figure 35. Figure 36 shows the input and responses for move distances of 10 and 15 units. The only differences between the input commands are the times between transitions 1 and 2. For all of the move distances the deflection of the system is 0.5, which is equivalent to $D_{max}/2$ defined in (24). This is the amplitude of deflection for a vibration-free move. Analytic On-Off commands are extremely useful when transient deflection is not a dominant issue, or when the "natural" deflection is below the allowable limit. While command shaping methods greatly reduced the deflection in the WISP system, there is still 20 meters of deflection during the move in Figure 31. When transient deflection is a concern, analytic On-Off commands may not be suitable because they do not provide a mechanism for lowering deflection. The following section presents a procedure for creating analytic deflection-limiting commands.

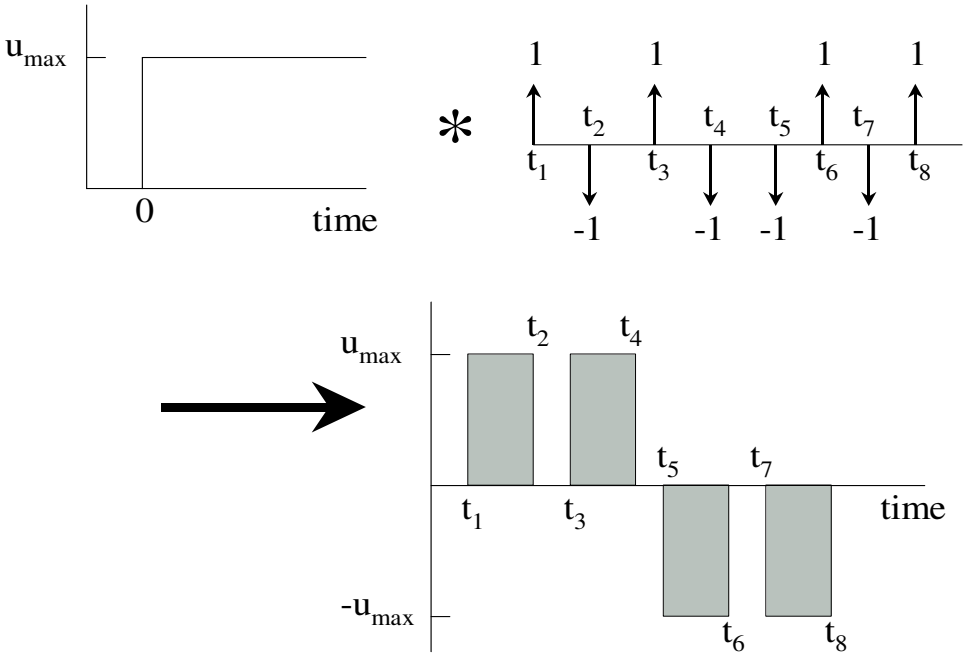

Figure 34: Analytic On-Off Commands.

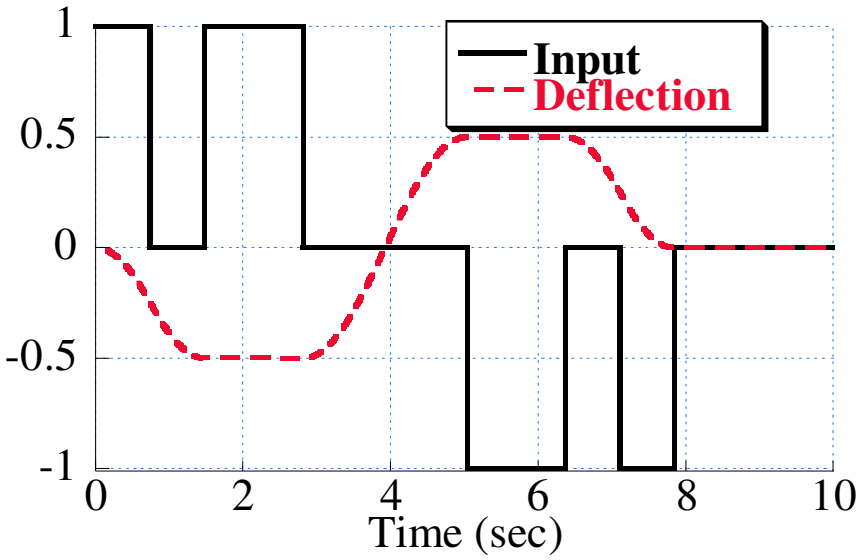

Figure 35: Analytic On-Off Commands - Move Distance = 5.

2.3 Analytic Deflection-Limiting Commands

2.3.1 Deflection-Limiting Transitions

Even in the absence of vibration, a deflection of magnitude $A_i D_{max}/2$ will remain when force is being applied to the system, where D_{max} is given by (24). If $A_i D_{max}/2$ is less than the

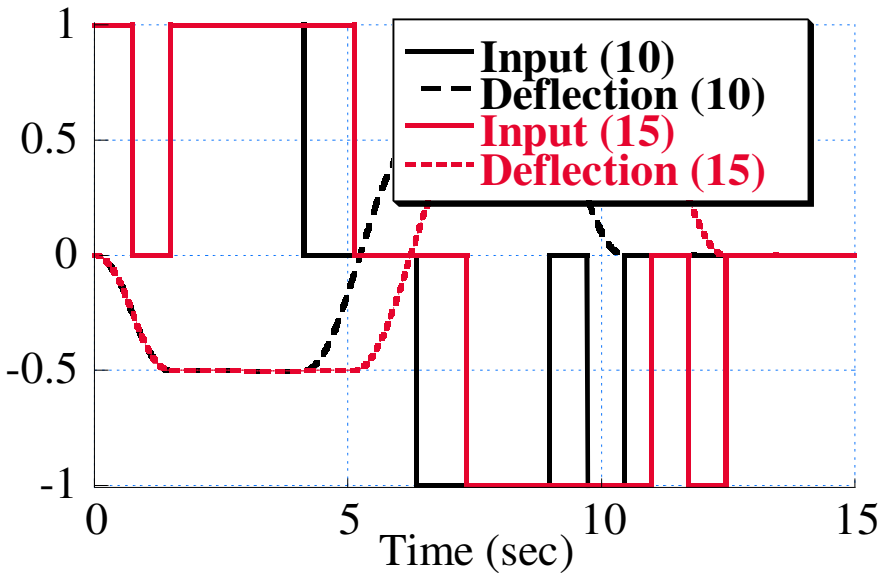

Figure 36: Analytic On-Off Commands for Various Move Distances.

deflection limit, then previously reported techniques for creating analytic on-off commands can be used. When this is not the case, there are two ways to meet this goal: adjust the physical parameters or adjust the constraints on impulse amplitudes. Adjusting the system parameters has consequences beyond transient deflection, so it is a more difficult solution. Adjusting the impulse amplitudes is easily done with few, if any, negative consequences. For the constraints to be met,

$$\frac{D_{max}}{2}\sum_{i=1}^{n} A_i[\cos(w(t-t_i))-1] \leq D_{lim} \tag{54}$$

where D_{lim} is the deflection limit. This must hold for the time after transition 1. This can be accomplished by modifying the impulse amplitude constraint to be

$$\sum A_i \leq 2\left(\frac{D_{lim}}{D_{max}}\right) \tag{55}$$

resulting in a Deflection-Limiting ZV shaper to a form shown in Figure 37. We can now solve for A_3 using

$$a_3 = 2\left(\frac{D_{lim}}{D_{max}}\right) \tag{56}$$

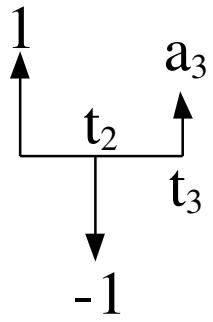

Figure 37: Deflection-Limiting Zero Vibration Shaper.

With the impulse amplitudes set by Figure 37 and (2) and (3), the zero vibration constraints are

$$1 - \cos(\omega t_2) + a_3 \cos(\omega t_3) = 0 \tag{57}$$

$$-\sin(\omega t_2) + a_3 \sin(\omega t_3) = 0 \tag{58}$$

These equations can be solved for t_2 and t_3 to get

$$t_2 = \arccos[(0.5 + \left(2 - 2\left(\frac{D_{lim}}{D_{max}}\right)^2\right)]/\omega \tag{59}$$

$$t_3 = \arccos\left(\frac{D_{lim}}{D_{max}}\right)^2 /\omega \tag{60}$$

The time locations of the impulses of the Deflection-Limiting ZV shaper have a strong dependence on the deflection limit, as shown in Figure 38. As the deflection limit is decreased, the t_2 decreases and $t_3 - t_2$ increases. This has the effect of shortening the duration of the first pulse in the command and lengthening the coast time before the second pulse, as predicted in [**?**]. Note that the modified negative ZV Shaper is equivalent to the UM-ZV shaper when $D_{lim} = 0.5$.

Transition 2 in the complete command profile can be created by modifying a standard ZV Shaper by using impulses of value A_3 given by

$$\begin{bmatrix} A_i \\ t_i \end{bmatrix} = \begin{bmatrix} -A_3 & -A_3 \\ 0 & T/2 \end{bmatrix} \tag{61}$$

Therefore, t_5 is

$$t_5 = t_4 + T/2 \tag{62}$$

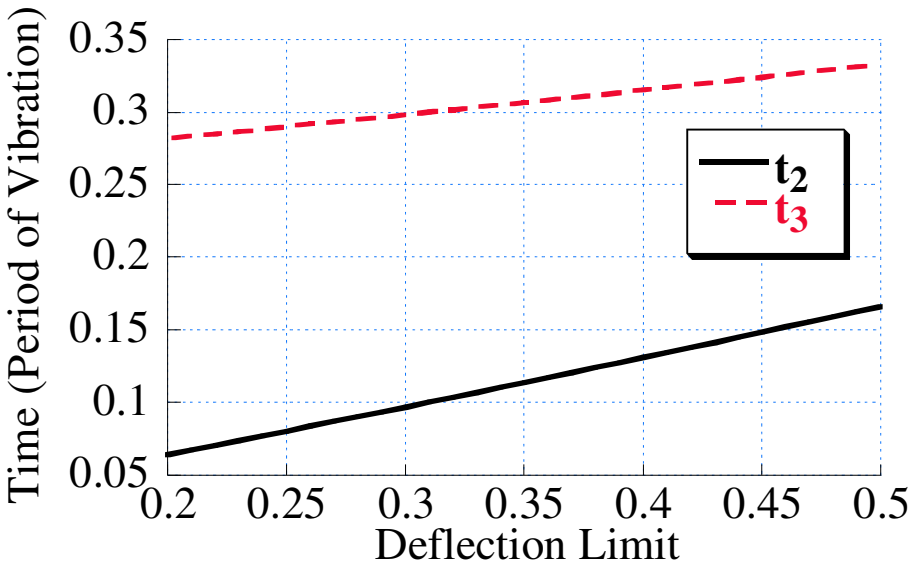

Figure 38: Modified Negative Zero Vibration Shaper Impulse Time Locations as a Function of Deflection Limit.

2.3.2 Forming the Complete Command Profile

Figure 39 shows the command resulting from this formulation. All that is left to be determined is t_4, the duration of the constant acceleration portion of the move. This is done be examining the rigid-body constraints. Looking at only the first half of the move for an undamped system (the second half can be found from symmetry), we know that we must be at the midpoint of the move at the midpoint of the command, therefore

$$x(t_{mid}) = \frac{x_d}{2} \tag{63}$$

where x_d is the desired move distance and t_{mid} is described by

$$t_{mid} = t_4 + \frac{T}{4} \tag{64}$$

By integrating the rigid-body equation of motion with respect to time, an expression for the mass center as a function of switch times is obtained

$$t_4 = \frac{-b + \sqrt{b^2 - 4ac}}{2a} \tag{65}$$

where

$$a = \alpha * D_{lim} \tag{66}$$

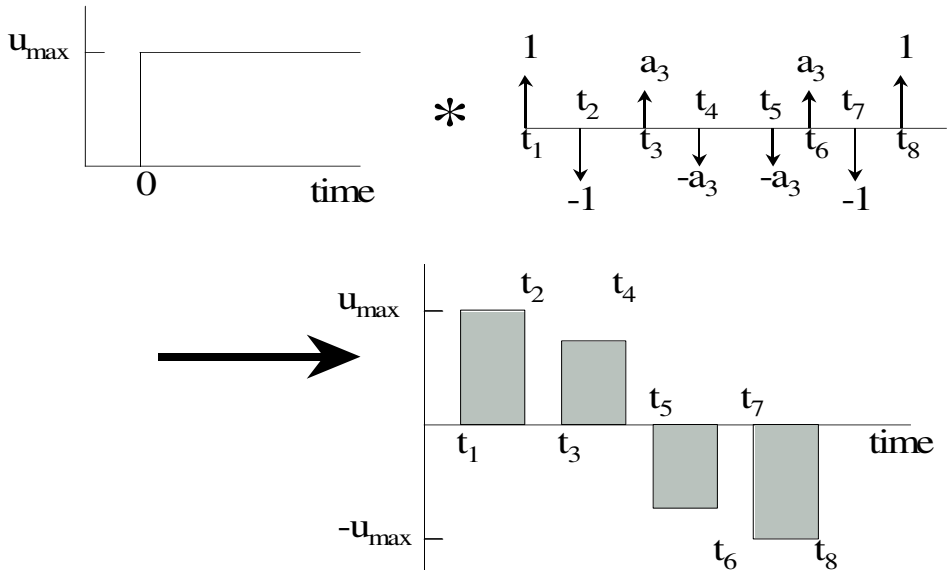

Figure 39: Analytic Deflection-Limiting Command.

$$b = \alpha * (t_2 - 2 * D_{lim} * t_3 + 2 * D_{lim} \frac{T}{4}) \tag{67}$$

$$c = -\frac{\alpha}{2} t_2^2 + \alpha * D_{lim} * t_3^2 + \alpha \left(\frac{T}{4}\right) t_2 - 2 * \alpha * D_{lim} \left(\frac{T}{4} t_3\right) - \frac{x_d}{2} \tag{68}$$

and α is the force-to-mass ratio. Now the complete command shaper can be described by

$$\begin{bmatrix} A_i \\ t_i \end{bmatrix} = \begin{bmatrix} 1 & -1 & A_3 & -A_3 & -A_3 & A_3 & -1 & 1 \\ 0 & t_2 & t_3 & t_4 & t_5 & t_6 & t_7 & t_8 \end{bmatrix} \tag{69}$$

where t_2 - t_5 are as defined above and the remaining times can be found from symmetry:

$$t_8 = 2 * t_{mid} = 2 * t_4 + T/2 \tag{70}$$

$$t_7 = t_8 - t_2 \tag{71}$$

$$t_6 = t_8 - t_3 \tag{72}$$

Figure 40 shows the digital deflection-limiting and analytic deflection-limiting commands and deflection responses of the benchmark system for a move distance of 5 units and a deflection limit of 0.4. The input commands for the two cases are quite similar. The only difference between the two is some rounding of the corners in the digital command. The deflection responses of the two commands are virtually identical. Figure 41 shows that the similarities are repeated for a move distance of 6 units and a deflection limit of 0.3. This

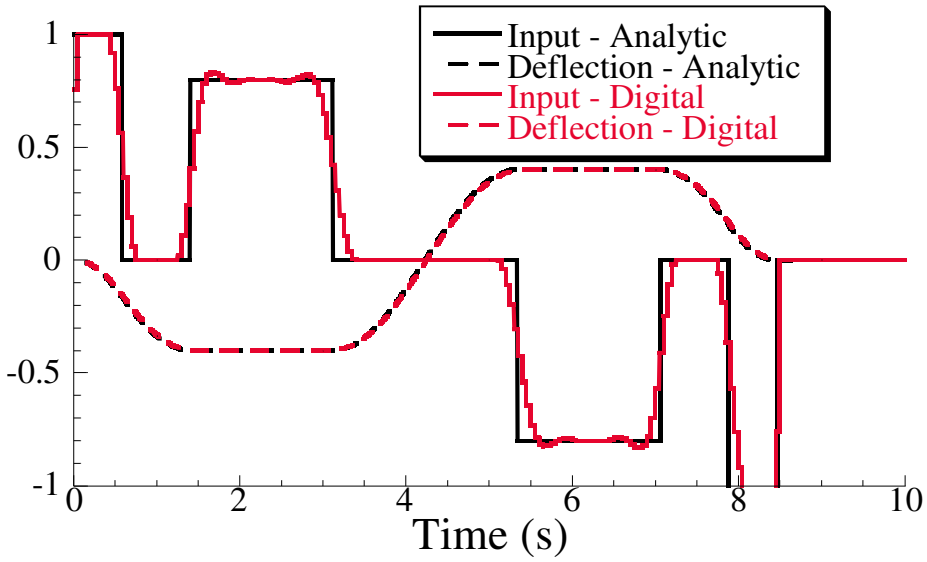

Figure 40: Input and Deflection Response for Move Distance = 5, Deflection Limit = 0.4.

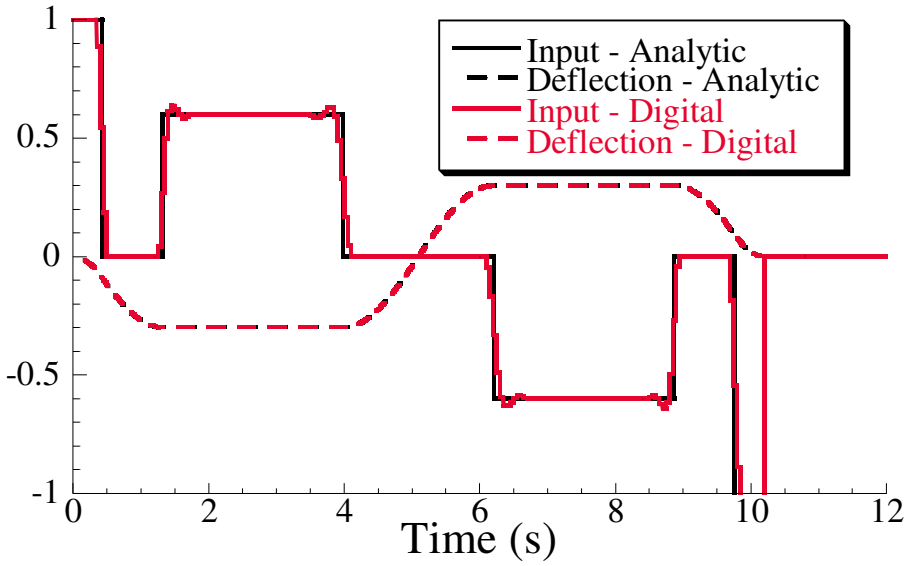

Figure 41: Input and Deflection Response for Move Distance = 6, Deflection Limit = 0.3.

is significant because the digital deflection-limiting commands were shown to be within one digital time spacing of the time-optimal solution [52]. This indicates the closed-form solution obtained here is essentially time-optimal Figure 49 shows that the duration of the analytic commands are less than or equal to the digital command duration over a wide range of deflection limits.

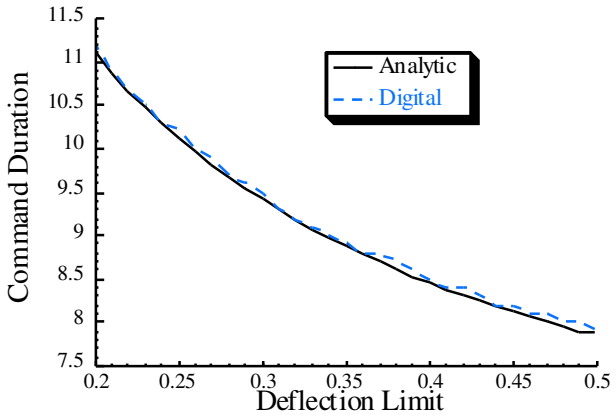

Figure 42: Comparison of Command Durations of Digital and Analytic Deflection Limiting Commands, Move Distance = 5.

2.3.3 Experimental Results

In order to verify the ability of the analytic deflection-limiting command to both eliminate residual vibration and reduce transient deflection, experiments were performed on the 10-ton bridge crane located in the Manufacturing Research Center's high bay on the campus of Georgia Tech. The crane uses two 460-volt AC induction motors on the bridge and one on the trolley. Two Siemens Vector Masterdrives control the bridge and trolley motors. The drives are programmed to track a velocity reference signal sent as an analog voltage from a Siemens CPU 314C-2DP programmable logic controller (PLC). A simple model of the crane is given in Figure 43. Figure 44 shows four commands that were used to move the crane. The first command is a bang-bang acceleration command that is created only considering the rigid-body dynamics. The second command is a fuel-efficient command used to eliminate the residual vibration. The fuel-efficient formulation results in on-off commands. The third command was designed to reduce the transient deflection to 80% of the amount resulting from the fuel-efficient command and the fourth reduces the transient deflection to 60% of the amount resulting from the fuel-efficient command. The velocity commands that correspond to these acceleration profiles are shown in Figure 45. These are the commands that were actually sent to the motor drivers. The positions of the trolley and the payload are determined using a Banner LT3 Long-Range Sensor and a Siemens 732-2 machine vision system.

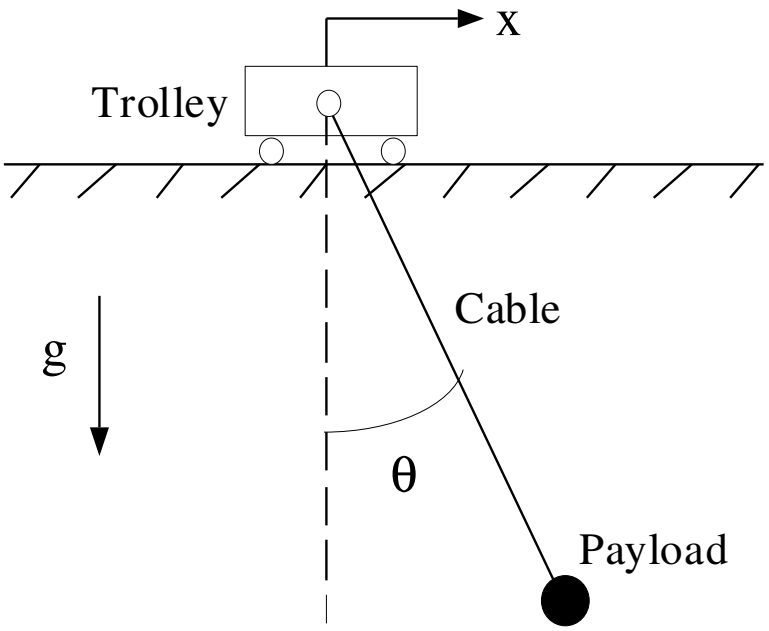

Figure 43: Model of Bridge Crane.

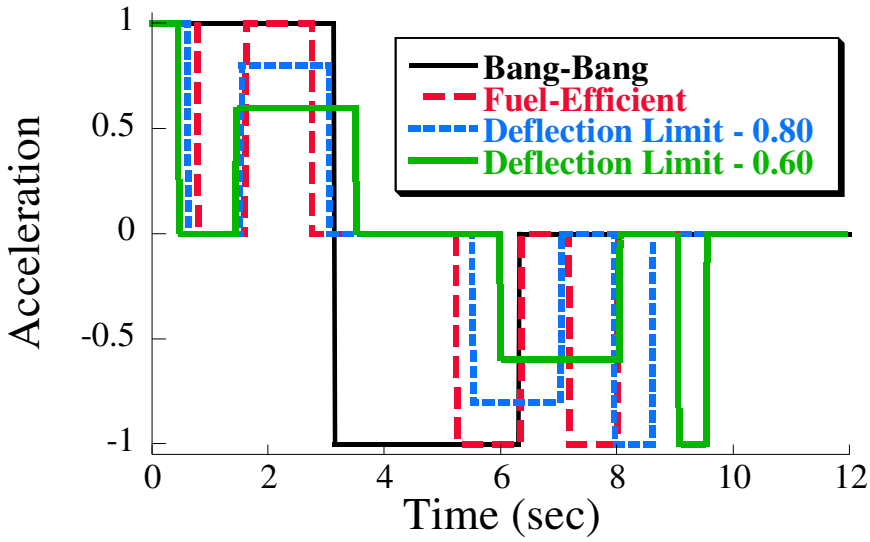

Figure 44: Acceleration Profile for Bridge Crane.

When given the bang-bang command, the payload responds quickly, but oscillates about the final position, as shown in Figure 46. When the fuel-efficient command is used, the system takes a little longer to move the payload, but the payload arrives at the desired location with very little residual vibration. The two deflection-limiting commands also move the system to the desired position with little residual vibration. In addition to the residual

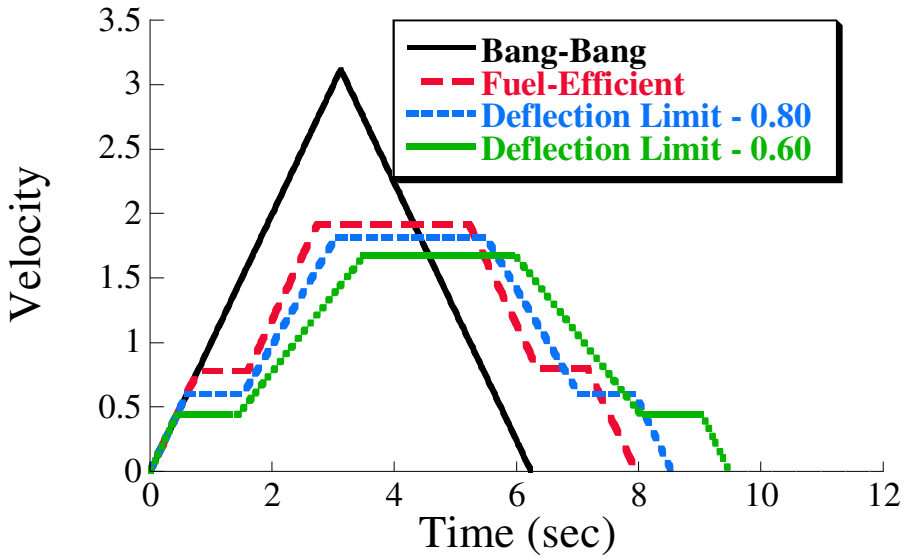

Figure 45: Velocity Profile for Bridge Crane.

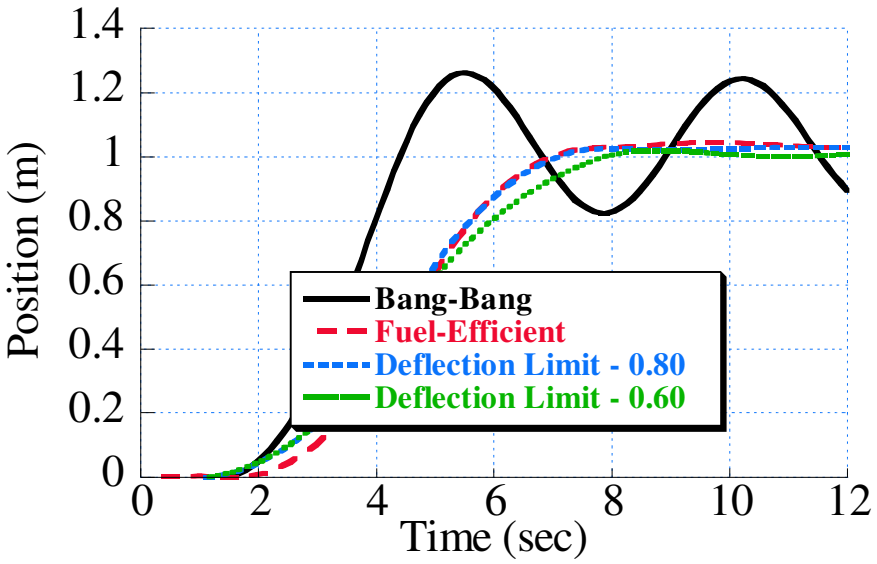

Figure 46: Crane Payload Position.

vibration, the transient deflection was also measured using the vision system. Figure 47 shows the deflection, defined to by the horizontal distance between the trolley and the payload, for the four commands. As expected, the bang-bang command causes large amounts of transient deflection. The maximum amplitude of the bang-bang deflection is 0.23 meters. The fuel-efficient command greatly reduces the transient deflection. The maximum amplitude of the fuel-efficient deflection is 0.12 meters. The maximum amplitude of the

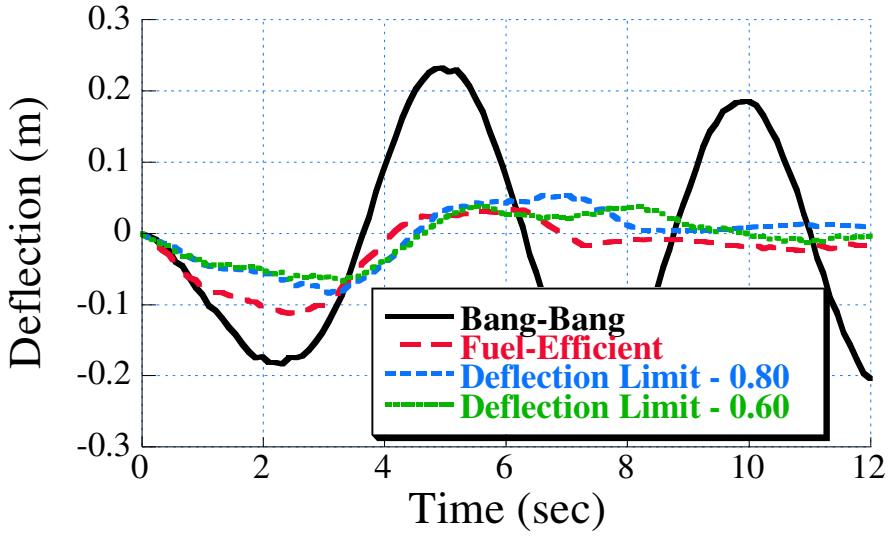

Figure 47: Crane Payload Deflection.

transient deflection deflection-limiting commands are 0.08 meters and 0.06 meters, respectively. Figure 47 clearly shows that the deflection-limiting commands successfully reduce the transient deflection.

2.4 Deflection-Limiting Commands Robustness Analysis

The previous section demonstrated the efficacy of the analytic deflection-limiting commands with a fairly accurate system model. The experimental results then demonstrated their value in the real world when the model was obviously somewhat inaccurate. The current section investigates the performance of the analytic deflection-limiting commands in the presence of significant modeling errors.

2.4.1 Robustness as a Function of Move Distance

In traditional command shaping, the impulse amplitudes and time locations are only functions of the natural frequency and damping ratio. When creating analytic deflection-limiting commands, the impulse amplitudes and time locations are functions of the natural frequency, damping ratio, move distance and deflection limit. This complicates the determination of the robustness of these commands. Figure 48 shows the 5% insensitivity (as defined in Chapter 1) of analytic commands as a function of move distance for a fuel-efficient and a

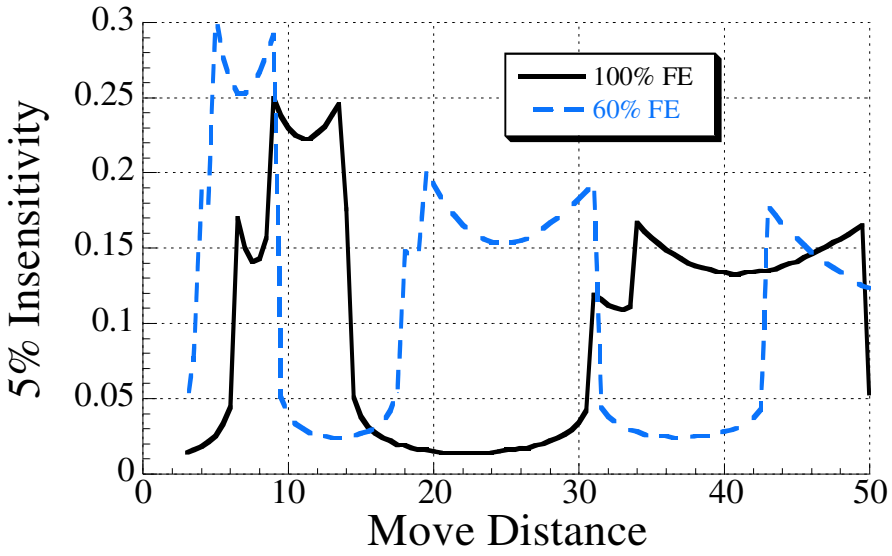

Figure 48: Robustness Analysis of Analytic Commands.

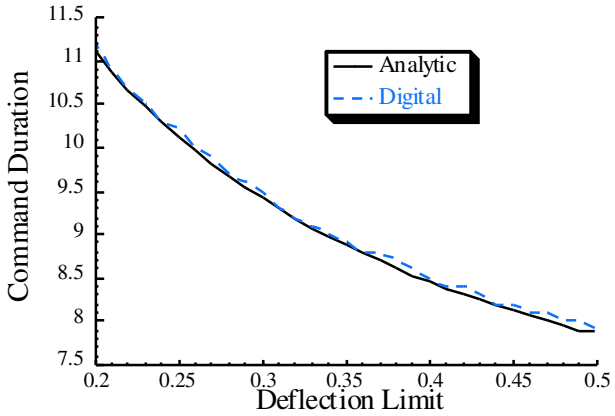

Figure 49: Analytic Deflection-Limiting Commands.

60% deflection-limited command. Clearly there are move distances that are more robust than others and the robustness for a specific move distance varies with the deflection limit. For example, consider a move distance of 10 units. The insensitivity of the Fuel-Efficient command is over six times that of the deflection-limiting command. However, for a move distance of 20 units, the insensitivity of the deflection-limited command is over six times that of the fuel-efficient command. The goal of this section is to understand the source of this variation and to use this knowledge to improve the overall robustness of the analytic commands.

Figure **??** shows a generic analytic deflection-limiting command. When the deflection limit is fixed, but various move distances are considered, only the time between the end of transition 1 and end of transition 2, t_{12}, and the time between the end of transition 2 and end of transition 3, t_{23}, will change. The resultant residual vibration of analytic commands in the presence of modeling errors can be found using (1) or by superimposing the residual vibration of each individual transition. Rather than considering the impulses individually, the transitions, and any vibration at the conclusion of each transition, can be treated as an equivalent "impulse". Now, the variation in robustness as a function of move distance can be explained by considering the relative interference of sine waves. For two sine waves $A_1 sin(\omega t)$ and $-A_2 sin(\omega t + \phi)$, there will be destructive interference when

$$\phi < T/4 \tag{73}$$

or

$$\phi > 3T/4 \tag{74}$$

where T is the vibration period. For the analytic deflection-limiting shapers, if there is some residual vibration after transition 1, there is the chance that it will be reduced by transition 2. Similarly, any residual vibration remaining after transitions 1 and 2 may be reduced by transition 3. This happens when

$$t_{12}, t_{23} < T/4 \tag{75}$$

or

$$t_{12}, t_{23} > 3T/4 \tag{76}$$

This may seem a bit counter-intuitive, but transition 2 has a"negative" equivalent shaper (impulses sum to a negative number). Therefore the commands should be least robust when both t_{12} and t_{23} are in the "constructive" regime and most robust when both times are in the "destructive" regime.

Figure 50 shows t_{12} and t_{23} for the 100% FE case. The"peaks" of the robustness graph correspond to the times when both t_{12} and t_{23} are the "destructive" phase and the "valleys" correspond to the times when both t_{12} and t_{23} are the "constructive" phase. For example,

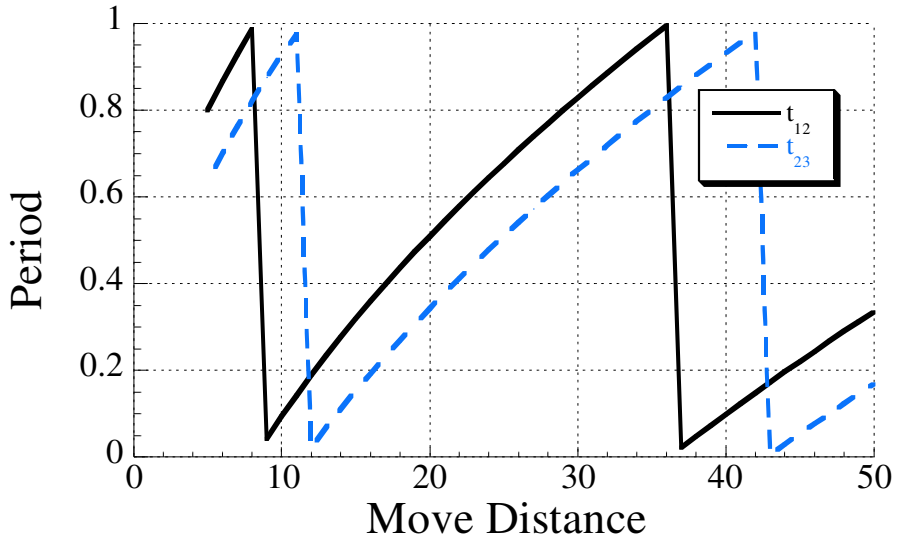

Figure 50: Times Between Transitions for 100% FE Analytic On-Off Commands.

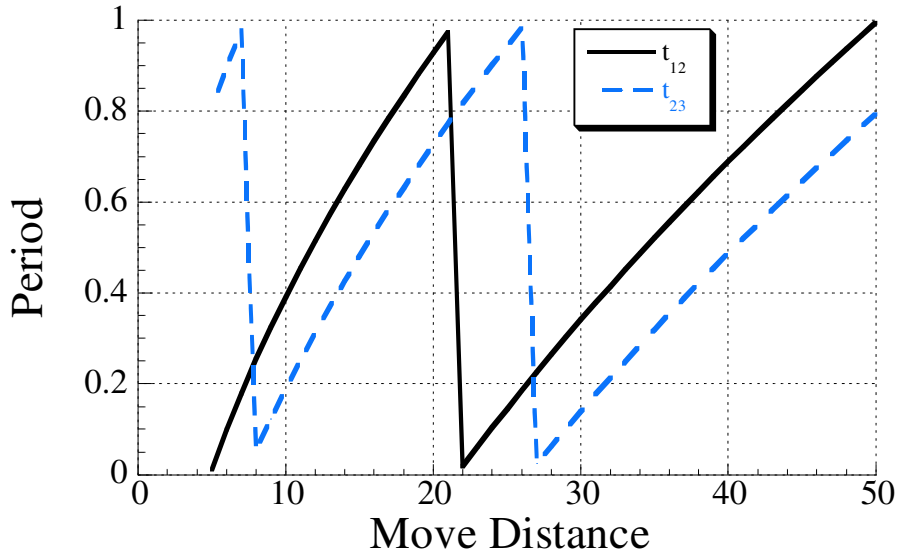

Figure 51: Times Between Transitions for 60% FE Analytic Deflection-Limiting Commands.

consider a move distance of 10 units. Here, $t_{12} = 0.1$ and $t_{23} = 0.9$. Both times are in the "destructive" range. This corresponds to a high insensitivity in Figure 48. For a move distance of 20 units, $t_{12} = 0.5$ and $t_{23} = 0.35$. These times are in the "constructive" range and the insensitivity for this move distance in Figure 48 is one of the lowest. The same holds for the 60% FE times shown in Figure 51.

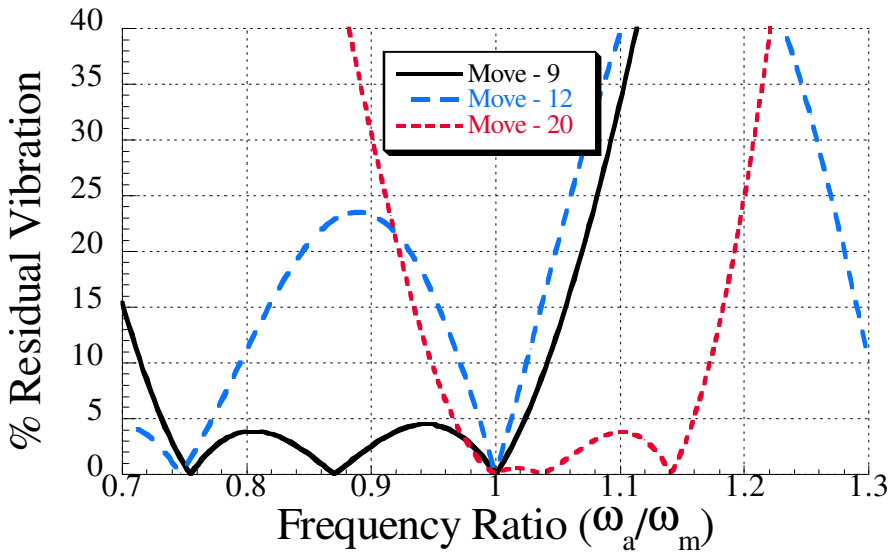

Figure 52: Sensitivity Plots for Three 60% Deflection-Limited Commands.

2.4.2 Symmetric Insensitivity

While it appears that some move distances are more robust than others, the "quality" of the robustness needs to be investigated. In most cases, it is desirable to have a symmetric insensitivity. Figure 52 shows three sensitivity plots for the 60% FE cases; two robust commands (Move - 9 & Move - 20) and one non-robust command (Move - 12). While the Move - 9 (I = 0.28) command and Move - 20 (I = 0.20) commands are more robust than the Move - 12 (I = 0.03) case, the insensivities are heavily skewed to the low side and high side, respectively. In general, the more robust the command, the more skewed the robustness of the command. Figure 53 shows the Insensitivity Ratio - the ratio of the insensitivity above the modeling frequency to the total insensitivity - as a function of move distance for an analytic fuel-efficient command and a 60% deflection-limited command. An insensitivity ratio of 0.5 is a symmetric sensitivity curve. A number greater than 0.5 indicates that the sensitivity is skewed to the high side; a number less than 0.5 indicates that the sensitivity is skewed to the low side. When comparing Figure 48 and Figure 53, it becomes apparent that the "peaks" of the robustness correspond to large deviations from 0.5 insensitivity ratio. In general, commands with large insensitivities will not have well balanced robustness to modeling errors both above and below the modeling frequency.

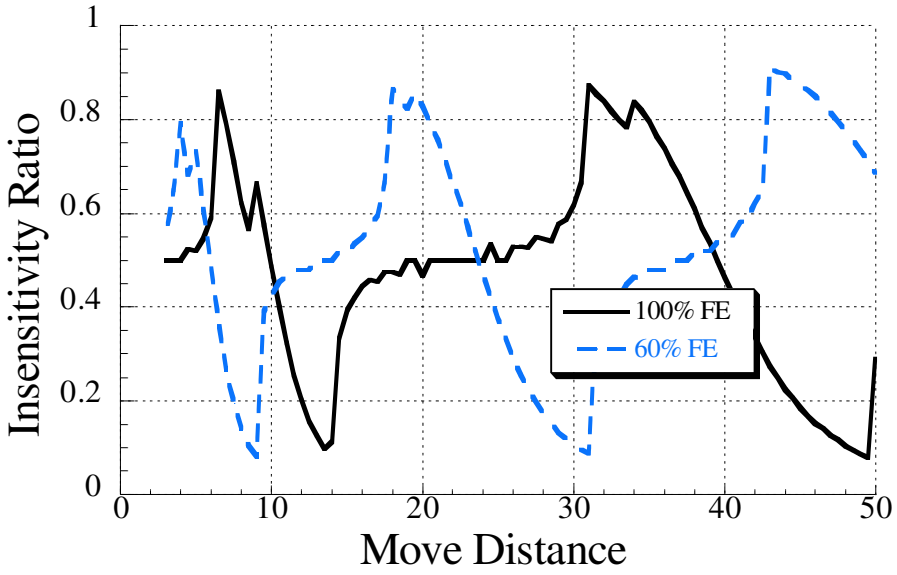

Figure 53: Insensitivity Ratio.

When a more symmetric sensitivity curve is needed, the above results will be misleading. In order to account for the shape of the sensitivity curve, a scaling factor can be introduced to the traditional robustness measure

$$TrueRobustness = (1 - 2 * w_{skew}|x - 0.5|) * Robustness \tag{77}$$

where x is the insensitivity ratio developed in Figure 53 and w_{skew} is a weighting factor between 0 and 1. If a symmetric sensitivity curve is not needed, then w_{skew} may be set to zero and the calculated robustness will not change. If a symmetric sensitivity curve is mandatory, then w_{skew} may be set to 1. For more moderate levels of desired symmetry, w_{skew} may be anywhere in between. Figure 54 shows the new robustness measurements for $w_{skew} = 0.5$ and $w_{skew} = 1$. Increasing w_{skew} reduces the height and the width of the peaks while increasing the width of the valleys. Using the weighting factor yields more reasonable measures of robustness when considering the desired level of symmetry.

2.4.3 Robustness Compared to Bang-Bang Commands

Equation 1 gives the ratio of the vibration resulting from a shaped command (series of impulses) to that of the unshaped command (single impulse). However, for rest-to-rest

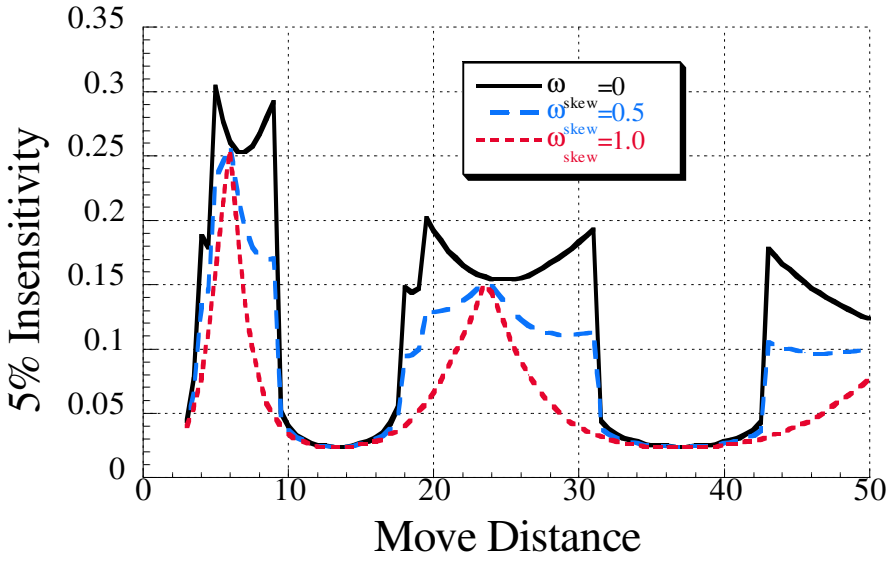

Figure 54: Robustness of 60% Deflection-Limited Command using Symmetric Weighting Factor.

moves, comparing the residual vibration to that of a single impulse does not take into account the effect of move distance. The unshaped command should move the system the required distance, something a single impulse cannot do. For the benchmark system addressed in this chapter, a bang-bang command is used as the unshaped command.

There is one difficulty with using a bang-bang command as the baseline, unshaped command. Unlike a single impulse which will always induce a non-zero residual vibration, there exists some move distances for which a bang-bang command will result in zero vibration [61]. The switch time for a bang-bang command can be found by

$$t_2 = \sqrt{x_d/\alpha} \tag{78}$$

where x_d is the desired move distance and α is the force-to-mass ratio. A bang-bang command will induce zero vibration when

$$t_2 = nT \tag{79}$$

where n is a positive integer and T is the period of vibration. Combining (78) and (79) gives the move distances for which the vibration will be zero

$$x_d = \alpha(nT)^2 \tag{80}$$

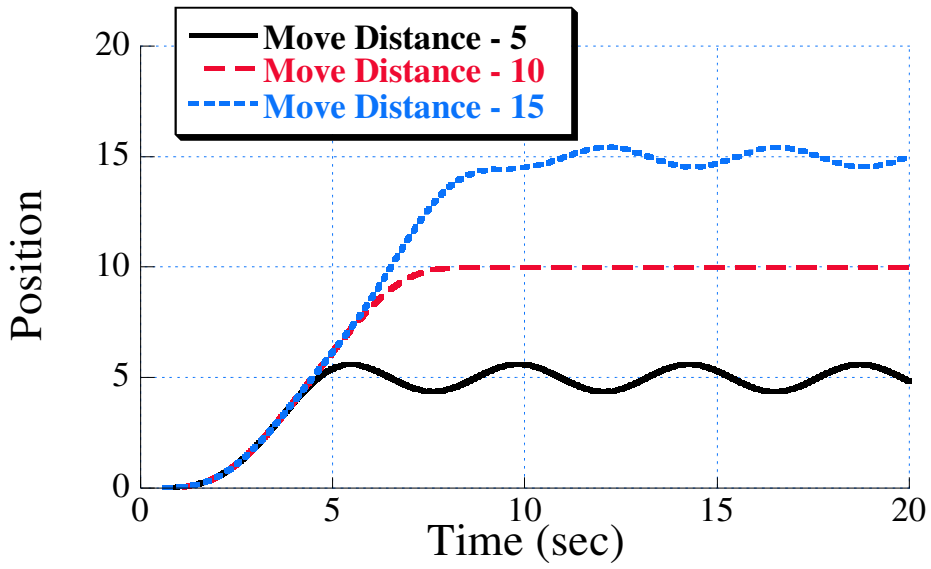

Figure 55: Position Response to Bang-Bang Command.

For the benchmark system with $\alpha = 0.5$ and $T = 4.425$ seconds, the first three move distances for which a bang-bang command will have zero vibration are 9.868, 39.472 and 88.811. If the residual vibration percentage for rest-to-rest commands is defined as the vibration of a shaped command to that of a bang-bang command, then these move distances will yield undefined percent vibration given the zero residual vibration from the bang-bang command. Figures 55 and 56 show the position and deflection resulting from a bang-bang command for a move distance of 5, 10 and 15 units. There is considerable residual vibration for the moves of 5 and 15 units. There is very little vibration for the 10-unit move given its close proximity to the first zero vibration move distance of 9.868.

A plot of the robustness measure using the bang-bang as the unshaped command, as opposed to a single impulse, is shown in Figure 57 for a move distance of 5 units. For this move distance, the 60% deflection limit command is much more robust than that of the 100% Fuel-Efficient command. However, the 100% Fuel-Efficient command is more robust than the 60% deflection limit command for a move distance of 15, as shown in Figure 58. The relative levels of robustness when using a bang-bang input as the standard unshaped command follow the trends shown in Figure 48. Therefore, while using the traditional residual vibration robustness measure does not take into account the fact that the move

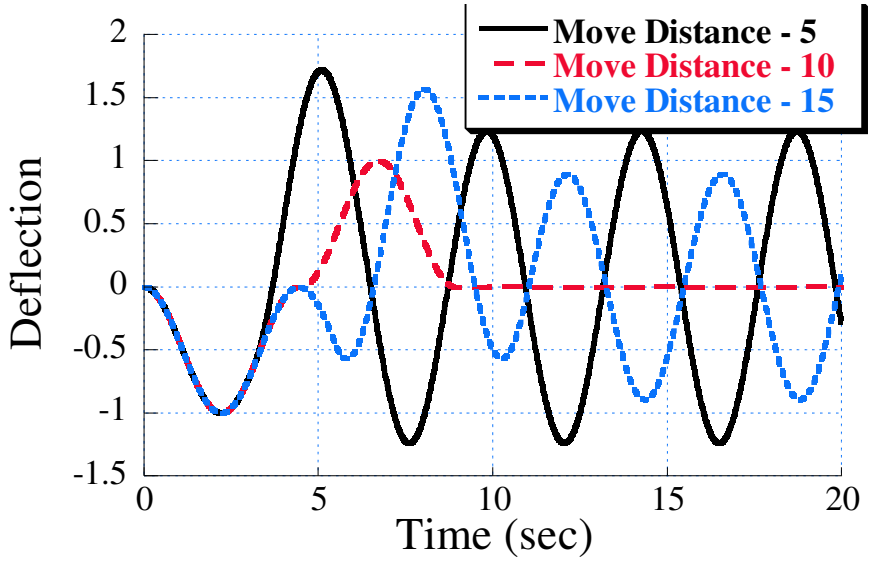

Figure 56: Deflection Response to Bang-Bang Command.

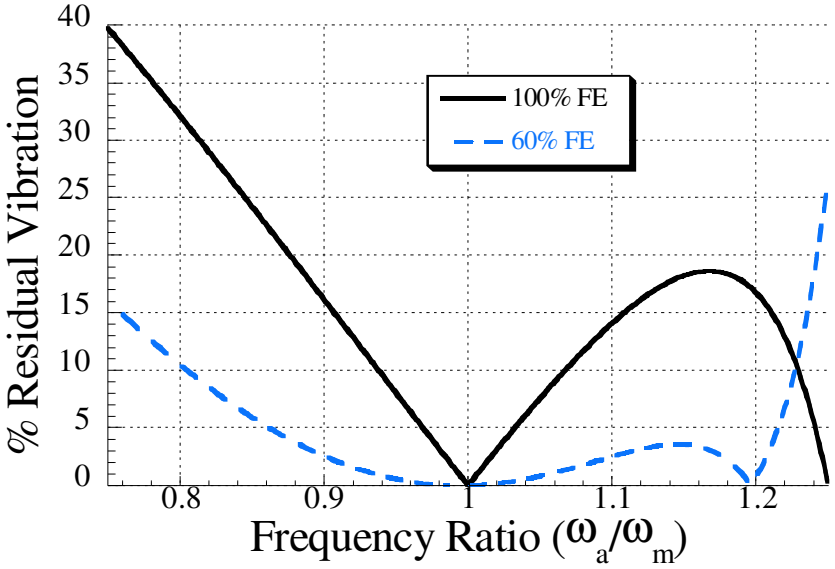

Figure 57: Robustness Relative to Bang-Bang Command, Move Distance - 5.

distance is a constraint, as well as the natural frequency, its results follow the same trends as the robustness measure that does account for move distance and it avoids cases where the robustness would be undefined.

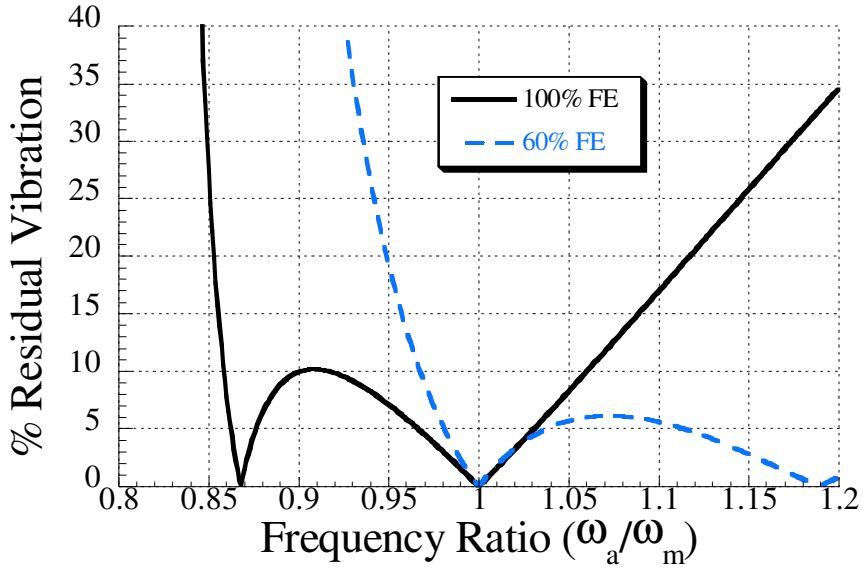

Figure 58: Robustness Relative to Bang-Bang Command, Move Distance - 15.

2.4.4 Effect of Modeling Errors on Transient Deflection

It may not be entirely appropriate to use residual vibration reduction as the primary measure of robustness for commands whose primary goal is limiting transient deflection. At the very least, percent residual vibration does not tell the entire story. One alternative is to use the percent by which the deflection exceeds the desired deflection limit. That is, a measure of how modeling errors effect the transient performance.

Figure 59 shows the deflection in the presence of modeling errors for a move distance of 5 units and a deflection limit of 0.3. When the actual frequency is higher than the model frequency, the deflection remains below the limit. When the actual frequency is lower than the model frequency, the deflection exceeds the limit. For this particular case, underestimation of the natural frequency does not cause the system to exceed the deflection limit.

This trend does not hold for all cases, however. Figure 60 shows the deflection in the presence of modeling errors for a move distance of 10 units and a deflection limit of 0.3. Here, both an overestimation or an underestimation in natural frequency will result in commands that exceed the deflection limit. Figure 61 shows the effect of modeling errors have on the amount the transient deflection exceeds the deflection limit of 60% Fuel-Efficient for move

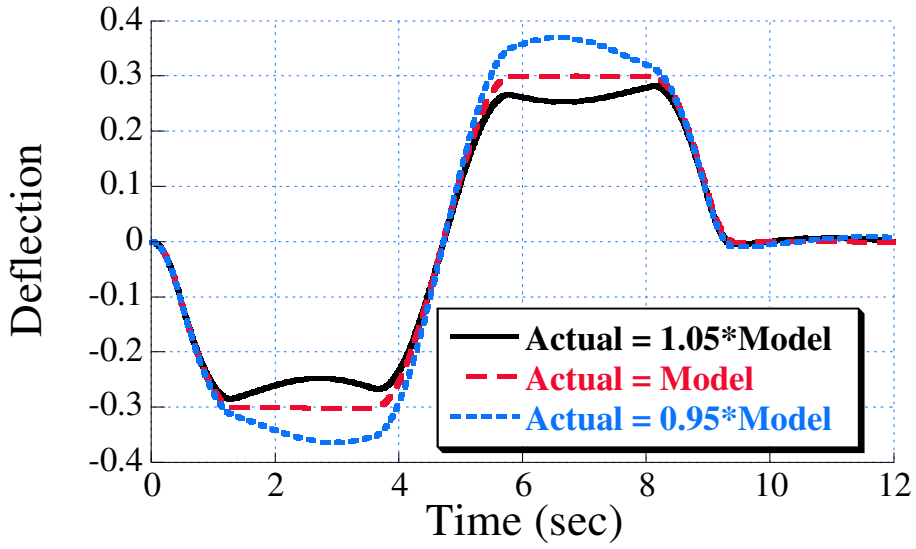

Figure 59: Deflection Response of 60% Deflection-Limited Command, Move Distance - 5 Units.

distances of 5, 10, 15 and 20 units. For all move distances, overestimating the natural frequency by as little as 2% will lead to commands that exceed the deflection limit by at least 10%. Underestimating the natural frequency has such dramatic effects on transient performance in only the 10 and 15 unit moves, while such errors have little effect on the 5 and 20 unit moves. Recall that on Figure 48 the 5 and 20 unit moves were much more robust, in a residual vibration sense, than the 10 and 15 unit moves.

2.5 Creating Robust Transitions for Analytic Deflection-Limiting Commands

The previous section investigated the robustness of the analytic deflection-limiting commands as a function of move distance. Figure 48 showed that for a specific deflection limit there are certain move distances that very robust and some move distances that are not very robust. In this section we develop new transitions in an attempt to "fill in the valleys" in Figure 48.

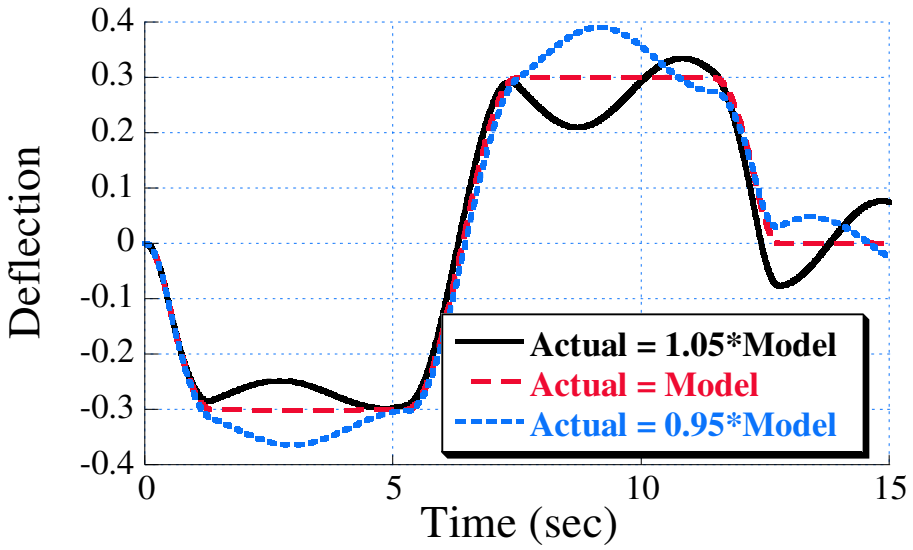

Figure 60: Deflection Response of 60% Deflection-Limited Command, Move Distance - 5 Units.

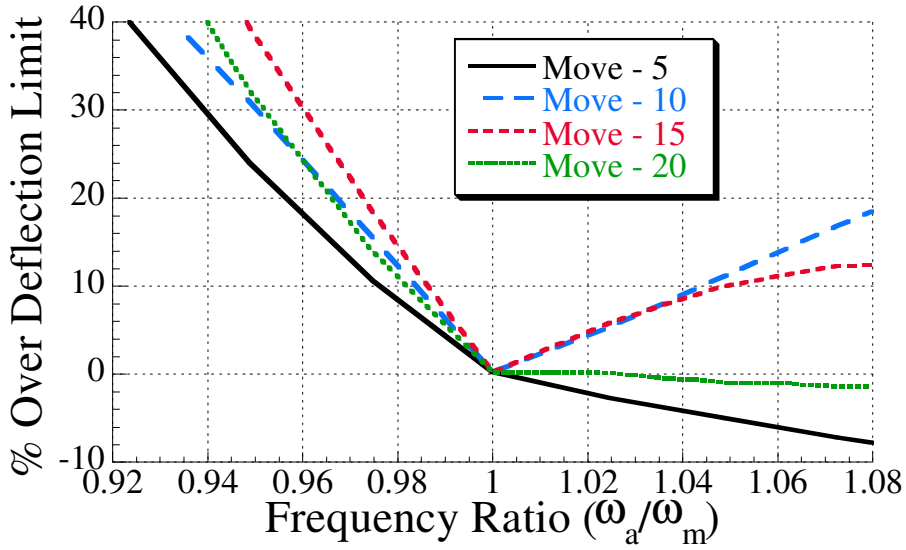

Figure 61: Transient Deflection Robustness of 60% Deflection-Limited Command.

2.5.1 Two-Unit Transitions

2.5.1.1 Modified UM-ZVD Shaper

The earlier section showed that two-unit transitions (transitions from acceleration to deceleration) can be easily created. Equation 61 gave the impulse amplitudes and time locations for a modified, two-unit ZV shaper that could be used for such a transition. Figure 9 in the

Introduction chapter showed that near the model frequency, the robustness of the UM-ZV shaper is equivalent to that of the ZV shaper. This section introduces a modified two-unit UM-ZVD shaper given by

$$\begin{bmatrix} t_i \\ A_i \end{bmatrix} = \begin{bmatrix} 0 & t_2 & t_3 & t_4 & t_5 \\ -2A_3 & 2A_3 & -2A_3 & 2A_3 & -2A_3 \end{bmatrix} \tag{81}$$

where t_2-t_5 can be determined by the method described in [65]. When combined with the modified UM-ZV shaper defined by (56), (59) and (60), the analytic deflection-limiting command is described by

$$\begin{bmatrix} t_i \\ A_i \end{bmatrix} = \begin{bmatrix} 0 & t_2 & t_3 & t_4 & t_5 & t_6 & t_7 & t_8 & t_9 & t_{10} & t_{11} \\ 1 & -1 & A_3 & -2A_3 & 2A_3 & -2A_3 & 2A_3 & -2A_3 & A_3 & -1 & 1 \end{bmatrix} \tag{82}$$

Using the move distance constraint given in (63) and solving for t_4 yields

$$t_4 = \frac{-b + \sqrt{b^2 - 4ac}}{2a} \tag{83}$$

where

$$a = 0.5 * A_3 \tag{84}$$

$$b = t_2 + A_3(-t_3 + 0.3661T) \tag{85}$$

and

$$c = t_2(0.3661 * T - 0.5 * t_2) + A_3(0.0095 * T^2 - 0.3661 * T * t_3 + 0.5 * t_3^2) - x_d \tag{86}$$

where T is the vibration period.

Figure 62 showed the 5% Insensitivity as a function of move distance for the UMZV-ZV-UMZV commands (modified negative shapers for transitions 1 and 3, and a ZV shaper for transition 2) presented in the earlier section and the UMZV-UMZVD-UMZV commands (modified negative shapers for transitions 1 and 3, and a UMZVD shaper for transition 2) derived here. While the "valleys" of the UMZV-UMZVD-UMZV commands aren't as deep or wide as the UMZV-ZV-UMZV commands, the "peaks" aren't as high either. Increasing the robustness of the two-unit transition alone does not increase the overall robustness of the analytic deflection-limiting commands. The next section will combine a modified negative ZVD shaper for one-unit transitions will the two-unit UM-ZVD transition presented in this section.

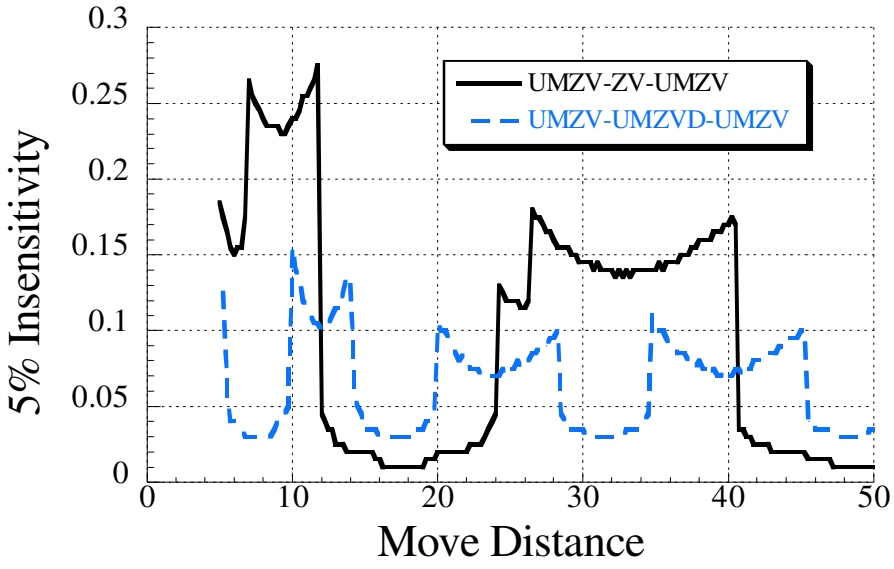

Figure 62: 5% Insensitivity of 60% Deflection-Limited Commands.

2.5.2 One-Unit Transitions

2.5.2.1 Modified Negative ZVD Shaper

Figure 37 shows the modified negative ZV shaper used to create the one-unit transition (transitions 1 and 3). In an effort to increase the robustness, the modified negative ZVD shaper shown in Figure 63 will be used for the one-unit transition. The amplitude of A_5 can be found using

$$A_5 = 2\left(\frac{D_{lim}}{D_{max}}\right) \tag{87}$$

The impulse times can be found using the zero vibration and derivative constraints given by

$$1 - \cos(\omega t_2) + \cos(\omega t_3) - \cos(\omega t_4) + A_5 \cos(\omega t_5) = 0 \tag{88}$$

$$-\sin(\omega t_2) + \sin(\omega t_3) - \sin(\omega t_4) + A_5 \sin(\omega t_5) = 0 \tag{89}$$

$$-t_2 \cos(\omega t_2) + t_3 \cos(\omega t_3) - t_4 \cos(\omega t_4) + A_5 t_5 \cos(\omega t_5) = 0 \tag{90}$$

$$t_2 \sin(\omega t_2) - t_3 \sin(\omega t_3) + t_4 \sin(\omega t_4) - A_5 t_5 \sin(\omega t_5) = 0 \tag{91}$$

Figure 64 shows the these times as a function of deflection limit. Rather than solving (88)-(91) for t_2 - t_5, a curve fit for the trends shown in Figure 64 can be used. A second

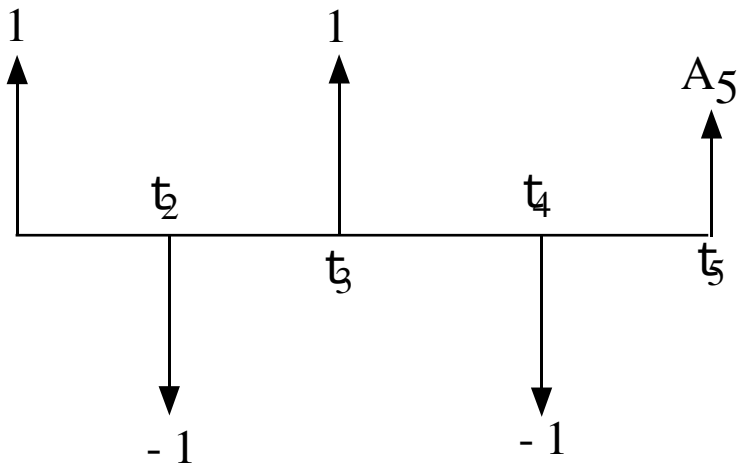

Figure 63: Modified Negative Zero Vibration and Derivative Shaper.

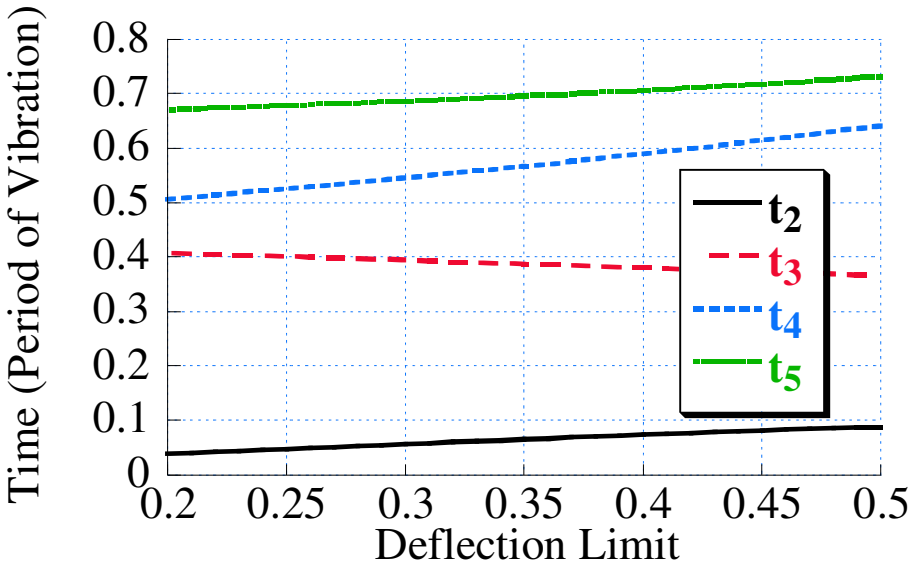

Figure 64: 5% Insensitivity of 60% Deflection-Limited Commands.

order polynomial of the form $t_i = a * D_{lim}^2 + b * D_{lim} + c$ (R=0.9999) was used. The values for a, b and c for each impulse is given in Table 2.

When combined with the two-unit UM-ZVD presented in the previous section, the complete command is described by

$$\begin{bmatrix} 0 & t_2 & t_3 & t_4 & t_5 & t_6 & t_7 & t_8 & t_9 & t_{10} & t_{11} & t_{12} & t_{13} & t_{14} & t_{15} \\ 1 & -1 & 1 & -1 & A_5 & -2A_5 & 2A_5 & -2A_5 & 2A_5 & -2A_5 & A_5 & -1 & 1 & -1 & 1 \end{bmatrix} \tag{92}$$

Table 2: Curve Fit for Modified UM-ZVD Shaper Impulse Times.

	a	b	c
t_2	-7e-6	-0.0015	0.0912
t_3	-4e-6	0.0015	0.3649
t_4	3e-5	-0.0055	0.6475
t_5	-2e-5	0.0028	0.7346

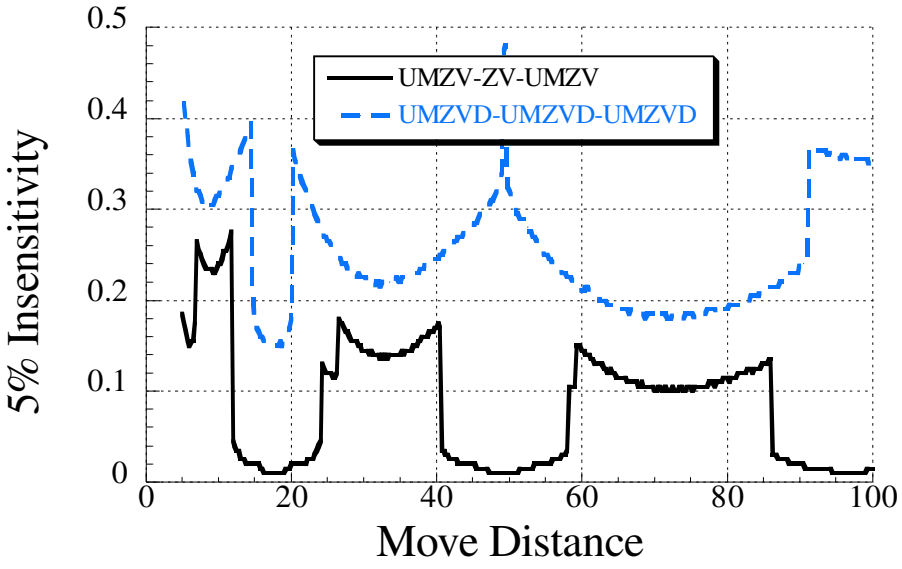

Figure 65: 5% Insensitivity of 60% Deflection-Limited Commands.

Using the move distance constraint given in (63) and solving for t_6 yields

$$t_6 = \frac{-b + \sqrt{b^2 - 4ac}}{2a} \tag{93}$$

where

$$a = 0.5\alpha A_5 \tag{94}$$

$$b = \alpha(t_2 - t_3 + t_4 + A_5(-t_5 + 0.3572T)) \tag{95}$$

and

$$c = \alpha(0.5(-t_2^2 + t_3^2 - t_4^2 + a_5 t_5^2) + 0.3572T(t_2 - t_3 + t_4) + a_5(0.00786838T^2 - 0.3572T t_5)) - x_d/2 \tag{96}$$

where T is the vibration period. The times for the two-unit UM-ZVD shaper can be found using the techniques detailed in [65] and t_{11} - t_{15} can be found from symmetry.

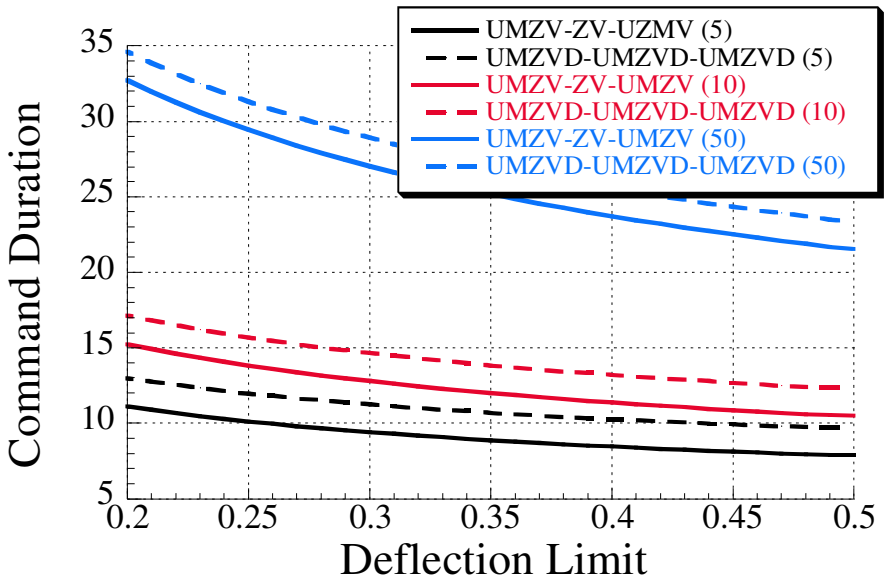

Figure 66: Command Duration of Analytic Deflection-Limiting Commands.

Figure 65 compares the 5% Insensitivity for UMZV-ZV-UMZV and UMZVD-UMZVD-UMZVD commands. On average for the range shown, the robust commands are over nine times more robust than the non-robust commands. This increase in robustness does not come without a cost. Figure 66 shows the command durations for move distances of 5, 10 and 50 units. The percent increase in command durations decreases as move distance increases. Figure 67 shows the difference in durations of the non-robust and robust commands. The difference is relatively close to the sum of the differences of the durations of the individual transitions. That is, the differences in command durations can be attributed to the differences in durations of the UMZV and the UMZVD commands. As shown in Figures 38 and 64, the modified negative ZV and the modified negative ZVD shaper durations do lengthen slightly with the deflection limit. This effect can also be seen in Figure 67.

2.6 Deflection-Limited Electrodynamic Reboost

Command shapers of the form shown in Figure 37 can be used for a variety of systems beyond the benchmark models shown is Figure 33 and for a variety of uses beyond deflection-limited rest-to-rest moves. These shapers can also be used to reduce the deflection of an electrodynamic tether during reboost.

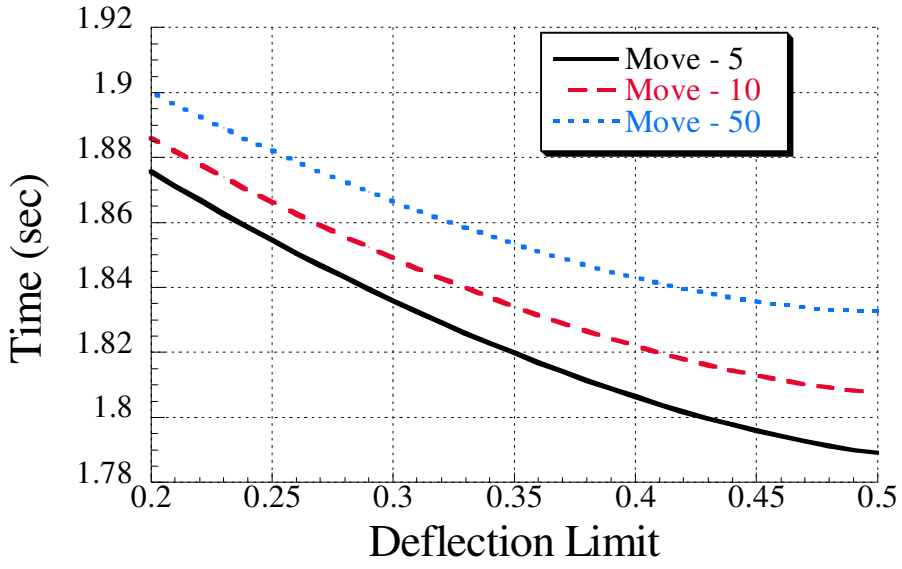

Figure 67: Difference in Durations of UMZV-ZV-UMZV and UMZVD-UMZVD-UMZVD Commands.

Figure 68 shows a model for an electrodynamic tether. The tether is 2000 meters long with stiffness, EA, of 10000 Newtons, lines density of 0.001 kg per meter and a subsatellite mass of 500 kg in a 200 km circular orbit. The tether is modeled as 10 lumped mass segments connected by massless springs and perfect revolute. To initiate the reboost process, a current is run through the tether. When a simple, unshaped command (such as a step change in current) is used, large vibrations in the tether may result. Figure 69 shows the tether midpoint deflection from the local horizontal during the electrodynamic reboost. The unshaped response displays a large libration and a string vibration mode. A ZV shaper can be used to cancel the libration. This reduces the peak-to-peak amplitude of the vibration by 70% as shown in Figure 69. While the amplitude of the deflection has been decreased dramatically, the string vibration still exists. An Extra-Insensitive (EI) shaper for the string vibration can be combined with the ZV for the libration to eliminate the two dominate vibration modes. Figure 69 shows that this solution works very well.

Using multi-mode shaping allows for a relatively vibration-free electrodynamic reboost. However, the tether mid-point displacement of 78 meters may be unacceptably large. The modified negative ZV shaper developed in the previous section can be used to cancel the

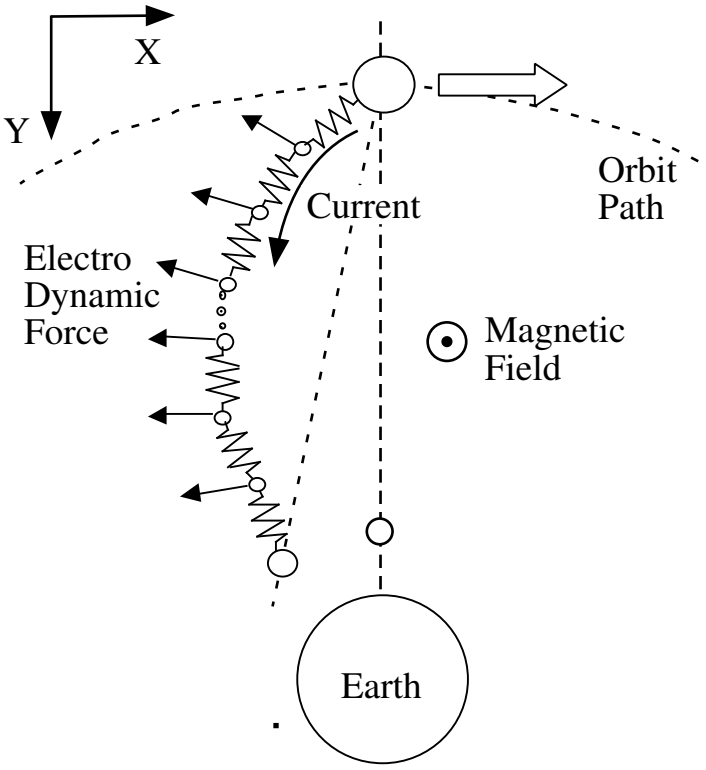

Figure 68: Model of Electrodynamic Tether

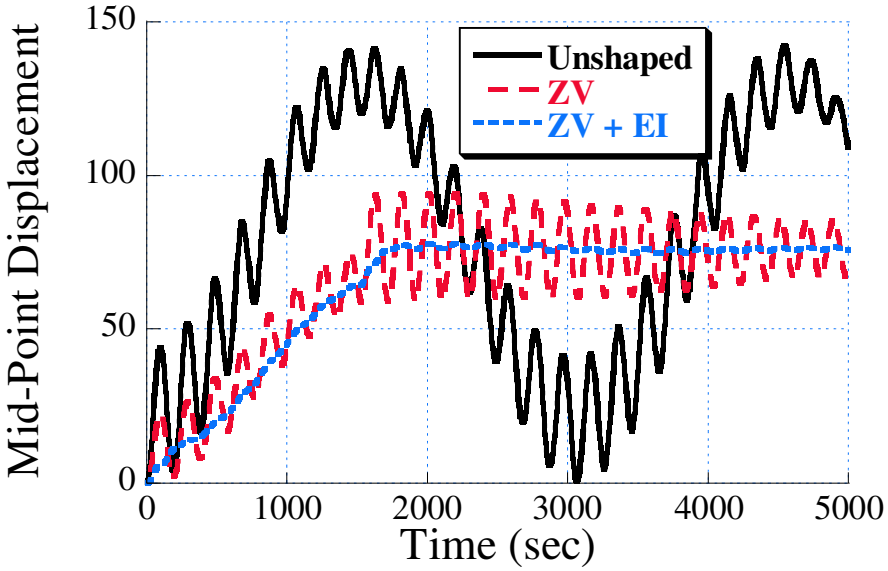

Figure 69: Electrodynamic Tether Mid-Point Response During Reboost.

libration and limit the mid-point displacement. Figure 70 shows the tether mid-point displacement using a 80% Deflection-Limiting shaper. The overall responses are similar to those shown in Figure 69 except that the amplitude of the mid-point deflection has been

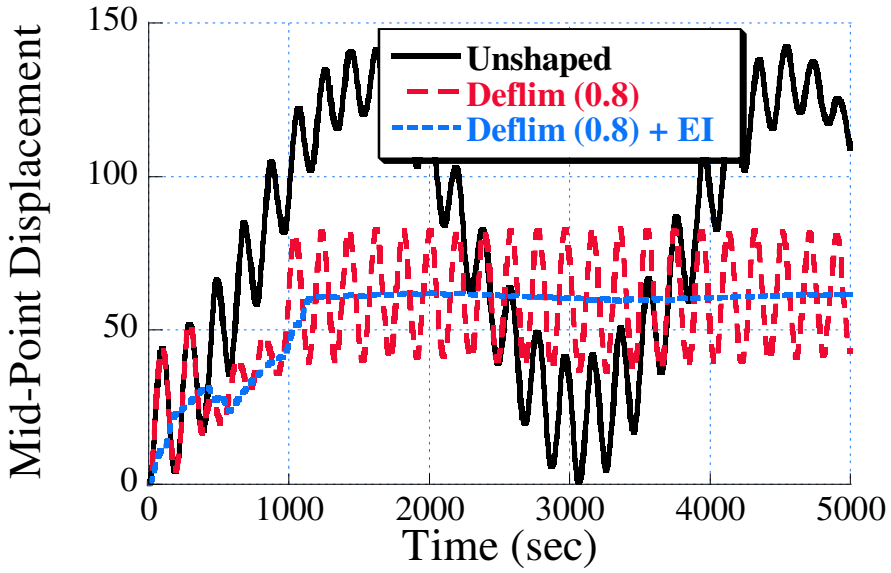

Figure 70: Deflection-Limited Electrodynamic Reboost.

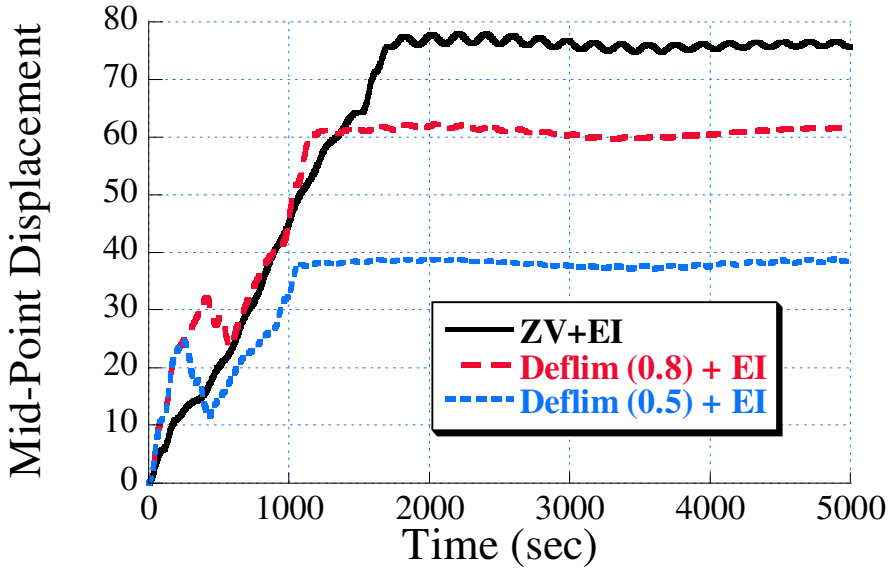

Figure 71: Comparison of Tether Mid-Point Deflection During Electrodynamic Reboost.

reduced by approximately 20% as intended.

The demonstrate more clearly the effectiveness in theDeflection-Limiting shapers to reduce the tether mid-point displacement Figure 71 shows the tether response for three multi-mode shapers. Using a traditional ZV shaper results in a mid-point deflection of 78 meters. The 80% and the 50% modified negative ZV shapers reduce the mid-point displacement to 61 and 38 meters, respectively.

2.7 Analytic Deflection-Limiting Commands Summary

In this chapter analytic deflection-limiting commands were derived and experimentally verified. The robustness characteristics of these commands were investigated. The major contributions of this chapter are as follows:

- Creation of Specified Deflection, Zero Vibration command shapers for a mass under PD control
- Derivation of Analytic Deflection-Limiting Commands
- Experimental Verification of Analytic Deflection-Limiting Commands
- Development of Analysis Tools for Rest-to-Rest Deflection-Limiting Commands
- Creation of robust transitions for Analytic Deflection-Limiting Commands
- Demonstration of the utility of deflection-limiting command shapers for Electrodynamic Reboost

CHAPTER III

TETHERED SATELLITE RETRIEVAL

There has been a significant amount of research in the dynamics and control of tethered satellite systems. Such systems can be used to conduct ionospheric or gravity gradient experiments, deploy or retrieve satellites, or construct large space structures. The major research results indicate that the stationkeeping phase is marginally stable; deployment can become unstable if a critical speed is exceeded; and the retrieval phase is always unstable [38]. One of the biggest concerns with tethered satellites is preventing tether slackness. Consequently, there have been many control methods proposed for tethered satellites. In particular, methods have been developed for deployment [38, 41, 78, 32, 45, 30, 42] stationkeeping [38, 31] and retrieval [38, 41, 78, 45, 31, 49, 25]. Given the inherently unstable nature of the tether retrieval process, the problem of retrieving tethered satellites has seen a tremendous amount of research in recent years and many control strategies have been devised. Pines et al. [49] used sliding mode and operator-in-the-loop control, while Fujii and Ishijima , and Vadali and Kim [25] used a Lyapunov-based approach to insure stability.

Given the complexity of the problem of tether retrieval, many studies often use a simple model that assumes the tether is massless and rigid. The equations of motion for a three-dimensional massless, rigid tether in Keplerian orbit can be written as [38]:

$$\lambda'' - \lambda[\phi\prime^2 + cos^2\phi(1+\theta)^2 - 1 + 3cos^2\phi)cos^2\theta] = -\hat{T} \tag{97}$$

$$\theta'' + 2[(\lambda'/\lambda) - \phi' tan\phi](1+\theta') + 3cos\theta sin\theta = 0 \tag{98}$$

$$\phi'' + 2(\lambda'/\lambda)\phi' + cos\phi sin[(1+\theta')^2 + 3cos^2\theta] = \hat{F}/\lambda \tag{99}$$

where λ is the nondimensional length, θ is the in-plane swing angle, ϕ is the out-of-plane swing angle, $\hat{T}$ is the nondimensional tension and $\hat{F}$ is the out-of-plane control input. It is obvious from the equations that the in-plane and out-of-plane swing angles are coupled. This coupling may obscure the results when trying to evaluate controllers. If $\phi =$

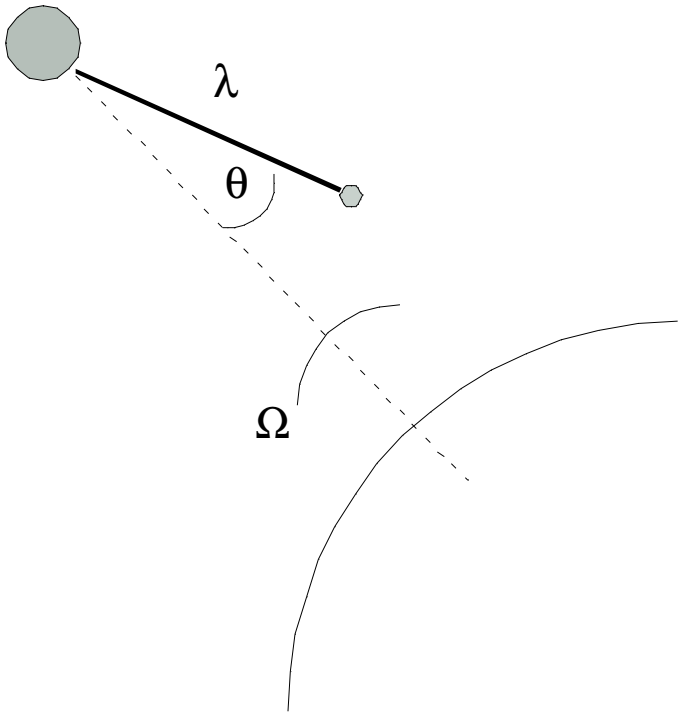

Figure 72: Nadir-Pointing Tethered Satellite System.

$phi' = \hat{F} = 0$ at the initial time, only the in-plane equations are needed to describe the motion of the tether. A simple, two-dimensional model that assumes a rigid, massless tether system in circular orbit is [38]:

$$\lambda'' - \lambda(1+\theta')^2 + 3\lambda cos^2(\theta) = -\hat{T} \tag{100}$$

$$\theta'' + 2(\lambda'/\lambda)(1+\theta') + 3cos(\theta)sin(\theta) = 0 \tag{101}$$

with λ and θ as defined in Figure 72. While this model does not capture all of the complex dynamics of the tethered satellite system, it is extremely useful in controller design and evaluation, and will be used for the simulations in this chapter.

3.1 Command Shaping for Tethered Satellite Retrieval

Many previous researchers have developed feedback control architectures or pre-computed tether length profiles for the retrieval process. However, to date, no one has explored the benefits of combining command shaping with controller gain selection to reduce tether retrieval time. This section will investigate the efficacy of command shaping in conjunction

with two Lyapunov-based feedback controllers.

3.1.1 Tension Control

Given the nonlinearities in the tethered satellite system, and the fact that the retrieval process is inherently unstable, extreme care must be taken when designing a controller for this system. Vadali and Kim [75] developed a tension controller for the deployment and retrieval process based on the Lyapunov criteria for stability. For a desired final length λ_f, the in-plane control law is given by:

$$\hat{T} = 3\lambda + K_1(\lambda - \lambda_f) + 2K_2\theta'(1+\theta')/\lambda + K_3\lambda' \tag{102}$$

The controller design is not complete, however, until the values for the gains K_1, K_2 and K_3 are selected. In general, the major trade-off in choosing the controller gains is compromising between a fast retrieval time and maintaining the maximum swing angle at or below acceptable levels. The controller gains suggested by Vadali and Kim ($K_1 = 1, K_2 = 0, K_3 = 4$) were originally chosen to minimize the tether retrieval while keeping the in-plane swing angle below a toleration limit of 0.3 radians and preventing tether slackness. The 0.3 radian limit is used to ensure that the tether remains in a nadir-pointing orientation. The solid black line in Figure 73 shows the non-dimensional length profile for the retrieval process from $\lambda = 1$ to $\lambda_f = 0.01$ while the solid black line Figure 74 shows the corresponding in-plane swing angle.

The retrieval time can be reduced by changing the controller gains K_1, K_2 and K_3 in the control law (102). The dashed red line in Figure 73 shows the non-dimensional length profile for the retrieval process with the increased controller gains ($K_1 = 2$, $K_2 = 0$, $K_3 = 8$). Given the asymptotic approach to the desired final tether length, the tether's length after one orbit is used as a measure of tether retrieval time. For the case shown, the tether length after one orbit is reduced by 35%. Unfortunately, the gain increase also leads to an increase of the in-plane swing angle. The dashed red line in Figure 74 shows that the maximum in-plane swing angle is 0.5 radians with the increased controller gains. This greatly exceeds the 0.3 radian limit. The dashed red line in Figure 75 shows the non-dimensional tension for the Increased Gains case. The tension remains above zero. Additionally, the tension

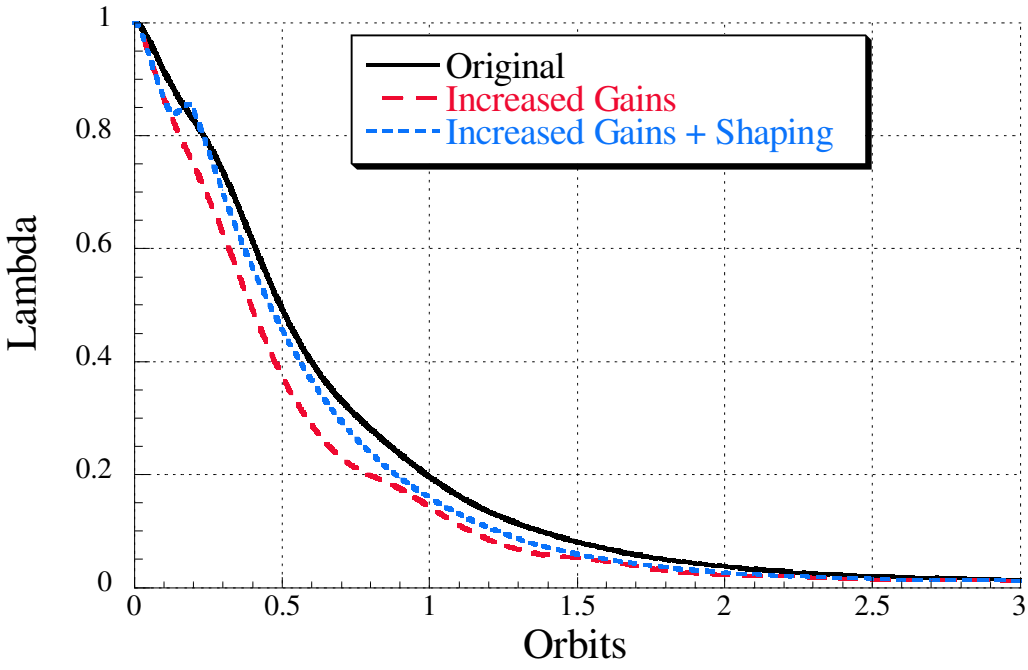

Figure 73: Tether Retrieval using Tension Controller.

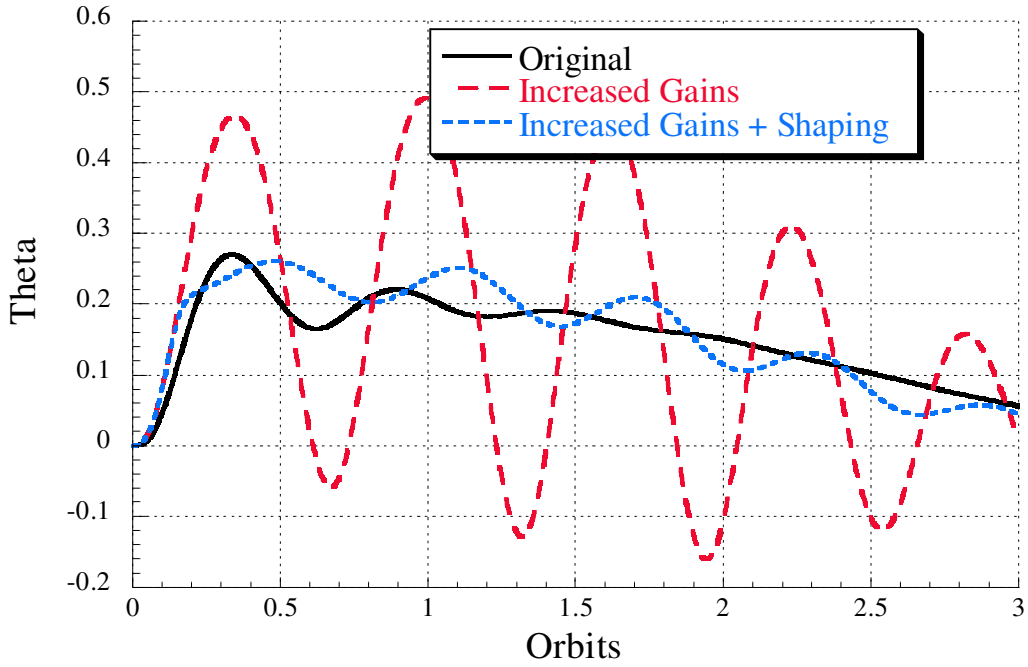

Figure 74: Swing Angle using Tension Controller.

is significantly higher than the original case. The upper limit on the tether tension is determined by the strength of the tether. It is assumed here that the tension values shown in these simulations will not exceed the limits placed on the tension by the tether material.

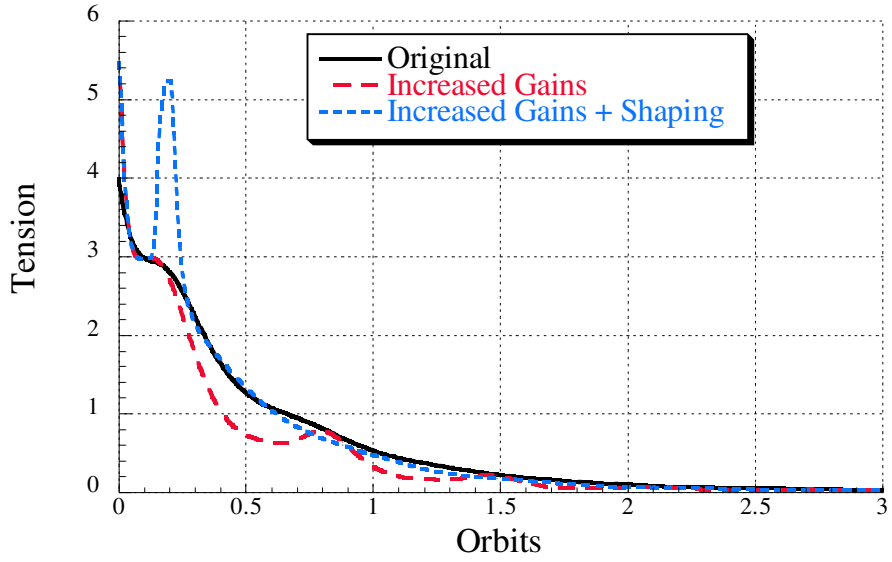

Figure 75: Tension using Tension Controller.

A command shaper was created to reduce the tether oscillation caused by the faster retrieval (increased gains). The unshaped input to the system is a step change in desired length. This step change was convolved with a UM-ZV input shaper [65] to create the new setpoints. Given the nonlinearities in the system, a closed-form solution for the impulse times and amplitudes is not possible. The command shapers for tethered satellites are created using numerical optimization routines. In this section, the retrieval length after 1 orbit is minimized while keeping the swing angle below 0.3 radians. The dotted blue line in Figure 73 shows the length profile for the increased gains "shaped" tether retrieval. The tether is approximately 20% shorter after one orbit when using increased gains and command shaping than the original case. Figure 76 shows the length of the Increased Gains and the Increased Gains + Shaping cases normalized by the Original case. The instantaneous percent reduction varies with time. However, the percent reduction after one orbit is representative of the average reduction for the entire retrieval.

The dotted blue line in Figure 74 shows that command shaping successfully reduced the swing angle to acceptable levels, a 50% decrease from the Increased Gains case. The shaper impulses were located at $t = 0.11$ and $t = 0.18$. That is, for $0 < t < 0.11$ and $t > 0.18$, the desired length was 0.01, while for $0.11 < t < 0.18$, the desired length was 1.0.

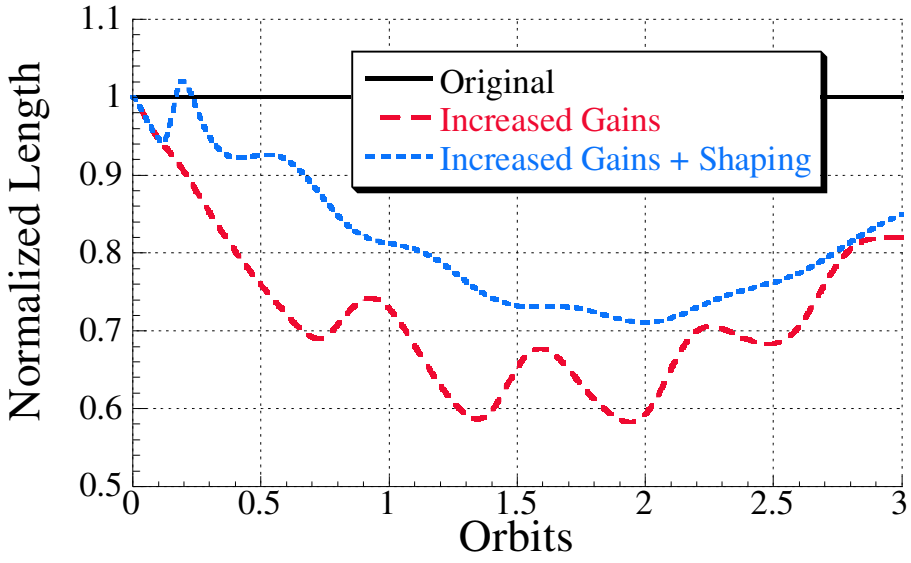

Figure 76: Normalized Tether Length During Retrieval using Tension Controller.

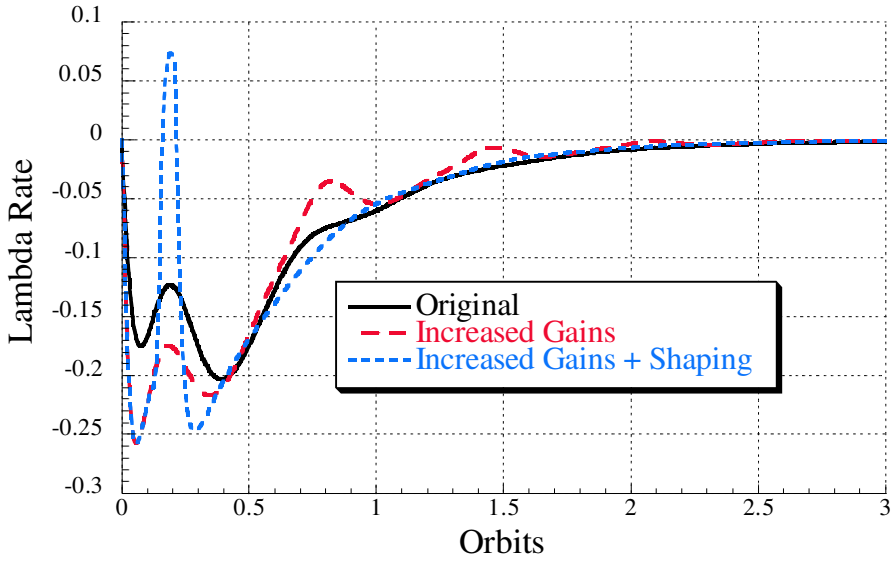

Figure 77: Tether Retrieval Rate using Tension Controller.

Figure 75 shows the non-dimensional tension for the retrieval process. The tension is shown to remain positive (i.e. no tether slackness) throughout the retrieval process. However, the Increased Gains and Increased Gains with Shaping cases increase the maximum tension by over 40%. The maximum tension the tether can safely support will depend on material and geometric properties of the tether. When the tension is expected to exceed the safe limit, the gains should be lowered.

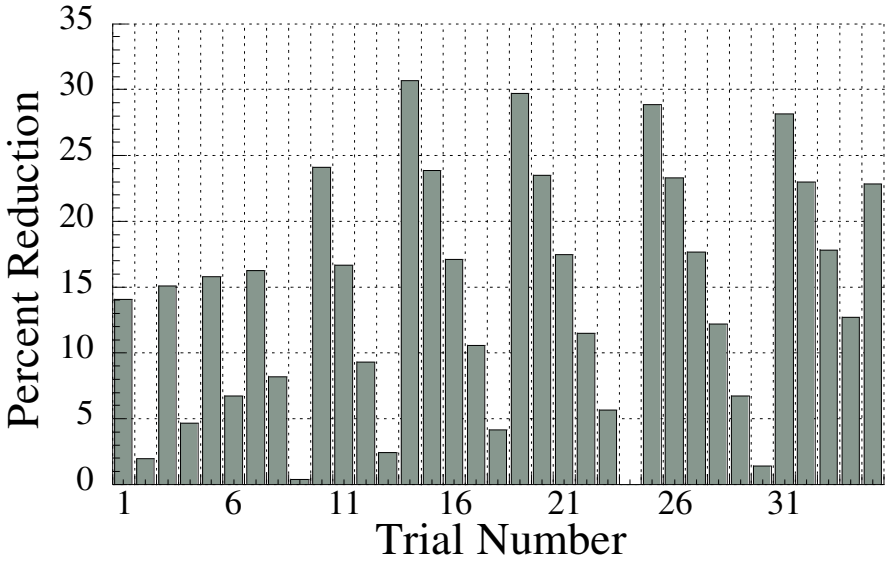

Figure 78: Tension Controller Retrieval Time Savings Summary

Not only will the maximum allowable tether tension be a limiting factor when implementing on a real system, so will the reel-in rate. Figure 77 shows the rate change of length for the three cases considered. The Increased Gains and Increased Gains with Shaping cases lead to an increase in the maximum reel-in rate. Additionally, the Increased Gains with Shaping case requires rapid changes in the retrieval rate. The feasibility of these requirements will ultimately depend on the mechanical design of the retrieval mechanism. Without knowing a detailed set of performance requirements and restrictions, it is impossible to determine an optimal gain set.

In the above results, the command shaper was designed for a specific gain set. The shaper switch times were chosen to minimize the tether length at 1 orbit while keeping the maximum swing angle below the tolerance limit. Due to the nonlinear nature of the equations of motion, the goal is not zero vibration but reduced swing angle. Figure 74 shows that command shaping reduces the maximum swing angle of the "Increased Gains" case by 50%. A different choice of gains would possibly lead to a vastly different response and require a different command shaper whose retrieval time and swing angle reduction characteristics may be different. A different gain set may be required to satisfy constraints on maximum tether tension or tether retrieval rate.

Table 3: Tension Controller Swing Angle Reduction and Retrieval Time Savings Summary.

K_1	K_3	%Swing Angle Reduction (Hi vs Hi + Shaping)	%Retrieval Time Reduction (Original vs Hi + Shaping)
3.5	9.3	72.6	44.6
2.7	8.5	55.0	21.1
2	7.2	42.2	0.1
2.2	7.5	43.3	9.0
Averages		53.3	18.7

In order to fully minimize the retrieval time, both the gain set and the command shaper should be designed together. However, the shaper can be designed independent of the gain set and still lead to significant retrieval time savings. Figure 78 shows the percent reduction in retrieval time for 35 different feedback controller gain sets. (Note: In all cases K_2 was set to zero.) For each set of gains, a command shaper was designed to minimize tether retrieval time. Table 3 shows the quantification of the swing angle reduction and retrieval time reduction for four sample gain sets. On average, adding command shaping reduces the maximum swing angle relative to the Increased Gains case by just over 48% with a standard deviation of 0.09 and results in 16% shorter tether lengths after 1 orbit with a standard deviation of 0.08 relative to the Original Gains case.

3.1.2 Reel-in-rate Control

In addition to the tension controller, Vadali and Kim [75] also developed a reel-in-rate controller for the deployment and retrieval process based on the Lyapunov criteria for stability. For a desired final length λ_f, the control law is given by:

$$\lambda' = K_1(\lambda - \lambda_f) + K_2\theta'(1 + \theta')/\lambda \tag{103}$$

Similar to the tension controller, once the overall form of the reel-in-rate controller is specified, the controller gains must be specified. The solid black line in Figure 79 shows the length profile for the reel-in-rate controller using the Original gains and the swing angle is shown in Figure 80. The gains chosen here attempt to minimize tether retrieval time while keeping the swing angle within tolerable limits ($K_1 = 0.25$, $K_2 = 0.01$). Figure 80 shows

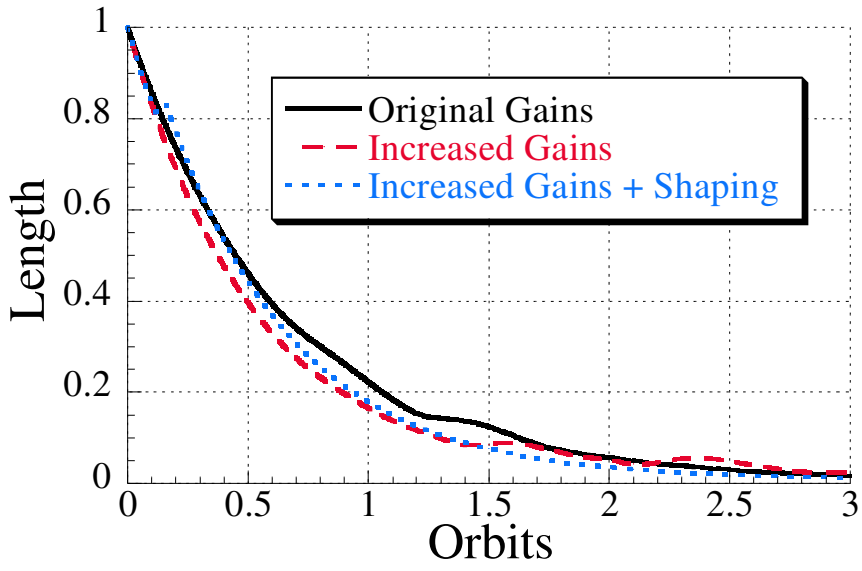

Figure 79: Tether Retrieval using Reel-in-rate Controller.

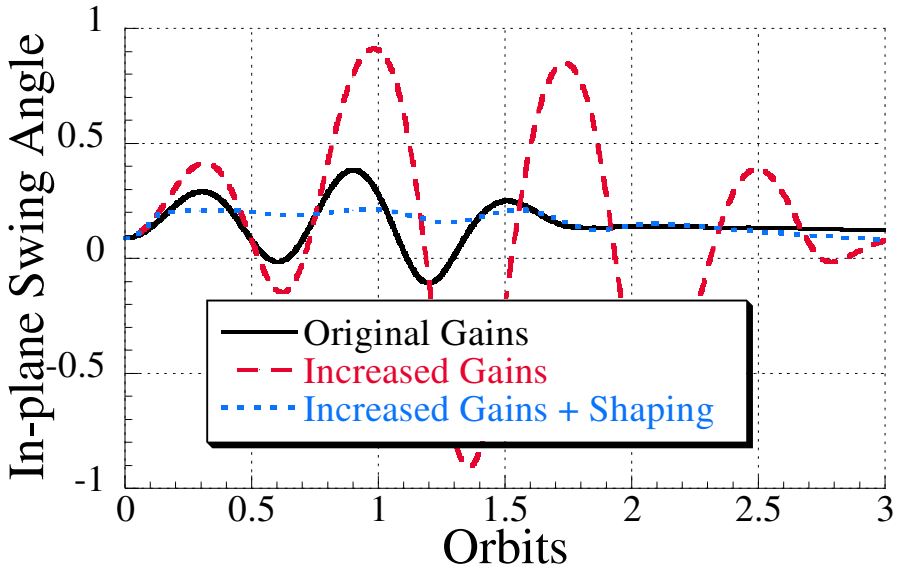

Figure 80: Swing Angle using Reel-in-Rate Controller.

that the maximum swing angle is 0.38 radians.

The retrieval time can be reduced by increasing the controller gains K_1 and K_2 in (103). The dashed red line in Figure 79 shows the non-dimensional length profile for the retrieval process with increased controller gains ($K_1 = 0.5$, $K_2 = 0.001$). The tether length after one orbit is reduced by 25%. Unfortunately, the gain increase also leads to an increase in the in-plane swing angle. The dashed red line in Figure 80 shows that the maximum

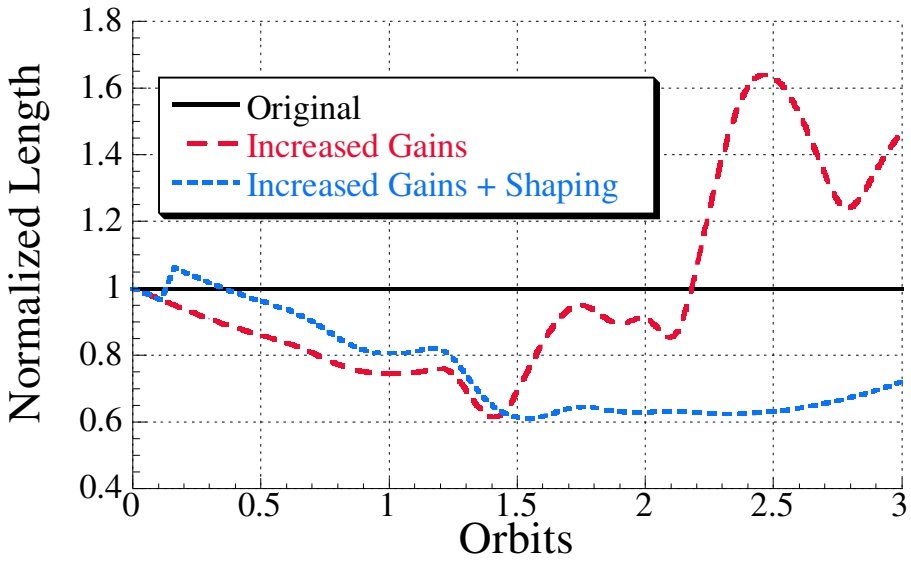

Figure 81: Normalized Tether Length During Retrieval using Reel-in Rate Controller.

in-plane swing angle is 0.9 radians with the increased controller gains. The dotted blue line in Figure 79 shows the length profile for the increased gains "shaped" tether retrieval. The shaper impulses were located at $t = 0.18$ and $t = 0.22$ orbits. For the case shown here, using increased gains and command shaping reduced the tether length after 1 orbit by 18%. Figure 81 shows the length of the Increased Gains and the Increased Gains + Shaping cases normalized by the Original case. The instantaneous percent deduction varies with time. However, the percent reduction after one orbit is representative of the average reduction for the entire retrieval.

The dotted blue line in Figure 80 shows that command shaping successfully reduced the swing angle to acceptable levels, reducing the swing angle of the Increased Gains case by 65%. Figure 82 shows the reel-in rate for the Original, Increased Gains and Increased Gains with Shaping case. Shorter retrieval times can be achieved by increasing the reel-in rate.

Command shapers were designed for 59 different gain sets. Figure 83 shows the results for 59 different feedback controller gains. For each set of gains, a command shaper was designed to minimize tether retrieval time. Table 4 shows the quantification of the swing angle reduction and retrieval time reduction for four sample gains sets. On average, using command shaping reduces the swing angle by 62% with a standard deviation of 0.07 and

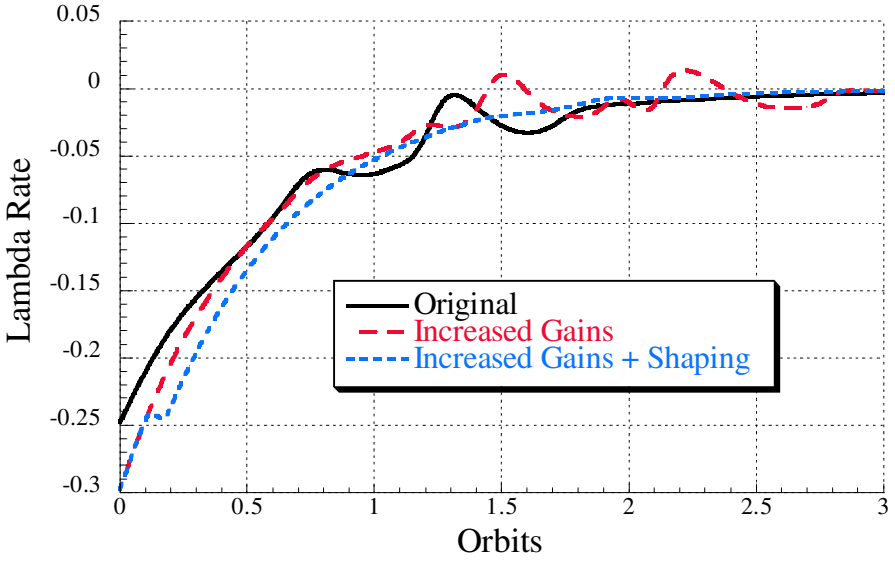

Figure 82: Reel-in Rate using Reel-in-Rate Controller.

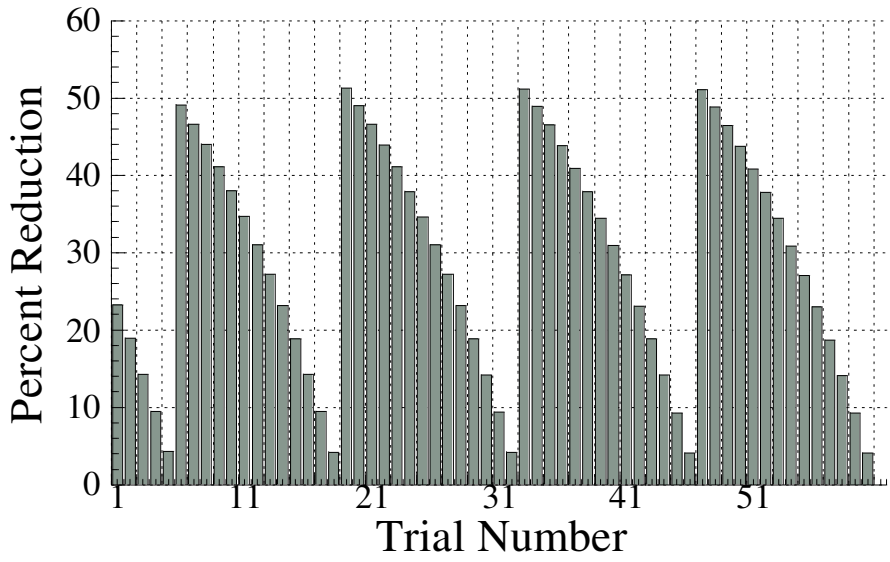

Figure 83: Reel-In Rate Controller Retrieval Time Savings Summary

reduces retrieval time by almost 29% with a standard deviation of 0.15.

3.2 Command Shaping for Partial Tether Retrieval

The results shown in the above section were for a full retrieval, from fully deployed to fully retrieved. However, many tether missions may require a partial retrieval, or retrieval in discrete intervals. This section addresses the effect the gain selection and command shaper

Table 4: Reel-in-rate Controller Swing Angle Reduction and Retrieval Time Savings Summary.

K_1	K_2	%Swing Angle Reduction (Hi vs Hi + Shaping)	%Retrieval Time Reduction (Original vs Hi + Shaping)
0.39	0.006	50.1	49.4
0.31	0.001	70.4	23.2
0.27	0.01	56.1	5.1
0.30	0.01	60.1	19.6
Averages		59.2	24.3

for a full retrieval will have on the case of a partial retrieval.

3.2.1 Tension Controller

Figure 84 shows the length profile for the Original gains, Increased Gains and the Increased Gains with Shaping cases for a retrieval from $\lambda = 1.0$ to $\lambda = 0.5$. For this partial retrieval, the length for the Increased Gains with Shaping case is actually longer than the Original gains case at 1 orbit. This is due to the delay of the UM-ZV shaper used to reduce the swing angle. While the retrieval time savings were not seen in the partial retrieval, the reduction in swing angle is maintained. Figure 85 shows the swing angle profile during the partial retrieval. Command shaping reduced the maximum swing angle of the increased gains case by over 60%. Here, the Increased Gains with Shaping's maximum swing is approximately 30% less than the Original case. Using shaping causes a slight delay in retrieval time, but it decreases swing angle.

In addition to a partial retrieval starting with the tether fully deployed, simulations were performed for a partial retrieval starting with a partially deployed tether. Figure 86 shows the length profile for the Original gains, Increased Gains and the Increased Gains with Shaping cases for a retrieval from $\lambda = 0.8$ to $\lambda = 0.2$. For this partial retrieval, again the length for the increased gains with shaping case is actually longer than the original gains case at 1 orbit. Figure 87 shows the swing angle profile during the partial retrieval. Command shaping reduced the maximum swing angle of the Increased Gains case by over 50%. Here, the Increased Gains with Shaping's maximum swing is approximately 30% less than the original case. The retrieval time savings obtained using a command shaper designed for a

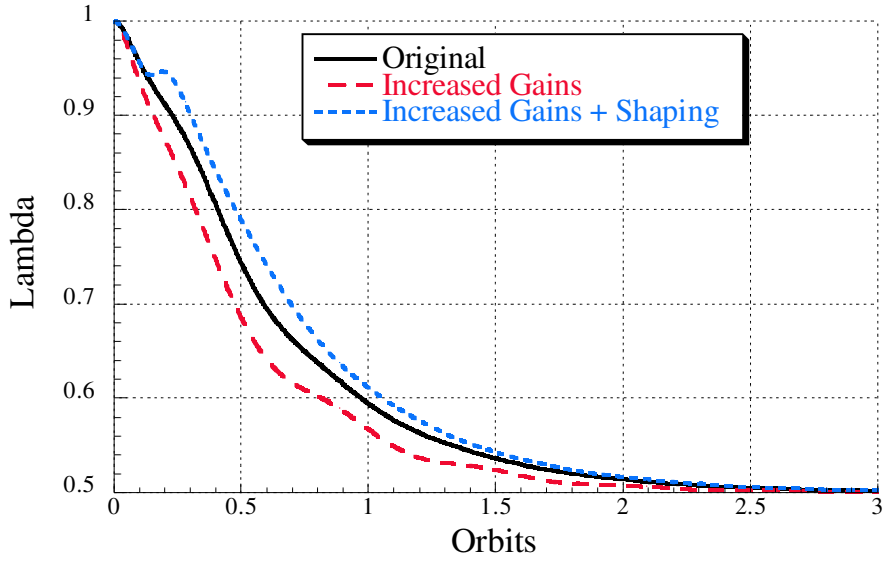

Figure 84: Length Profile of Retrieval from $\lambda = 1.0$ to $\lambda = 0.5$ using Tension Controller.

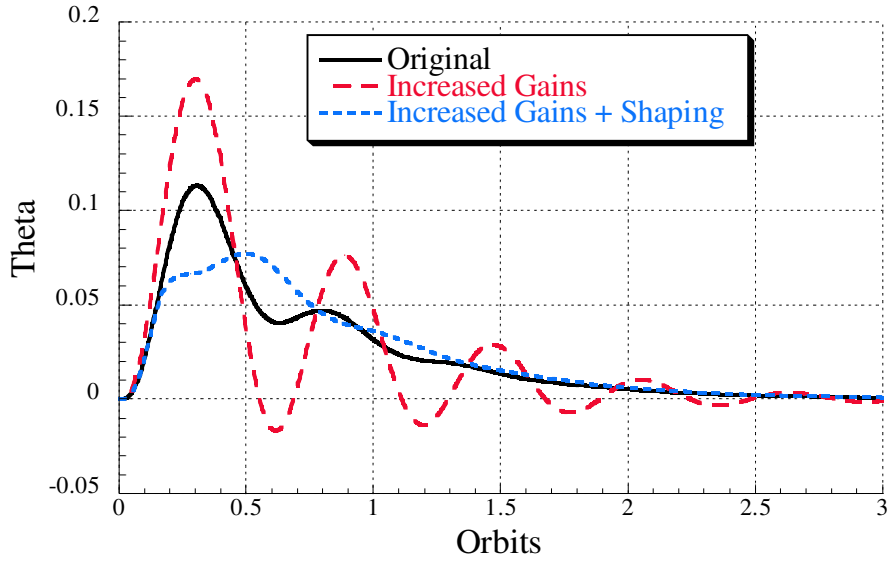

Figure 85: Swing Angle of Retrieval from $\lambda = 1.0$ to $\lambda = 0.5$ using Tension Controller.

full retrieval do not necessarily carry over to partial retrievals, but the reductions in swing angle do.

3.2.2 Reel-in Rate Controller

Figure 88 shows the length profile for the original gains, increased gains and the increased gains with shaping cases for a retrieval from $\lambda = 1.0$ to $\lambda = 0.5$. Even for this partial

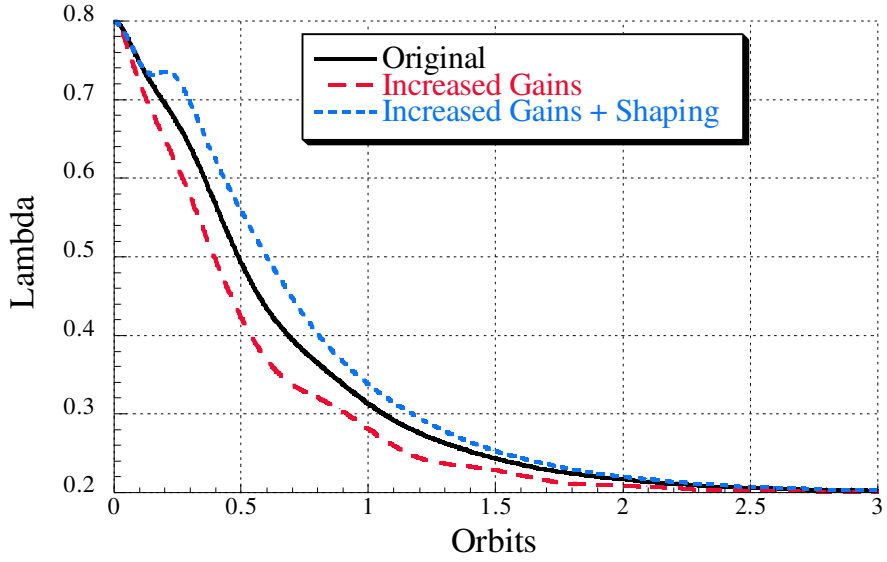

Figure 86: Length Profile of Retrieval from $\lambda = 0.8$ to $\lambda = 0.2$ using Tension Controller.

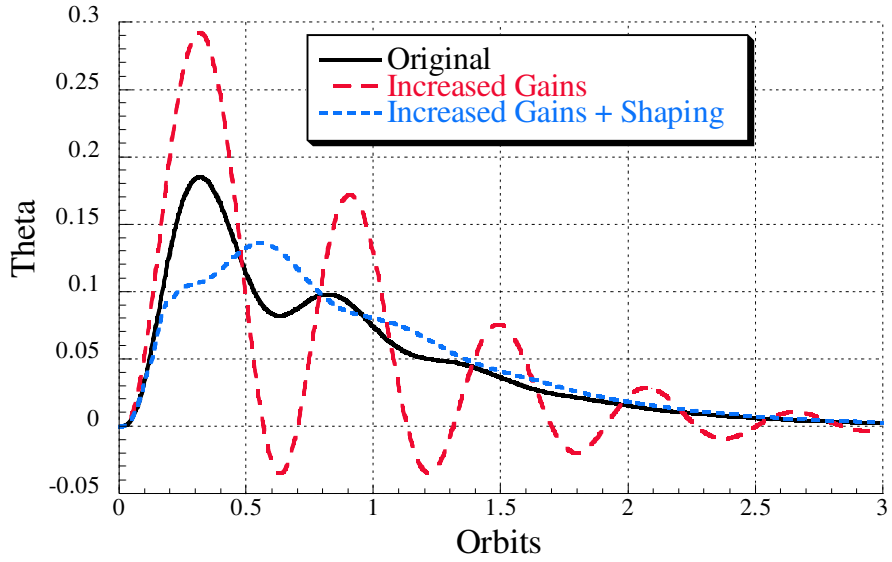

Figure 87: Swing Angle of Retrieval from $\lambda = 0.8$ to $\lambda = 0.2$ using Tension Controller.

retrieval, the length for the increased gains with shaping case has a shorter retrieval time than that of the original gains case at 1 orbit. Figure 89 shows the swing angle profile during the partial retrieval. Here, both the increased gains and the increased gains with shaping cases have maximum swing angles greater than that of the original profile. However, none of the cases exceed the tolerable limit.

In addition to a partial retrieval starting with the tether fully deployed, simulations

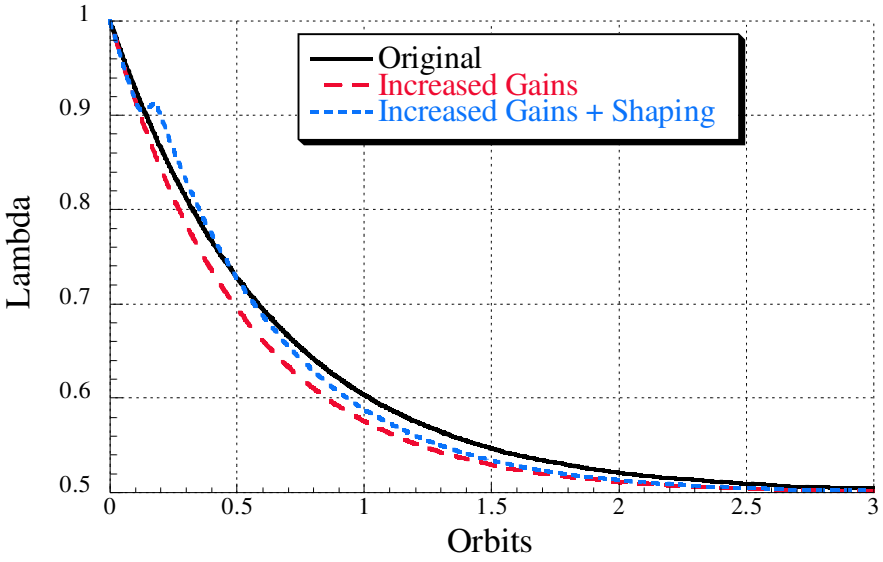

Figure 88: Length Profile of Retrieval from $\lambda = 1.0$ to $\lambda = 0.5$ using Reel-in Rate Controller.

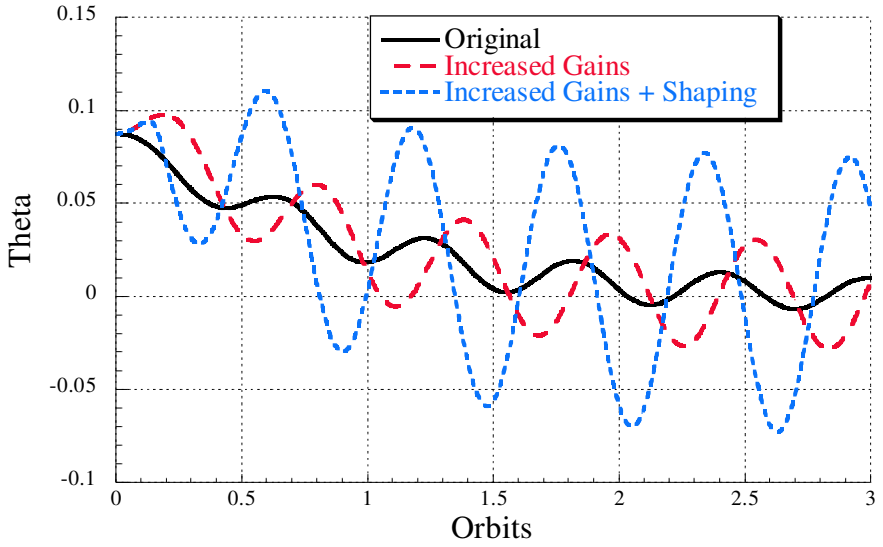

Figure 89: Swing Angle of Retrieval from $\lambda = 1.0$ to $\lambda = 0.5$ using Reel-in Rate Controller.

were performed for a partial retrieval starting with a partially deployed tether. Figure 90 shows the length profile for the original gains, increased gains and the increased gains with shaping cases for a retrieval from $\lambda = 0.8$ to $\lambda = 0.2$. For this partial retrieval, again the length for the increased gains with shaping case has a shorter length than the original gains case at 1 orbit. Figure 91 shows the swing angle profile during the partial retrieval. Here, the increased gains with shaping's maximum swing is approximately 15% less than

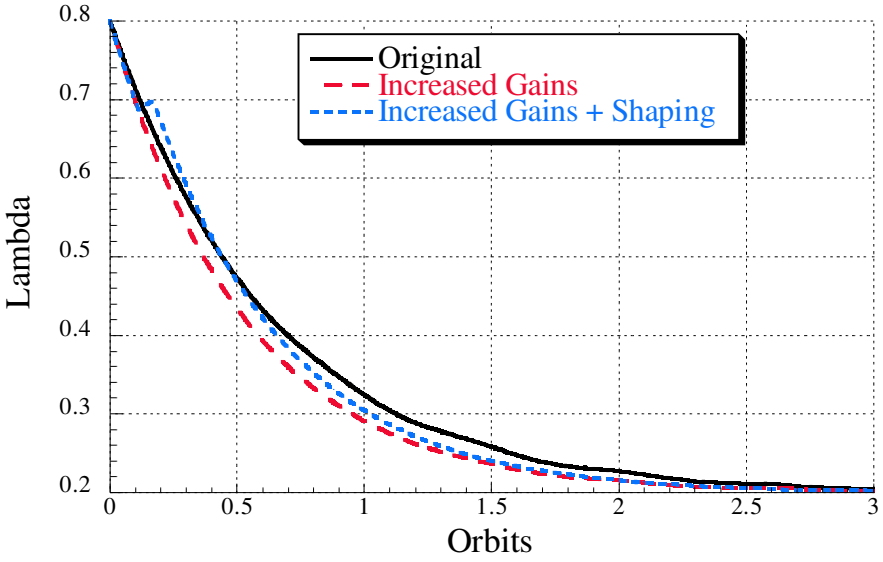

Figure 90: Length Profile of Retrieval from $\lambda = 0.8$ to $\lambda = 0.2$ using Reel-in Rate Controller.

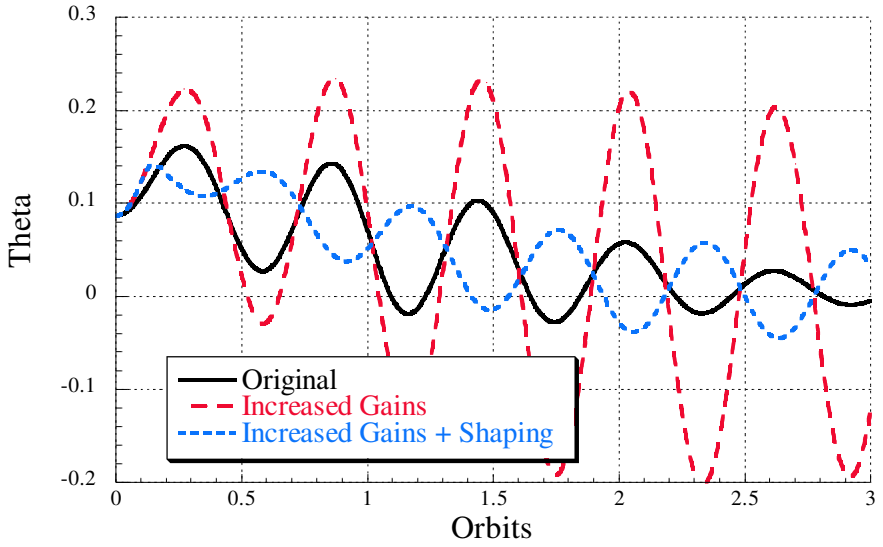

Figure 91: Swing Angle of Retrieval from $\lambda = 0.8$ to $\lambda = 0.2$ using Reel-in Rate Controller.

the original case. Command shaping reduced the maximum swing angle of the increased gains case by over 40%. For the Reel-in-Rate controller, the retrieval time saving obtained using a command shaper for full retrieval also translate into retrieval time savings for partial retrievals.

3.3 Effect of initial conditions on tether retrieval

There are many factors that can affect the swing angle during tether retrieval. The previous sections investigated the effect the controller gains, the command shaper and the retrieval distance has on tether retrieval dynamics. In addition to these factors, the swing angle at the beginning of the retrieval process has a great effect on the swing angle profile. This section will investigate the effect the initial swing angle has on the maximum swing angle attained during retrieval and outline command shaping techniques to compensate for the initial conditions.

3.3.1 Command Shaping for initial conditions

3.3.1.1 Tension Controller

In the Tension controller section, the retrieval was simulated for an initial swing angle of zero radians. Figure 92 shows the effect non-zero initial swing angles have on the maximum angle attained during the retrieval process using the Tension controller. Even a 5 degree (0.087 radians) initial condition can have dramatic effects on the performance of the Increased Gains controller. However, Figure 93 shows that the 5 degree initial condition has little effect on the tether length profile. These profiles are essentially similar to the zero initial condition profile. Figure 94 shows that the swing angle for both the increased gains and increased gains with input shaping has increased beyond acceptable levels.

An initial condition compensation input shaper (IC Shaper) was designed using an optimization that minimized retrieval time while keeping the swing angle acceptable. This length profile is shown as the dotted green line in Figure 95. Again, there is no significant difference between the IC Compensation shaper and the input shaper created assuming zero initial conditions. The differences between the two shapers is shown on the plot of the swing angle shown in Figure 96. The IC Compensation shaper successfully reduces the swing angle below the tolerance limit. It has a swing angle response that is comparable to the original case but has a shorter retrieval time. However, the IC Compensation Shaper will also suffer if the initial swing angle changes from the angle for which it was designed.

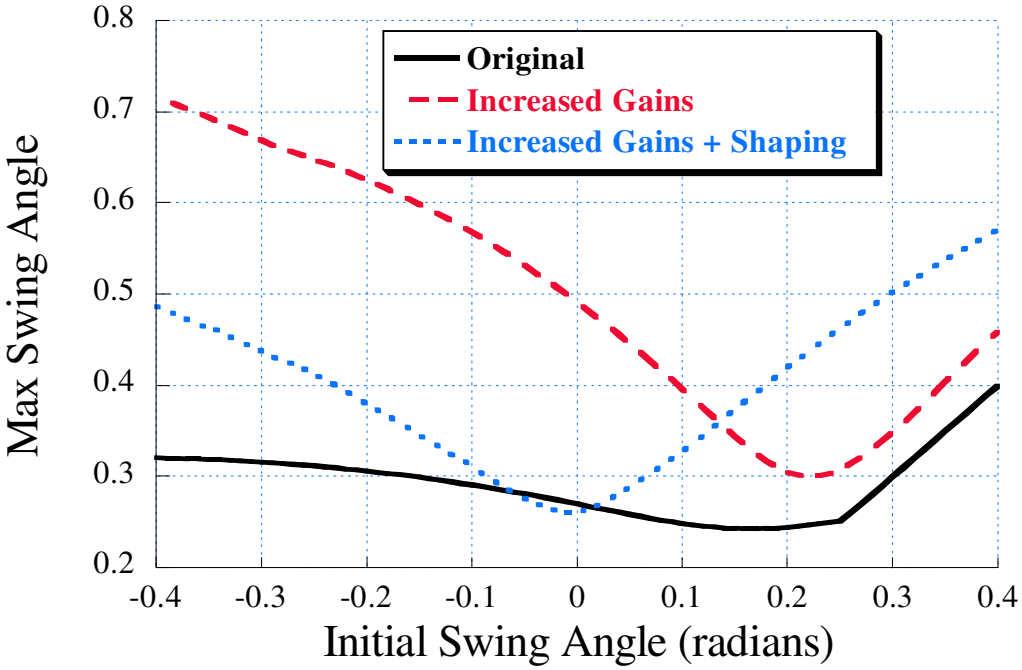

Figure 92: Effect of Initial Swing Angle using Tension Controller.

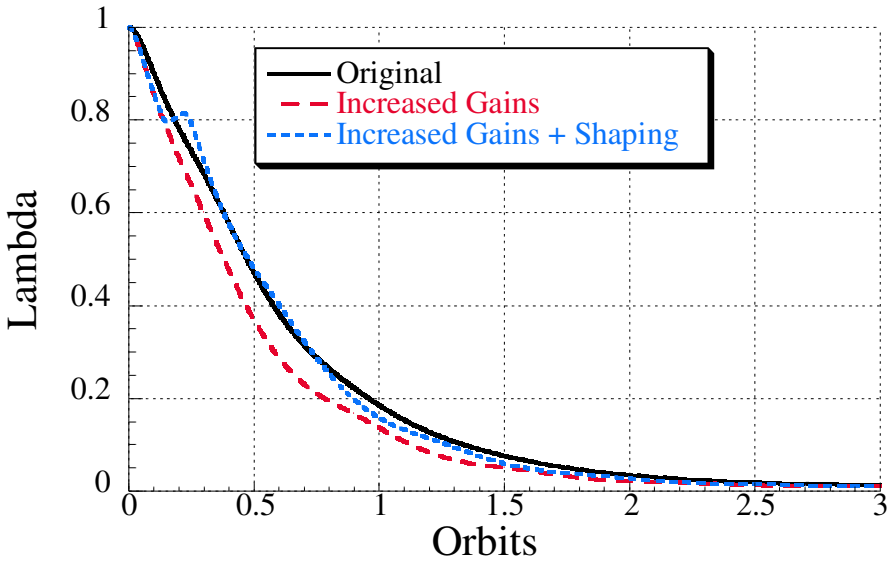

Figure 93: Length Profile with Initial Swing Angle using Tension Controller.

3.3.1.2 Reel-in-rate Controller

The effect the initial conditions have on the swing angle response is even more dramatic using the reel-in-rate controller. The results shown in Figures 79 and 80 were for an initial swing angle of 0.0873 radians (5 degrees). Figure 97 shows the maximum in-plane swing

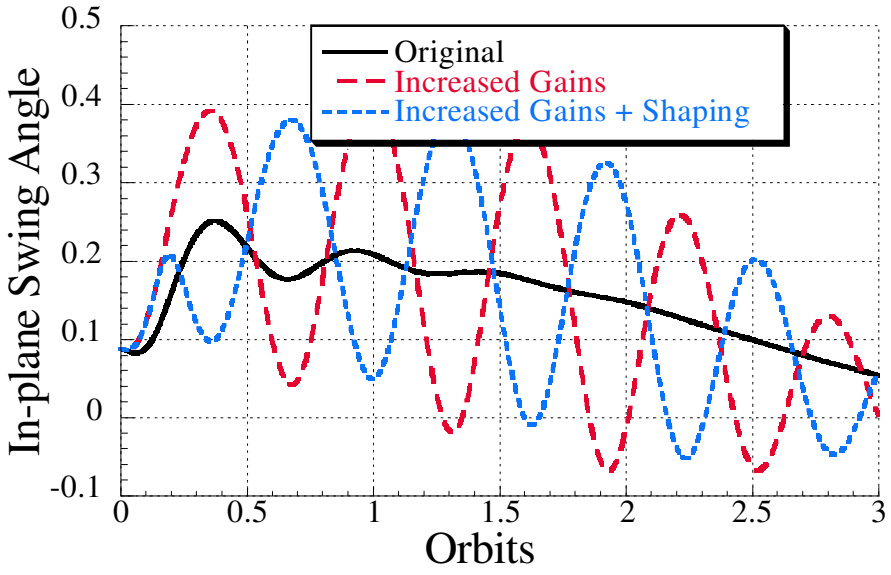

Figure 94: Length Profile with Initial Swing Angle using Tension Controller.

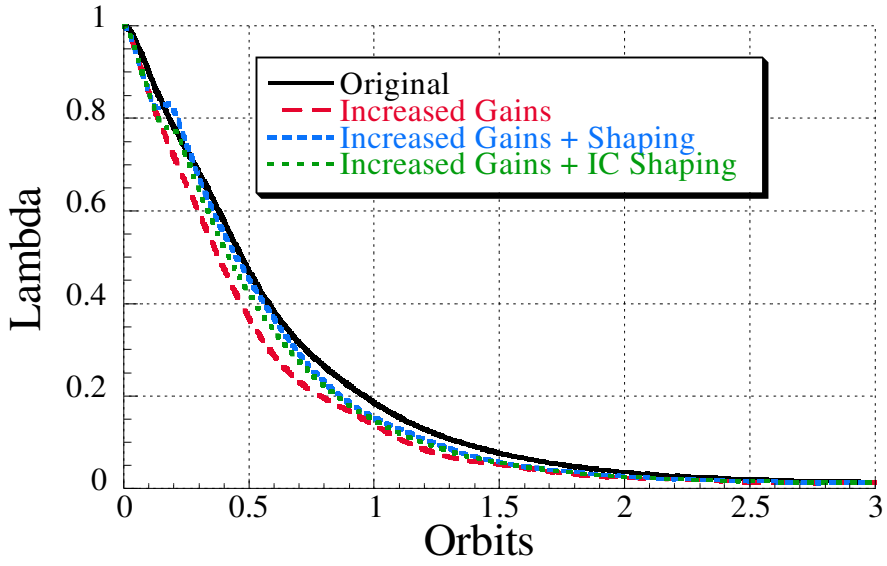

Figure 95: Length Profile with Initial Swing Angle using Tension Controller.

angle as a function of initial swing angle for the reel-in-rate controller. The original case works only for a small subset of initial swing angles. In fact, if the initial swing angle is zero, the original case would yield a maximum swing angle that exceeds the toleration limit. The reel-in-rate controller is highly dependent on the initial conditions. The previous section demonstrated the ability to create a shaper to reduce the swing angle for a specific initial condition, but that particular shaper would also be dependent on the initial conditions.

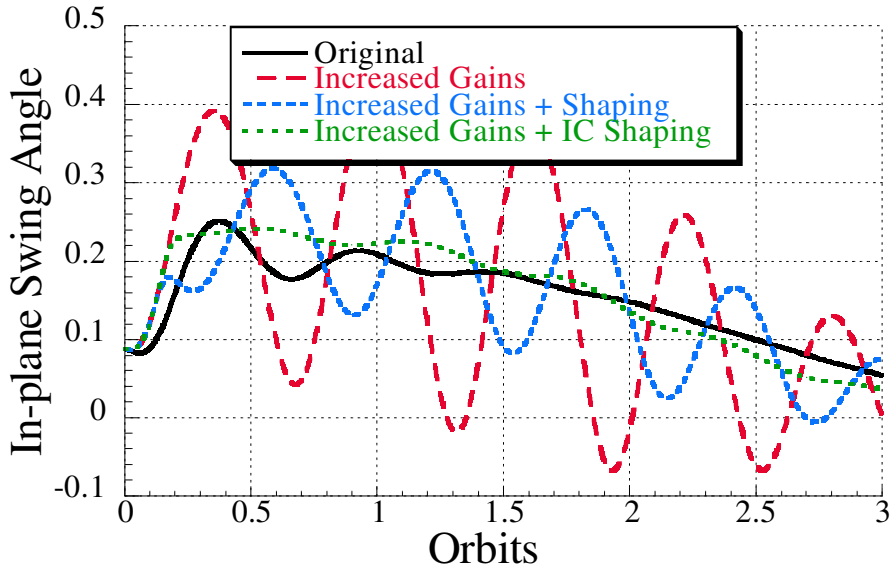

Figure 96: Length Profile with Initial Swing Angle using Tension Controller.

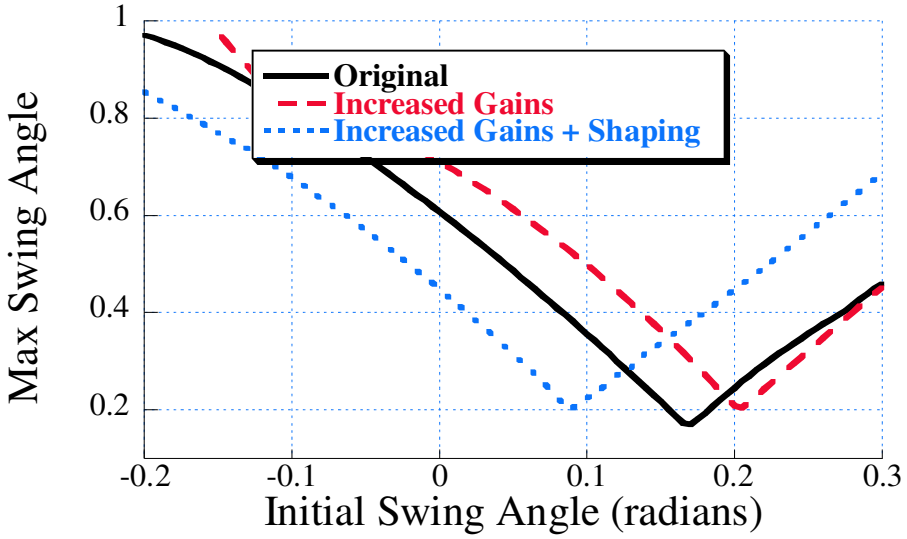

Figure 97: Effect of Initial Swing Angle using Reel-in-rate Controller.

These results motivate the development of command shapers for tether retrieval that are robust to initial swing angles.

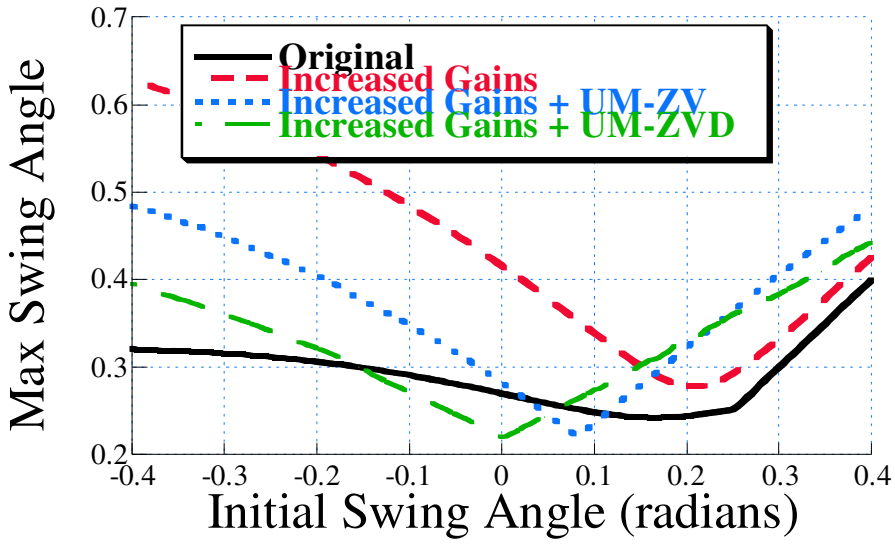

Figure 98: Length Profile with Initial Swing Angle using Tension Controller.

3.3.2 UM-ZVD Shapers for tether retrieval

3.3.2.1 Tension Controller

In an effort to produce a command shaper that is more robust to the effect of the initial conditions, a UM-ZVD shaper was designed for the tension controller. Figure 98 shows that this approach does lead to a significant improvement in robustness. The maximum swing angle is held below the tolerable limit for initial conditions up to 0.15 radians. Unfortunately, this increase in robustness comes with a steep price. Figure 99 shows the length of the tether after 1 orbit. The gain in robustness achieved by using the UM-ZVD shaper is outweighed by the retrieval time penalty because it takes longer to retrieve than the Original Gains case.

3.3.2.2 Reel-in-rate Controller

A UM-ZVD shaper designed for an initial condition of 0.087 for the Reel-in-rate controller produces only a minimal increase in robustness, as shown in Figure 100. Unfortunately, this approach again comes with a substantial price. Figure 101 shows that using a UM-ZVD Shaper results in a retrieval time that is slower than the original case. Given that traditional "robust" shapers are ineffective, a novel approach to producing command shapers that are

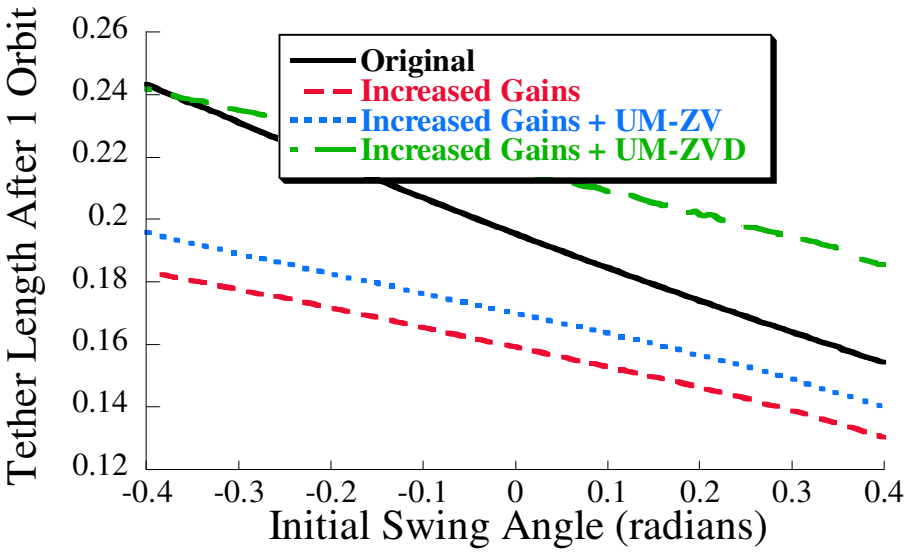

Figure 99: Tether Retrieval Time using Tension Controller.

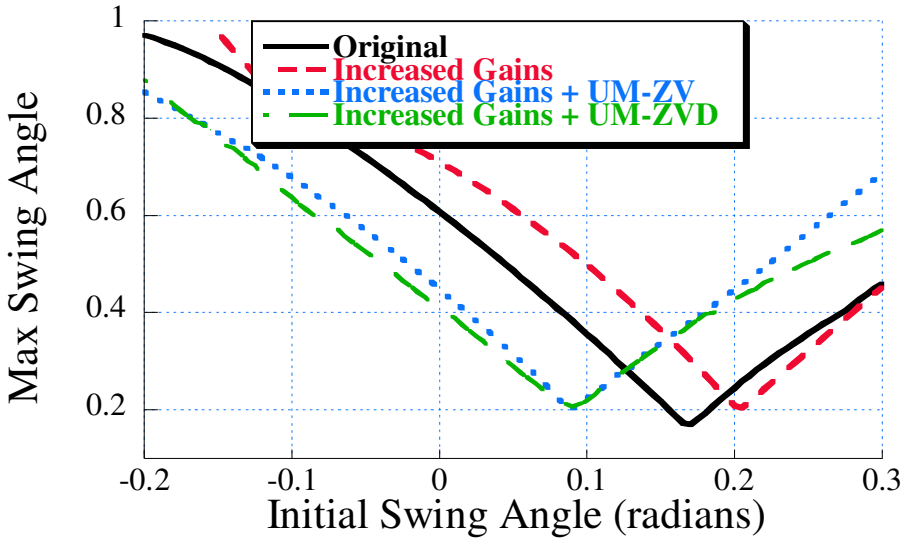

Figure 100: Length Profile with Initial Swing Angle using Reel-in-rate Controller.

robust to initial conditions is described in the following section.

3.3.3 Multi-UM-ZV Shapers for tether retrieval

3.3.3.1 Tension Controller

In an effort to replicate the robustness of the UM-ZVD, but retain the short retrieval times achieved with the UM-ZV shaper, three UM-ZV shapers designed for different initial

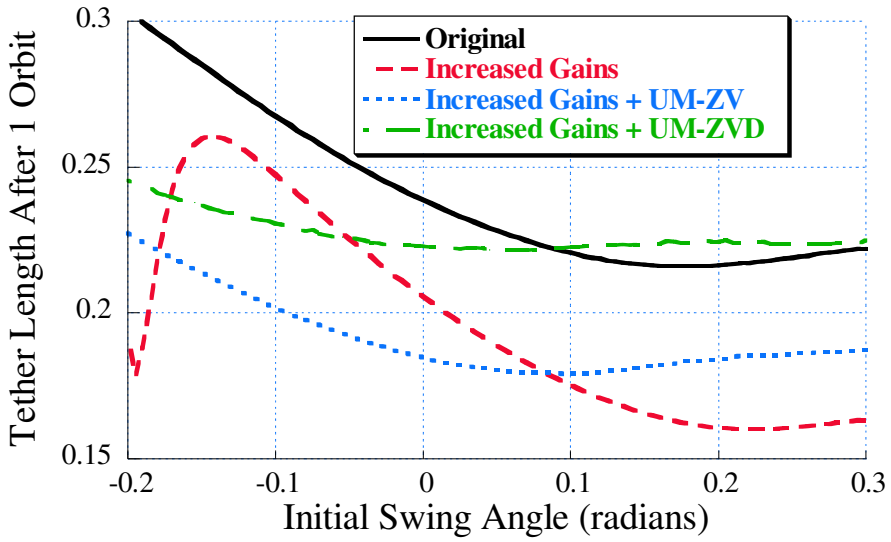

Figure 101: Tether Retrieval Time using Reel-in-rate Controller.

conditions were combined into a switching-type shaper. That is, each shaper was assigned to suppress a range of initial conditions. A suppression range of +/- 0.3 radians is shown in Figure 102. Given an initial swing angle, the retrieval process uses the shaper developed for that particular range of swing angles. This eliminates the need to design a shaper for each specific initial condition and reduces the dependence on a precise measurement of the initial condition. Figure 103 shows that the retrieval time for the Multi-UM-ZV is shorter than the original case for a wide range of initial conditions.

3.3.3.2 Reel-in-rate Controller

A Multi-UM-ZV shaper was also designed for the reel-in rate controller. The Multi-UM-ZV shaper was also designed for a range of initial conditions from -0.05 to 0.2 radians, as shown in Figure 104. Only three specific initial conditions were used in the Multi-UM-ZV shaper shown. In addition to keeping the maximum swing angle below the toleration limit in the suppression range, the Multi-UM-ZV shaper also reduces tether retrieval time, as shown in Figure 105. A wider suppression range can be easily produced by including more UM-ZV shapers. Figure 106 shows the results of a 5-hump-UM-ZV shaper designed for the reel-in rate controller. This shaper expands the suppression range from -0.2 to 0.2 radians.

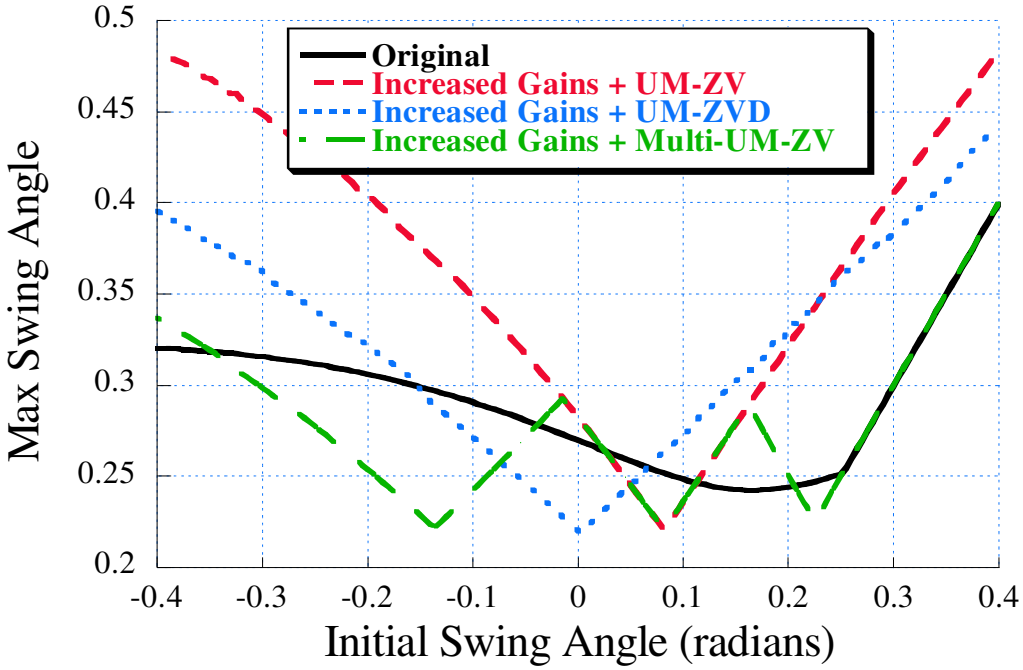

Figure 102: Maximum Swing Angle During Retrieval Using Tension Controller.

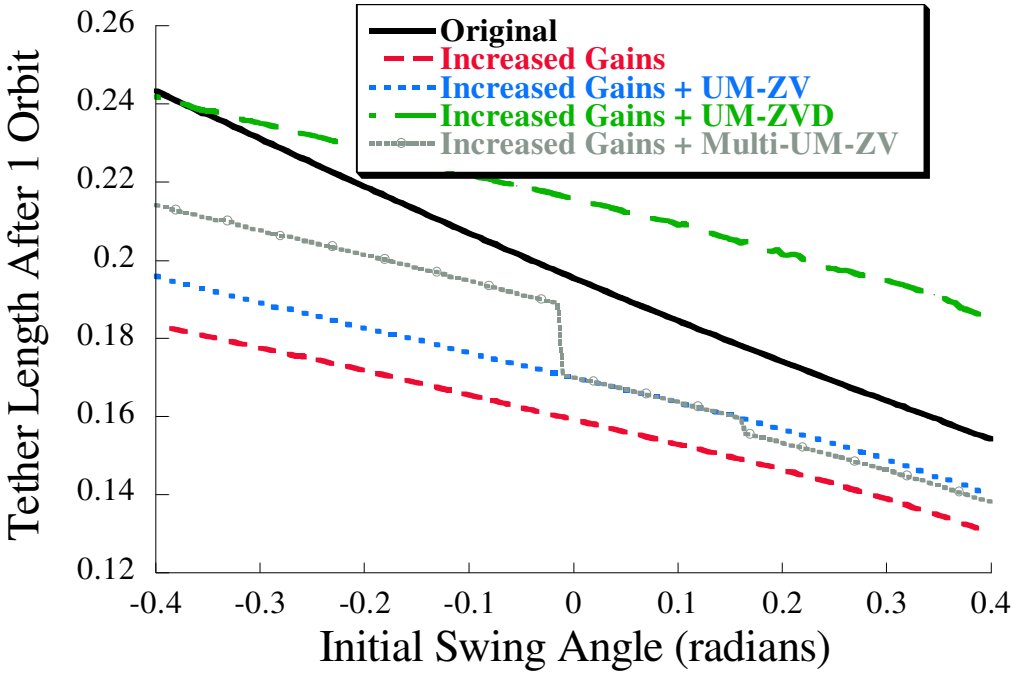

Figure 103: Tether Retrieval Time using Tension Controller.

3.4 Summary

In this chapter command shaping and controller feedback gain selection were combined to reduce tether retrieval time and control the tether swing angle. The major contributions of

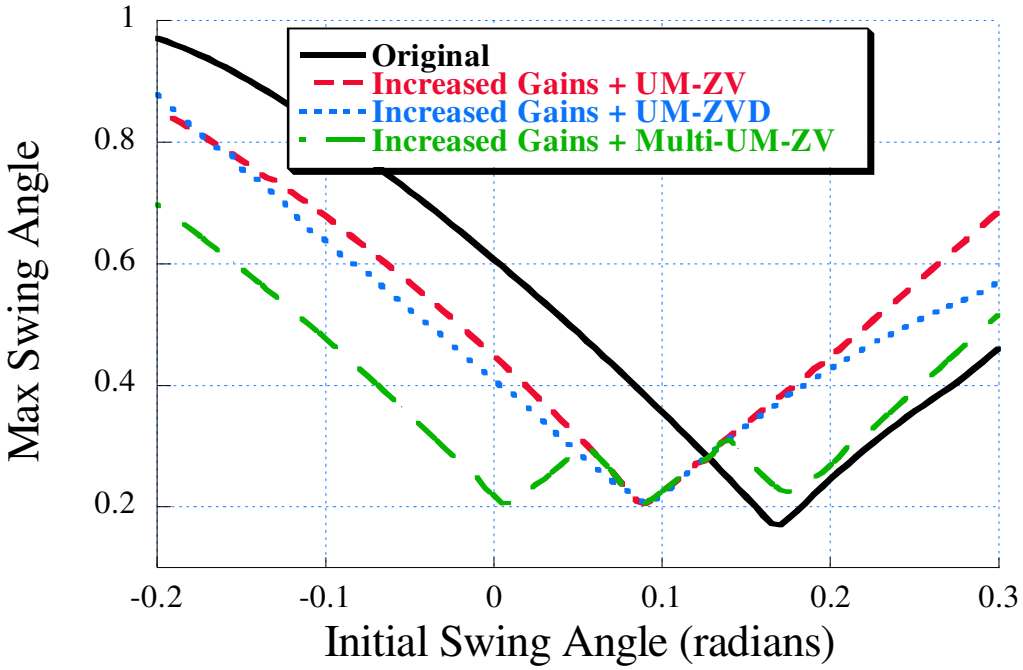

Figure 104: Maximum Swing Angle During Retrieval Using Reel-in-rate Controller.

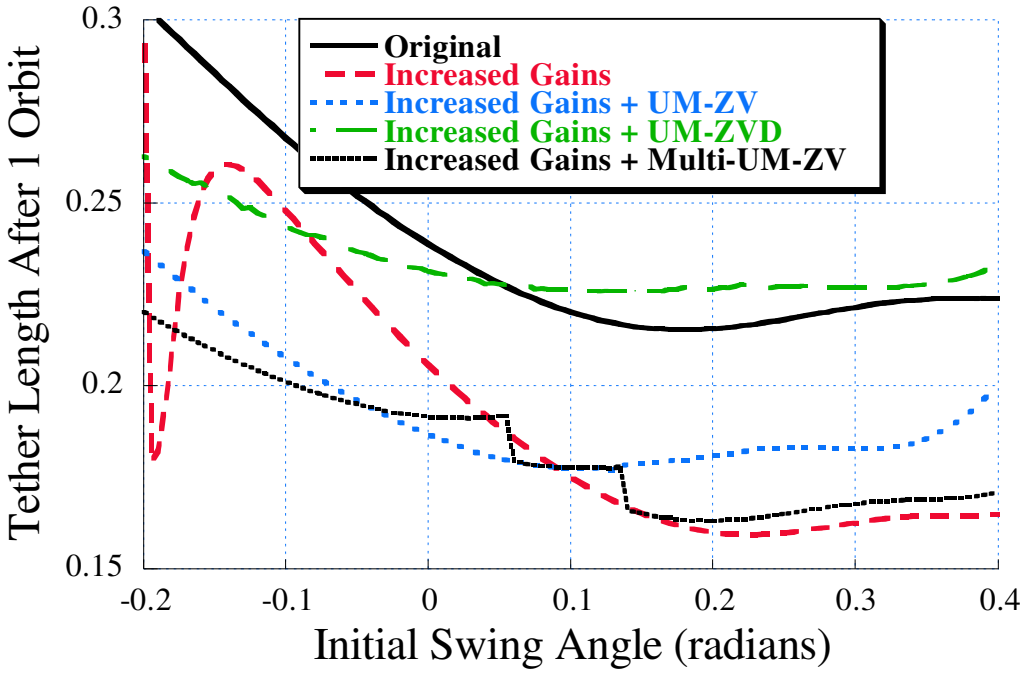

Figure 105: Tether Retrieval Time using Reel-in-rate Controller.

this chapter are:

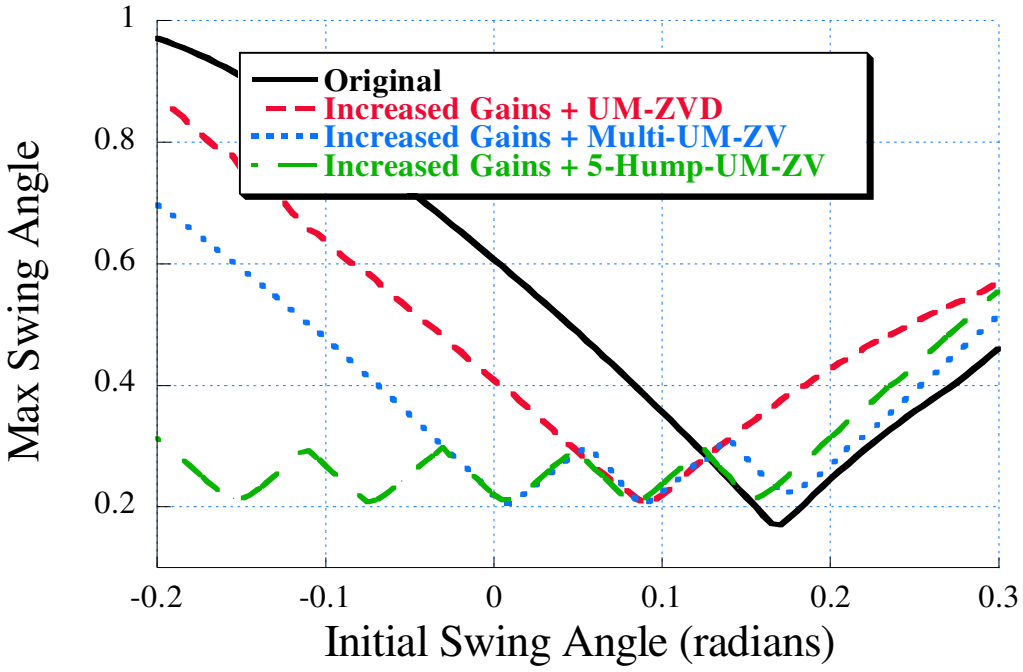

Figure 106: Maximum Swing Angle given Initial Swing Angle using Reel-in-rate Controller.

- A technique for combining command shaping and controller feedback gain selection to reduce tether retrieval time and swing angle.
- Verification that command shaping developed for full retrieval can be used for partial tether retrieval.
- A procedure for creating a command shaping scheme developed to reduce the effect of initial swing angle.

CHAPTER IV

TETHERED SATELLITE RETRIEVAL USING THREE DIMENSIONAL MODEL

The previous chapter detailed the benefits of using command generation and feedback controller gain adjustment to reduce tether retrieval time using a 2D model. This was done in an attempt to isolate the in-plane swing angle and focus on it alone. In the 3D model, there is coupling between the in-plane and out-of plane swing angles. This chapter will investigate the effect the increased gains and shaping has on the out-of-plane swing angle.

4.1 Out-of plane motion

4.1.1 Tension Controller

The equations of motion for a three-dimensional massless, rigid tether in Keplerian orbit, presented in the previous chapter, are repeated here:

$$\lambda'' - \lambda[\phi\prime^2 + cos^2\phi(1+\theta)^2 - 1 + 3cos^2\phi)cos^2\theta] = -\hat{T} \tag{104}$$

$$\theta'' + 2[(\lambda'/\lambda) - \phi' tan\phi](1+\theta') + 3cos\theta sin\theta = 0 \tag{105}$$

$$\phi'' + 2(\lambda'/\lambda)\phi' + cos\phi sin[(1+\theta')^2 + 3cos^2\theta] = \hat{F}/\lambda \tag{106}$$

where λ is the nondimensional length, θ is the in-plane swing angle, ϕ is the out-of-plane swing angle, $\hat{T}$ is the nondimensional tension and $\hat{F}$ is the out-of-plane control input. Here it is assumed that the out-of-plane motion is actively controlled. In these simulations, the tension control law based on the coupled equations and out-of-plane controller presented in [75]

$$\hat{T} = 3\lambda + K_1(\lambda - \lambda_f) + 2K_2[\theta'(1+\theta')\cos\phi^2 + \phi'^2]/\lambda + K_3\lambda' \tag{107}$$

and

$$\hat{F} = -k_4\lambda\phi' \tag{108}$$

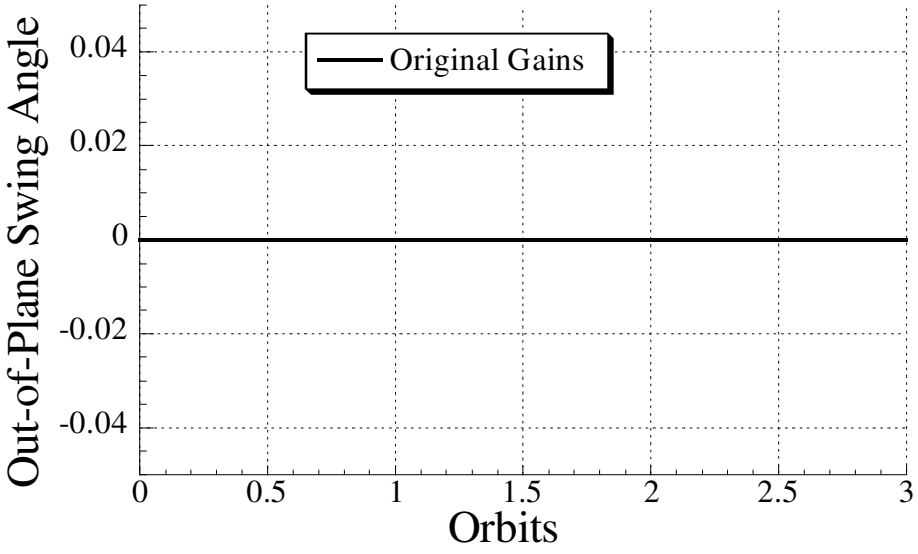

Figure 107: Out-of-plane Swing Angle using Original Gains.

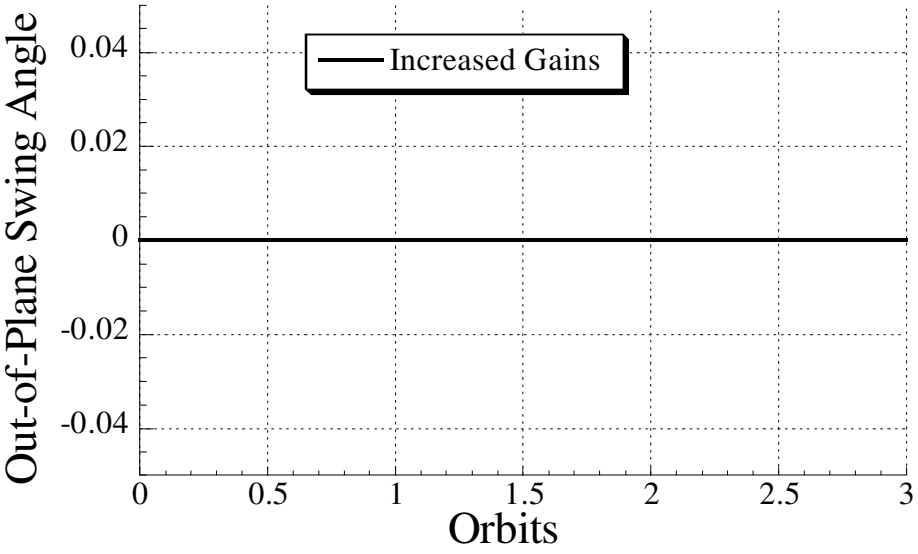

Figure 108: Out-of-plane Swing Angle using Increased Gains.

are used. For both the unshaped and shaped cases, $k_4 = 2$ will be used.

Figures 107 and 108 show the out-of-plane motion for initial conditions of $\theta = \dot{\theta} = \phi = \dot{\phi} = 0$. For this set of initial conditions, the out-of-plane motion is not excited, verifying the assumption made in the previous chapter. Even with the large in-plane swing angles achieved during retrieval using Increased Gains, as shown in Figure 74, the out-of-plane swing angle is not excited.

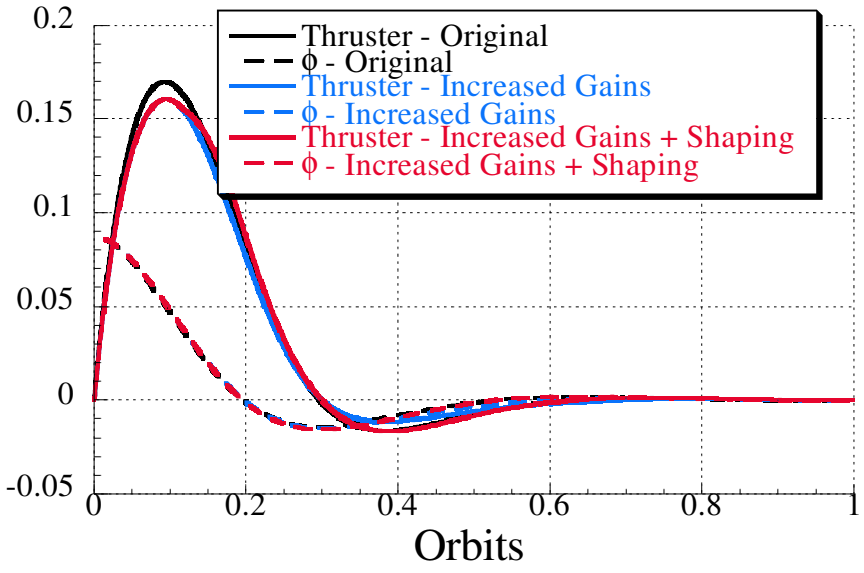

Figure 109: Out-of-plane Swing Angle and Thruster Profile: $\phi_{init} = 5$ degrees.

This is not the case when ϕ has non-zero initial conditions. Figure 109 shows the out-of-plane swing angle and thruster profile for a 5 degree initial condition in ϕ. Due to the out-of-plane controller, there is no difference in the maximum swing angle or the settling time. In fact, given the direct control of the out-of-plane thruster, the out-of plane swing angle is reduced in about a half an orbit. There are, however, small differences in the out-of-plane thruster profiles for the Original, Increased Gains and Increased Gains + Shaping cases. The Original case profile actually has the highest value, but it settles a small amount faster. These trends are repeated for a retrieval with $\phi_{init} = 10$ degrees as shown in Figure 110. Figure 111 shows the effect of $\theta_{init} = 5$ degrees on the out-of-plane motion. There is little difference between out-of-plane profiles for retrieval with and without a non-zero in-plane swing angle initial condition. Overall, the net actuator effort are equivalent for the three cases regardless of out-of-plane initial condition.

Figure 112 shows the in-plane swing angle when there is an initial condition of 5 degrees in the out-of-plane swing angle. There are no significant differences between the in-plane responses with and without the out-of-plane initial condition in the Original and Increased Gains responses and only the slightest difference in the Shaped response. In this case the neither the coupling nor the increased gains have a significant effect. Since the out-of-plane

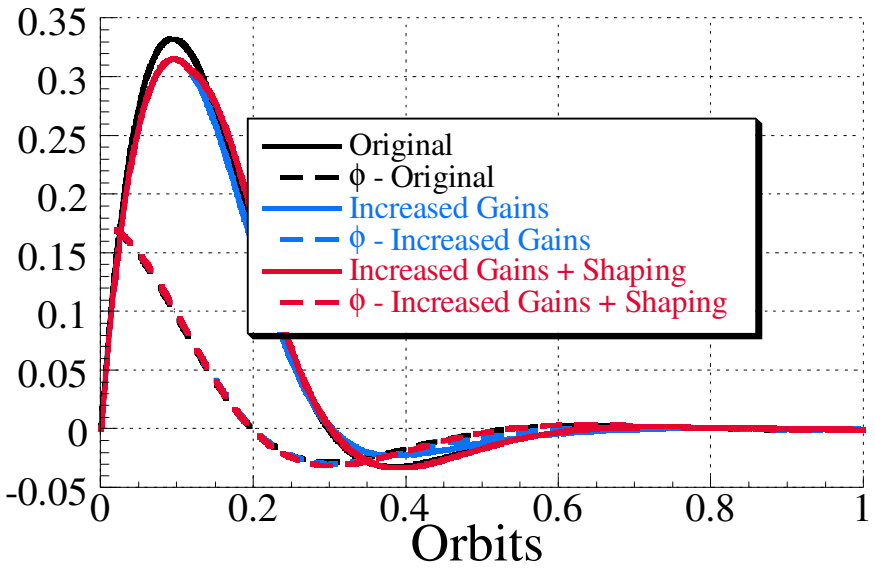

Figure 110: Out-of-plane Swing Angle and Thruster Profile: $\phi_{init} = 10$ degrees.

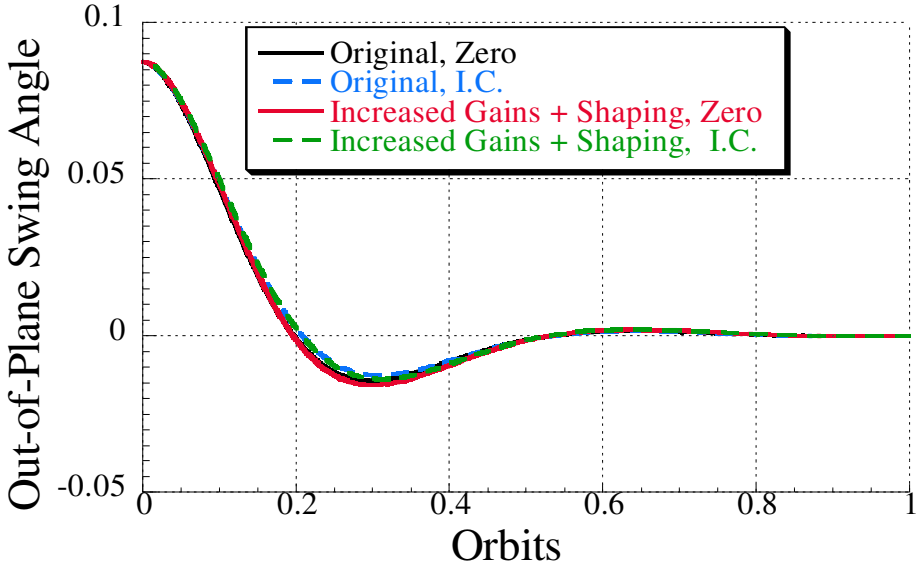

Figure 111: Comparisons Out-of-plane Swing Angle Profiles.

swing angle is actively controlled there is very little chance that the higher gains will lead to instability. The only possible negative effect, increased out-of-plane thruster usage, is minimal.

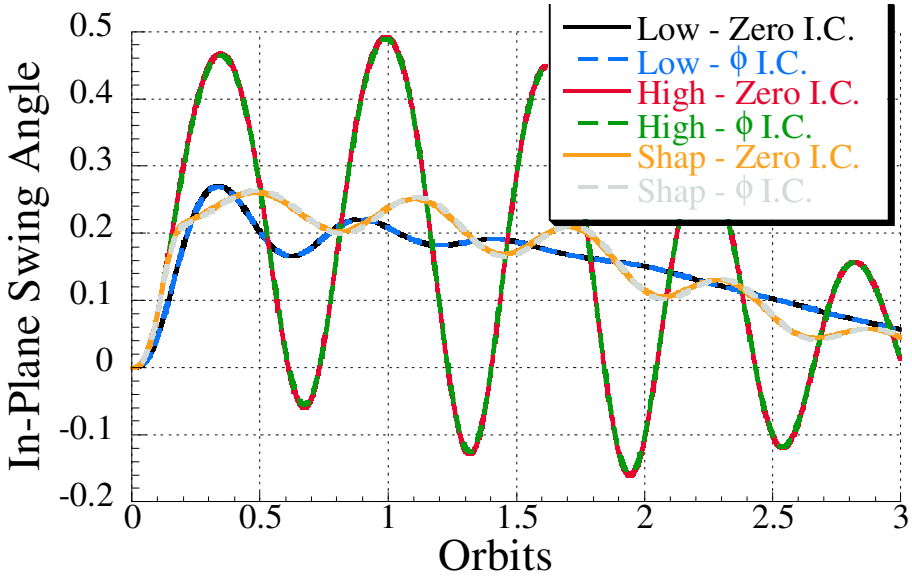

Figure 112: Effect of Out-of-Plane Swing Angle on In-Plane Swing Angle using Tension Controller.

4.1.2 Reel-in-rate Controller

The previous section examined the coupling between the in-plane and out-of-plane angles when controlled with a tension control law and an out-of-plane thruster. In this section, the effect the coupling has on the performance of the reel-in-rate controller, and the controller's effect on the coupling will be investigated.

Figure 113 shows the out-of-plane swing angle and thruster profile for a 5 degree initial condition in ϕ using the out-of-plane controller given in (108). In all cases, the out-of-plane angle settles in approximately 0.6 orbits. Increasing the gains does not adversely effect the out-of-plane seing angle or thruster profile. Again, the maximum control effort is slightly higher for the Original case while the Increased Gains + Shaping case requires 10% more net actuator effort.

Figure 114 shows the in-plane swing angle when there is an initial condition of 5 degrees in the out-of-plane swing angle. There are small differences between the in-plane responses with and without the out-of-plane initial condition in the Increased Gains and Increased Gains + Shaping responses. In this case the neither the coupling nor the increased gains have a significant effect. Since the out-of-plane swing angle is controlled there is very little

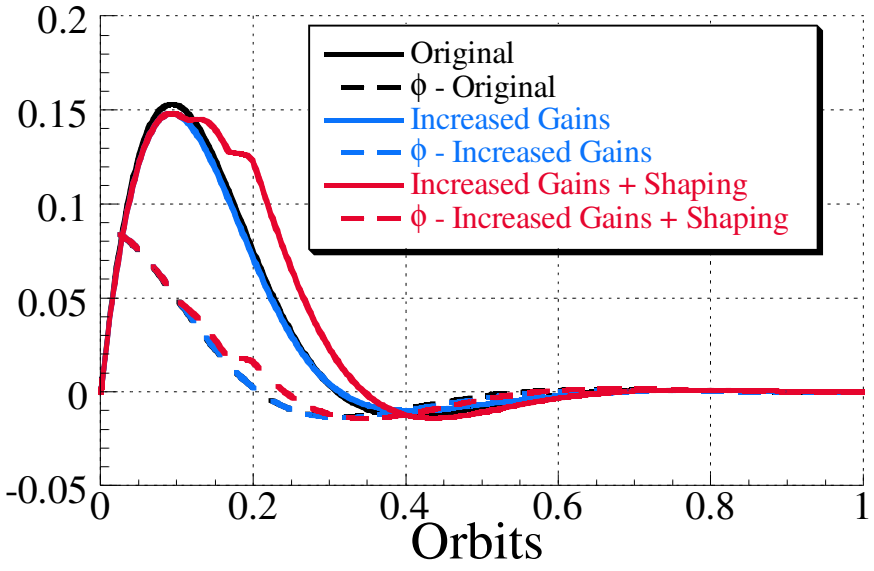

Figure 113: Out-of-plane Swing Angle and Thruster Profiles using Reel-in-Rate Controller.

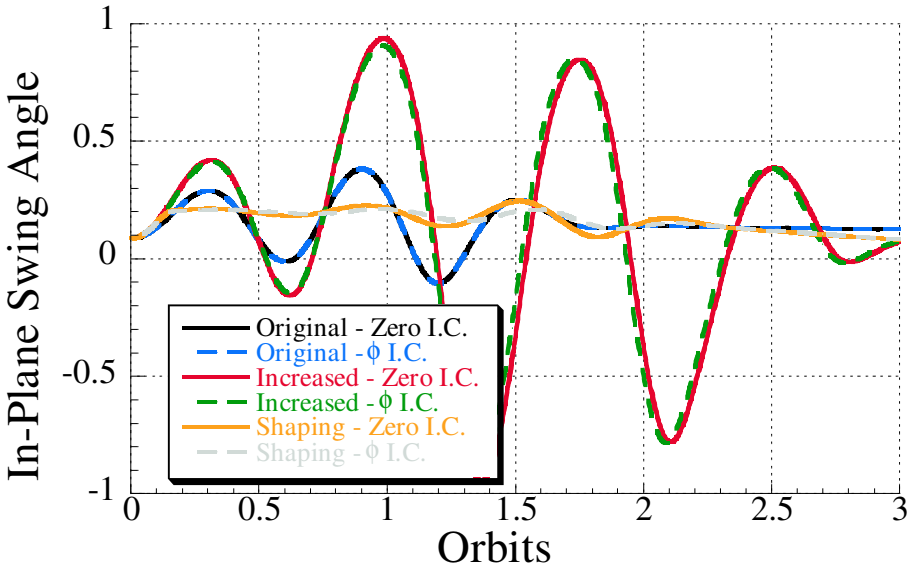

Figure 114: In-plane Swing Angle Profiles using Reel-in-Rate Controller.

chance that the higher gains will lead to instability. The only possible negative effect is the slight increase in out-of-plane thruster usage for the Increased Gains + Shaping case.

4.2 Shaped out-of-plane thruster

In the previous sections, the out-of-plane motion was actively controlled. In this section, the implications of tether retrieval without the out-of-plane control are investigated and a

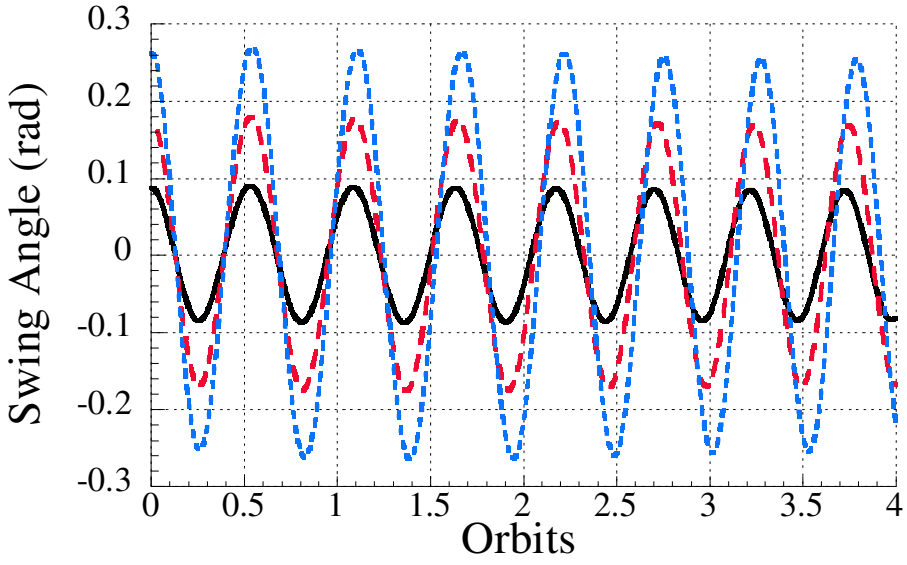

Figure 115: Uncontrolled Out-of-plane Seing Angles, Positive Initial Conditions.

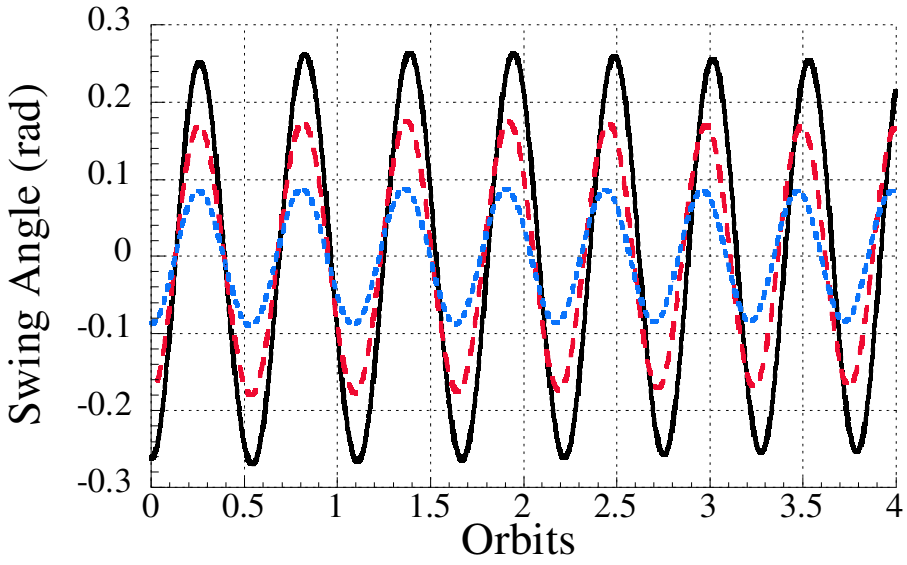

Figure 116: Uncontrolled Out-of-plane Swing Angles, Negative Initial Conditions.

simple open loop law for reducing out-of-plane oscillations is described.

4.2.1 Tether retrieval without out-of-plane control

Most tether control schemes focus on preventing tether slackness and reducing in-plane swing angles, leaving the out-of-plane motion to a separate controller. Figures 115 and 116 show the out-of-plane swing angles when the out-of-plane motion is not controlled using

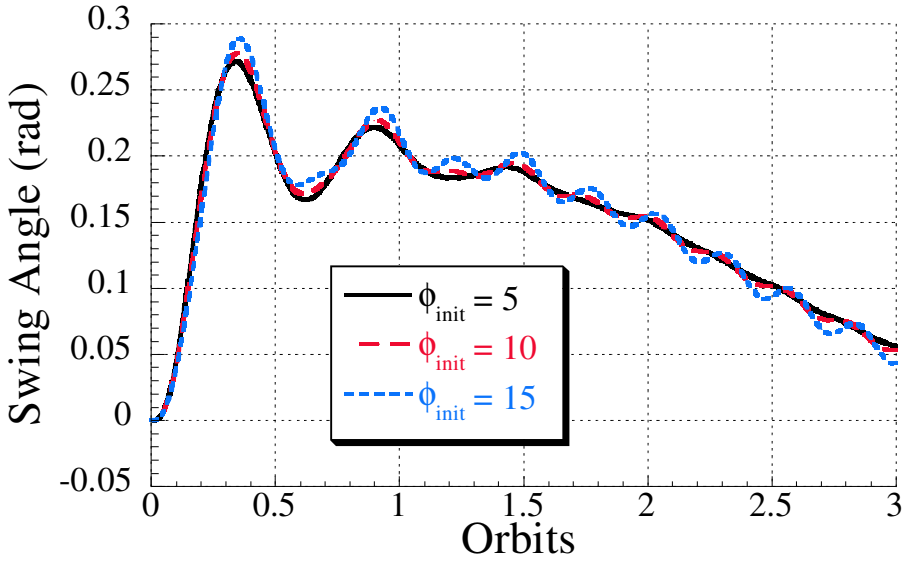

Figure 117: In-plane Swing Angle Profiles without Out-of-plane Thruster.

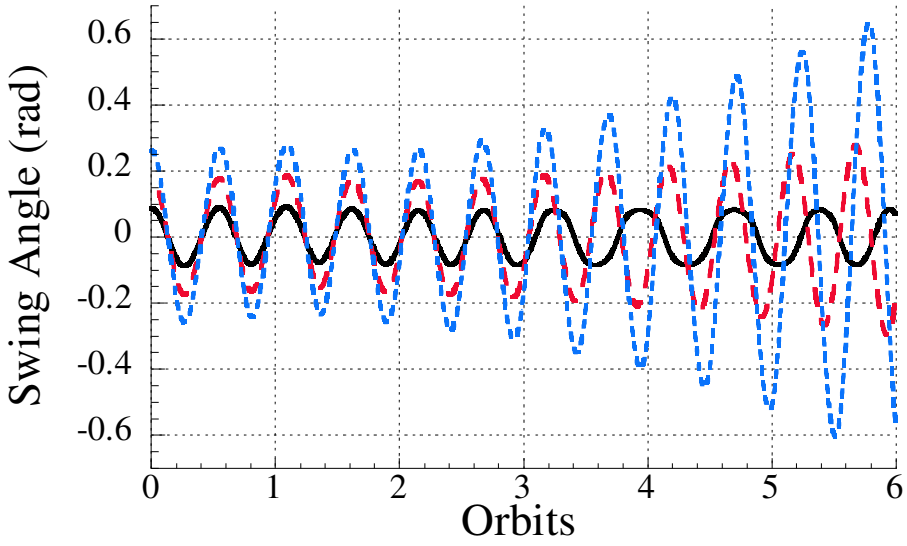

Figure 118: Uncontrolled Out-of-plane Swing Angles, Negative Initial Conditions.

the tension controller. The magnitude of the oscillation is equal to the magnitude of the initial swing angle and the period of oscillation is approximately 0.54 orbits. Without an out-of-plane controller, the effect of the coupling between the in-plane and out-of-plane swing angles in more clearly seen. Figure 117 shows the in-plane swing angle profiles when the out-of-plane motion is not controlled. Increasing the amplitude of the out-of-plane oscillation leads to oscillations in the in-plane swing angle.

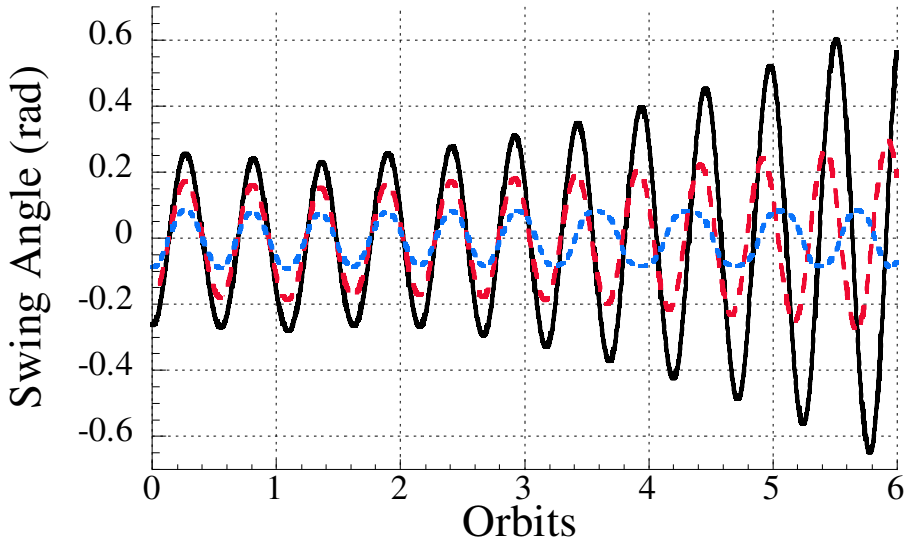

Figure 119: Uncontrolled Out-of-plane Swing Angles, Negative Initial Conditions.

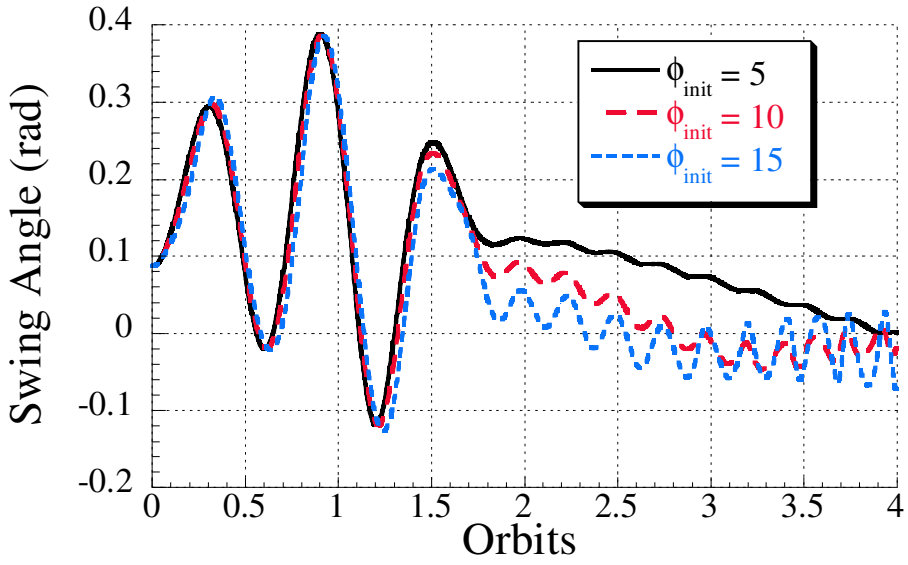

Figure 120: In-plane Swing Angle Profiles without Out-of-plane Thruster.

Figures 118 and 119 show the out-of-plane swing angles when the out-of-plane motion is not controlled using the reel-in-rate controller. For all cases, the period of oscillation is approximately 0.54 orbits. However, for initial swing angles with magnitudes larger the 0.087, the magnitude of the oscillations grow with time. The magnitude of the oscillation doubles in 6 orbits. Figure 120 shows that the increase in oscillations of the out-of-plane angle results in an increase in oscillations in the in-plane angle.

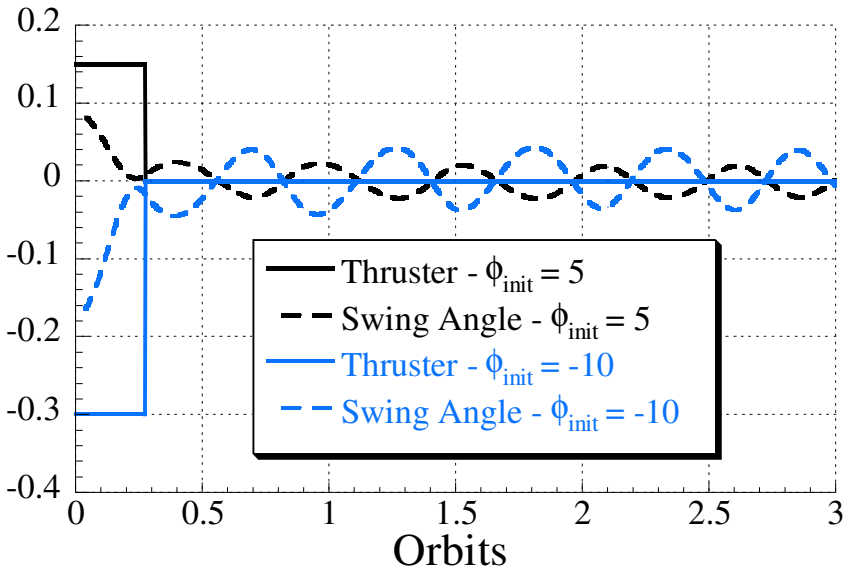

Figure 121: Open-loop Controller.

4.2.2 Open-loop out-of-plane thruster

The out-of-plane control law given by (108) produces thruster profiles that would be difficult to recreate using traditional on-off thrusters. This section presents a simple procedure for producing open loop thruster profiles that will greatly reduce the out-of-plane swing angle.

Figures 109, 110, and 113 showed that the control action response to an initial out-of-plane swing angle was a force that lasted approximately 0.25 orbits and whose magnitude varied with initial condition. Figures 115, 116, 118 and 119 showed that the uncontrolled out-of-plane oscillations have a period of approximately 0.55 orbits. Based in these two observations, an open-loop control law based on the initial out-of-plane swing angle is given by

$$\hat{F} = 0.15 * n \tag{109}$$

where

$$n = \phi_{init}/0.0873 \tag{110}$$

$\hat{F}$ is applied for 0.275 orbits. Figure 121 shows the out-of-plane thruster and swing angle profile for initial angles of 5 and 10 degrees. The open-loop control greatly reduces the oscillations. Figure 122 shows the oscillation amplitude for a given initial out-of-plane swing angle for the uncontrolled case and the open-loop control case. Here the reduction

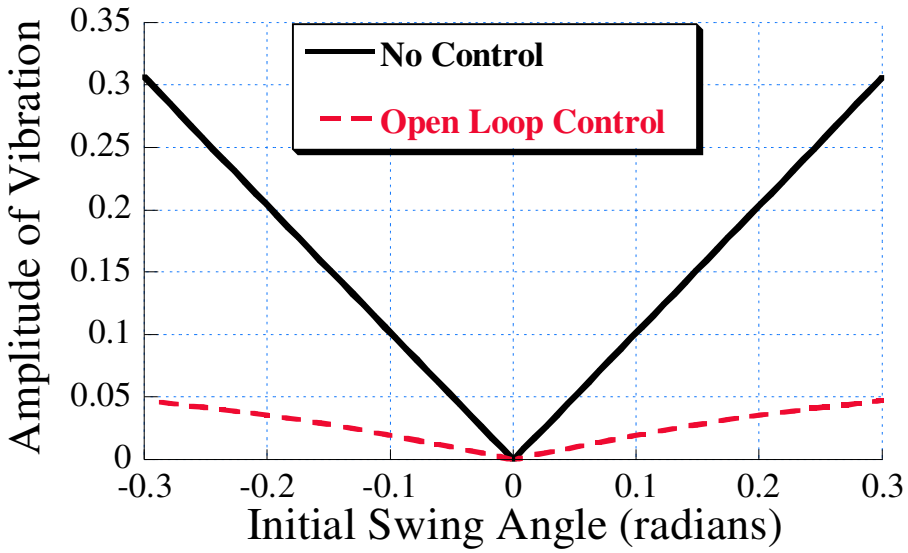

Figure 122: Open-Loop Thruster.

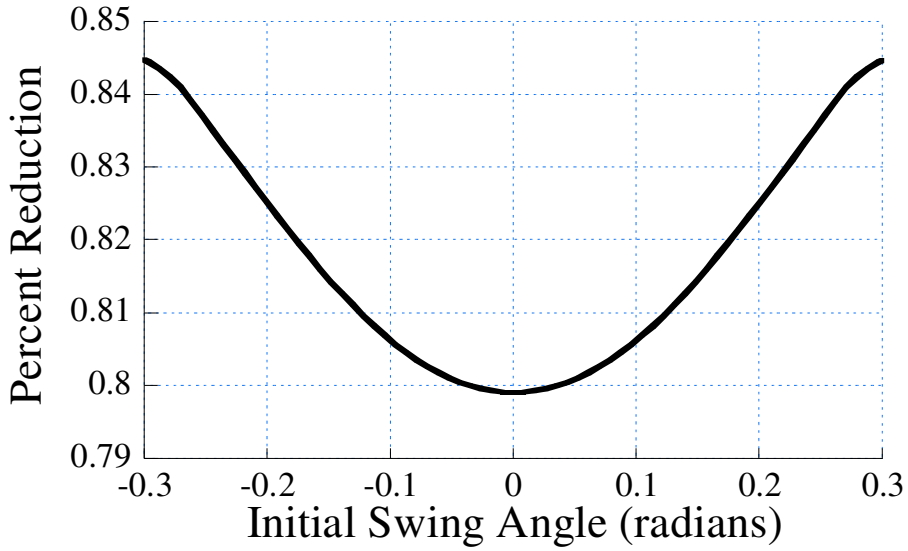

Figure 123: Oscillation Amplitude Reduction using Open-Loop Controller.

in oscillation amplitude is clearly shown. Figure 123 shows the percentage reduction in oscillation amplitude for the range of initial conditions is over 80%.

4.3 3D Tether Summary

In this chapter the three dimensional model of a tether satellite system was used and the effects of the increased gains on the coupling between the in-plane and out-of-plane angles

was investigated. The major findings can be summarized as follows:

- Increasing the gains of the Tension controller does not enhance the coupling between in-plane and out-of-plane angles.
- Increasing the gains of the Reel-in-rate controller does not enhance the coupling between in-plane and out-of-plane angles.
- A simple open-loop control law based on the initial out-of-plane swing angle produces commands that can be easily reproduced using traditional thrusters and reduces the out-of-plane swing angle by 80%.

CHAPTER V

SPINNING TETHERED SATELLITE

The previous chapters developed command shaping methods for reduced tether retrieval time and limited swing angles for earth-pointing tethered satellite systems. This chapter will investigate the utility of command shaping for spinning tethered satellite systems. In these systems, the purpose of tether retrieval is to create large swing angles. These large swing angles are used to induce significant angular velocity about the satellite's center of mass in the orbital plane.

Spinning tethered systems can have many useful applications. Spinning tethered satellites can be used to create artificial gravity fields [35, 70] in an effort to reduce bone density loss and muscle atrophy in humans during extended missions as discussed in Chapter 1. Spinning tethered satellites can also be used to transfer momentum between two spacecraft [14, 22, 27, 46, 58, 68]. The Momentum Exchange, Electrodynamic Reboost (MXER) system has been proposed as method for propellantless boosting of satellites from low to high orbits [68, 21].

Whether the spinning tethered satellite system will be used to momentum exchange or to create an artificial gravity field, the spin-up process is critical to mission success. Variations in angular velocity at the conclusion of the spin-up deteriorates the accuracy of the tether endpoint positioning for momentum exchange and creates fluctuations in the artificial gravity field. This chapter will develop retrieval profiles that will reduce the residual "vibration" of the spin-up process.

5.1 Simple Spinning Tether Model

In an effort to get a greater understanding of the spin-up dynamics, the Tethered Artificial Gravity (TAG) satellite project has been proposed [36]. A model of this system is shown in Figure 124. In this project, a satellite will be delivered in to orbit, automatically separated

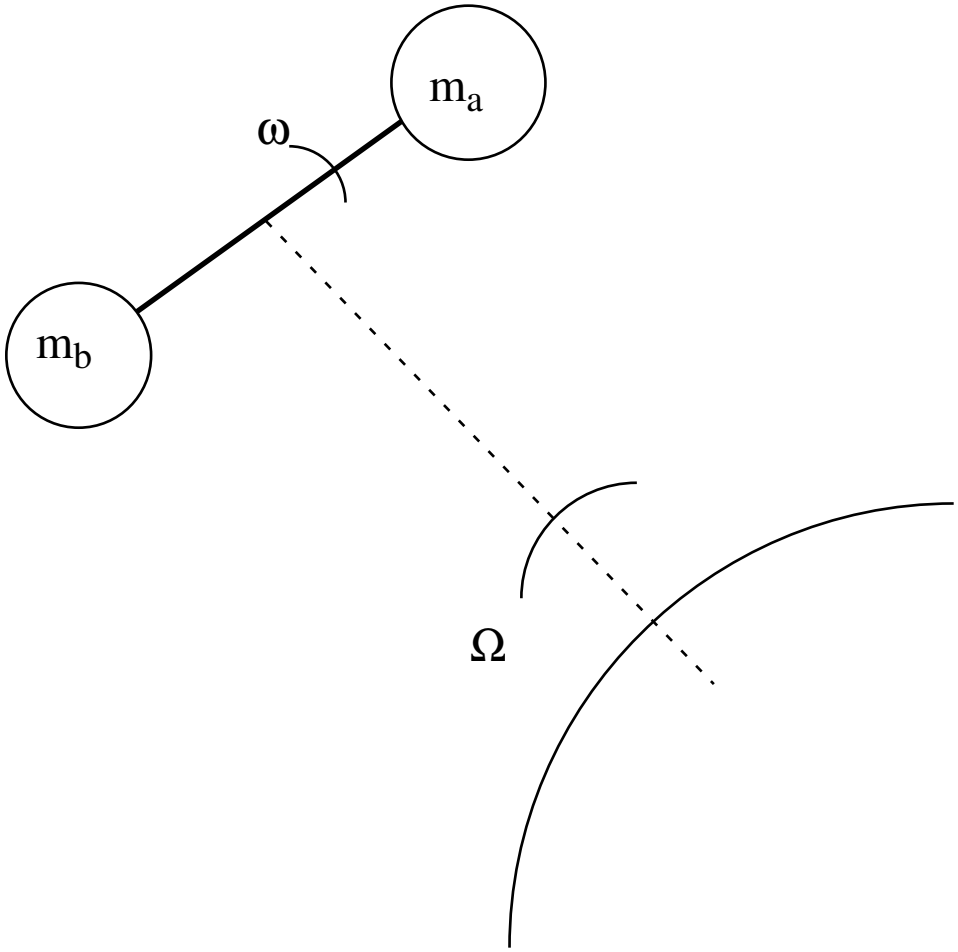

Figure 124: Tethered Artificial Gravity Satellite System.

into roughly equal masses and connected by 2000 meters of tether. Retrieval will be used to generate a rapid increase in rotational motion of the system. If the motion of the system is constrained to the orbital plane, the two sections of the satellite are modeled as point masses and the tether is assumed to be massless and rigid and remain straight throughout the retrieval process, then the equations of motion can be given by:

$$\ddot{L} - L(\dot{\theta}^2 + 2\Omega\dot{\theta} + 3\Omega cos^2(\theta)) = T/\bar{m} \tag{111}$$

$$\ddot{\theta} + 2(\dot{L}/L)(\Omega + \dot{\theta}) + \frac{3}{2}\sin 2\theta = 0 \tag{112}$$

where

$$\bar{m} = \frac{m_a m_b}{m_a + m_b} \tag{113}$$

and m_a and m_b are the masses of the two portions of the satellite, L is the length of the tether, θ is the in-plane swing angle, Ω is the orbital angular velocity and T is the tether tension. The TAG will use a simple exponential control for the length of the tether given by

$$L(t) = L_i \exp(-ct) \tag{114}$$

where L_i is the length of the tether at the start of the spin-up process and c is the decay rate. If the desired final length, L_f, and the length of time of the spin-up process, t_r are fixed, the c is given by

$$c = \frac{ln(L_i/L_f)}{t_r} \tag{115}$$

The final value of the angular velocity is dependant on both the rate of retrieval and the initial swing angle. Figure 125 shows the final angular velocity in radians per second for a retrieval from 2000 to 100 meters and an orbital rate of 0.0011636 radians per second (90 minute orbital rate) as a function of the decay rate, c, and values of the initial swing angle +/- 90 degrees. The final angular velocity is heavily dependant on the initial swing angle. Initiating retrieval when the swing angle is negative will lead to significant rotation rates. Figure 126 shows angular velocity profiles for a retrieval rate of 5.5e-4, or a retrieval time of approximately 90 minutes. The final angular velocities for the negative initial swing angles are much higher than those for the positive initial swing angles.

In an effort to better understand the retrieval rate's effect on the final angular velocity, retrieval with positive initial swing angles and varying retrieval rates were simulated. Figure 127 shows the effect of the retrieval rate on the final angular velocity with an initial zero swing angle. Increasing the decay rate increases the final angular velocity. This is not the case for a 30 or a 60 degree initial swing angle, as shown in Figures 128 and 129, respectively. For these initial conditions, increasing the retrieval rate decreases the final angular velocity. For the highest retrieval rate, there is no constant, positive angular velocity. Figure 130 shows that there are large swing angle oscillations, but no rotation.

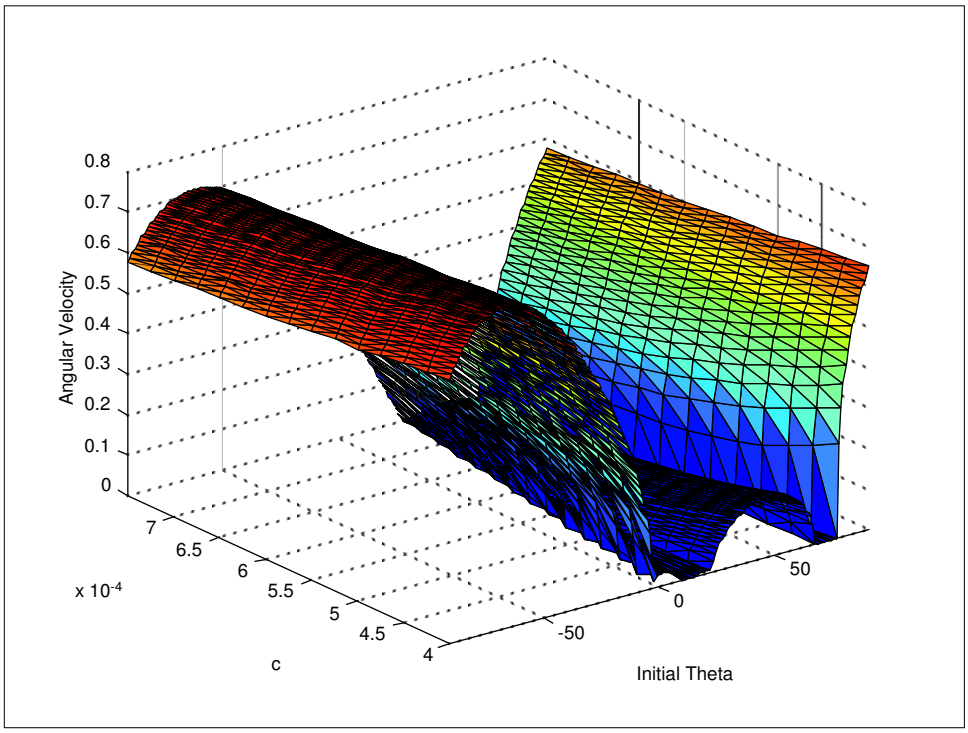

Figure 125: Effect of Initial Swing Angle and Retrieval Rate on Final Angular Velocity.

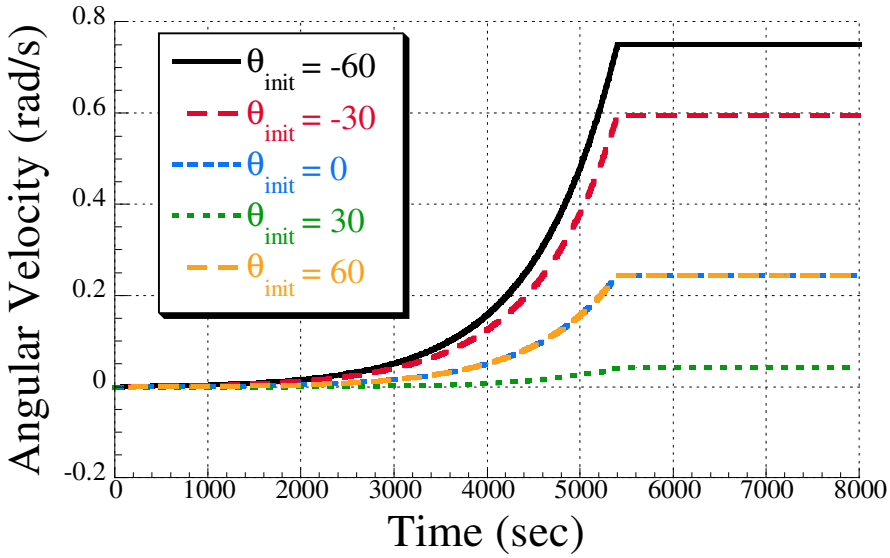

Figure 126: Effect of Initial Swing Angle, Constant Retrieval Rate.

5.2 Spinning Tethered System with Extensible Tether

The previous section demonstrated that for the simple tether model, the initial swing angle has the greatest influence on the final angular velocity. Negative initial swing angles are

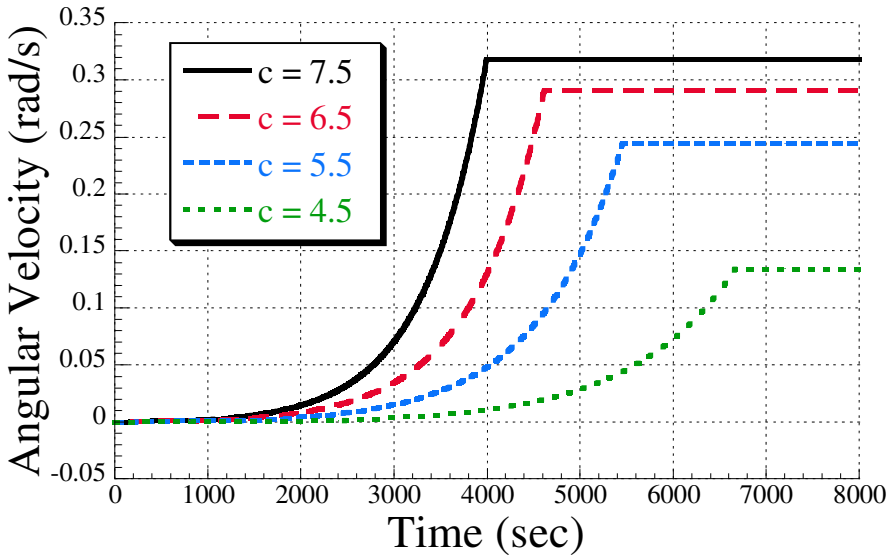

Figure 127: Effect of Retrieval Rate on Angular Velocity, Zero Initial Swing Angle.

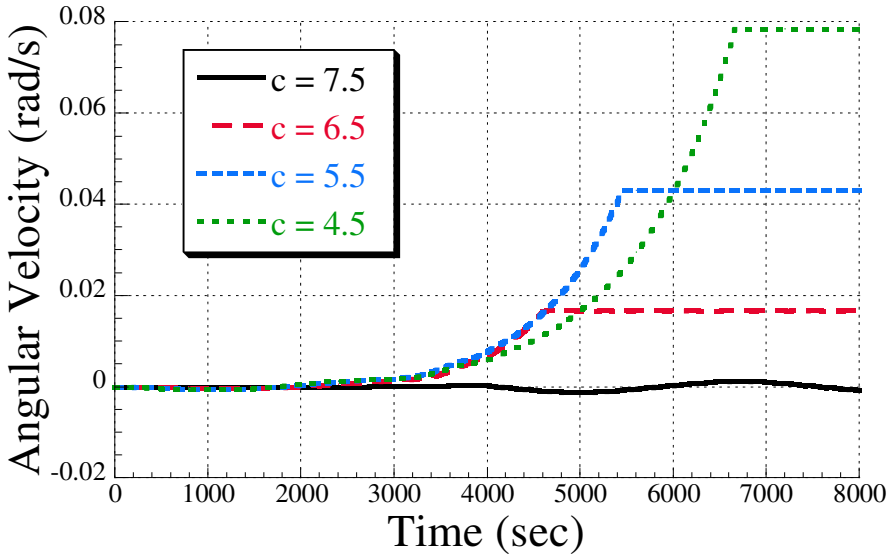

Figure 128: Effect of Retrieval Rate on Angular Velocity, 30 Degree Initial Swing Angle.

ideal, but for positive angles the spin rate can be improved by adjusting the retrieval rate. This section investigates the effect tether extensibility has on the final angular velocity and presents a command shaping scheme to reduce vibration.

In this model, the motion of the system is again constrained to the orbital plane, the two sections of the satellite are modeled as point masses and the tether is assumed to be massless and remains straight throughout the retrieval process. If the elasticity of the tether

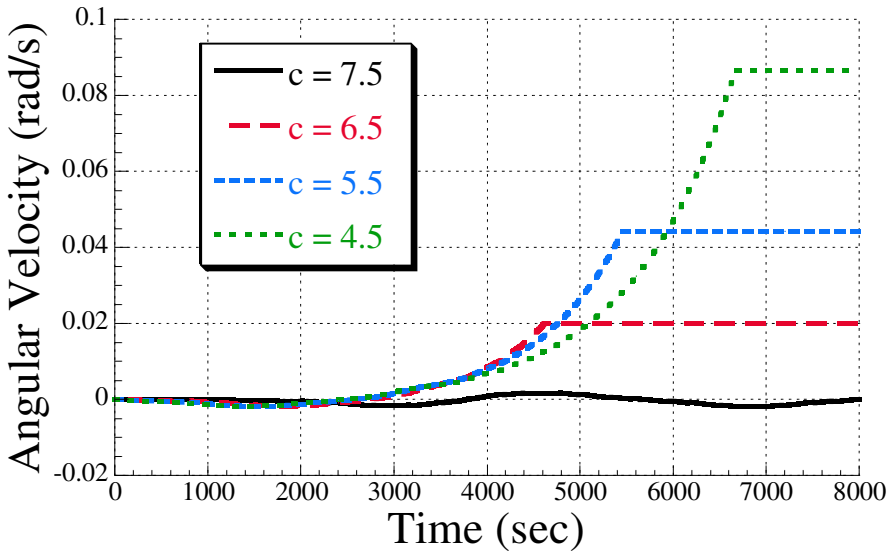

Figure 129: Effect of Retrieval Rate on Angular Velocity, 60 Degree Initial Swing Angle.

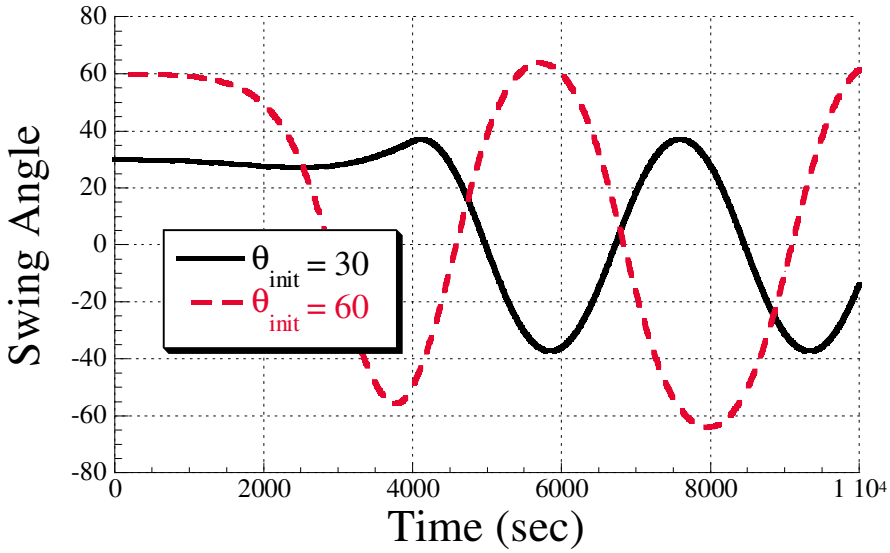

Figure 130: Swing Angle for Fast Retrieval.

is modeled linearly by Hooke's Law, then the equations of motion can be given by [36]:

$$\ddot{L} - L(\dot{\theta}^2 + 2\Omega\dot{\theta} + 3\Omega cos^2(\theta)) + \frac{EA}{\bar{m}}\epsilon U(\epsilon) = T/\bar{m} \tag{116}$$

$$\ddot{\theta} + 2(\dot{L}/L)(\Omega + \dot{\theta}) + \frac{3}{2}\sin 2\theta = 0 \tag{117}$$

where E is the modulus of elasticity of the tether, A is the cross sectional area of the tether, $\epsilon = (L - L_0)/L_0$, L_0 is the unstretched length of the tether, $U()$ is the unit step function

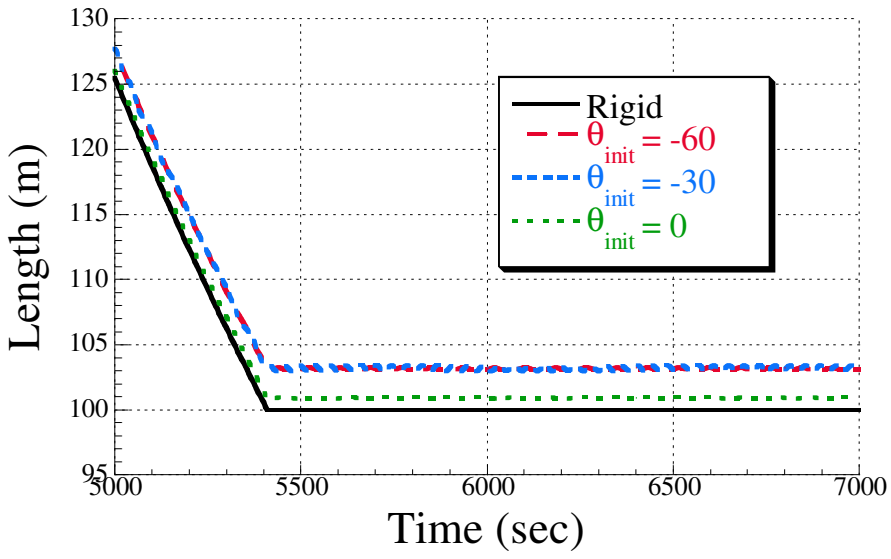

Figure 131: Length Profile using Extensible Tether Model, Negative Initial Swing Angles.

with L, θ and Ω defined as above.

In the TAG satellite project, the portions of the satellite, m_a and m_b will be 40 kg and 25 kg, respectively. The tether stiffness, EA is 10000 N and the orbital rate is 0.0011636 (90-minute orbital period). The tether will be retrieved from an initial length of 2000 meters to a final length of 100 meters in 90 minutes. This results in retrieval rate of $c = 5.5377e-4$. Figure 131 shows the length profile for initial swing angles of -60, -30 and 0 degrees. The cases with flexible tethers do not end with exactly 100 meters of satellite seperation because there is some extension in the tether. There is also a small amount of longitudinal vibration for the larger initial swing angles. Figure 132 shows a comparison of the final angular velocity of the rigid and extensible tethers. Again, there are only small differences between the two cases.

Figure 133 shows the angular velocity for initial swing angles of 60, 65 and 70 degrees using the extensible tether model. All three cases have oscillation about the final value. Both the frequency and the average angular velocity decrease with initial swing angle. In fact, the angular velocity is negative for the 70 degree initial swing angle. The variations in angular velocity result in variations in the artificial gravity field that can be uncomfortable for humans and may negatively effect experiments and electronic components aboard the

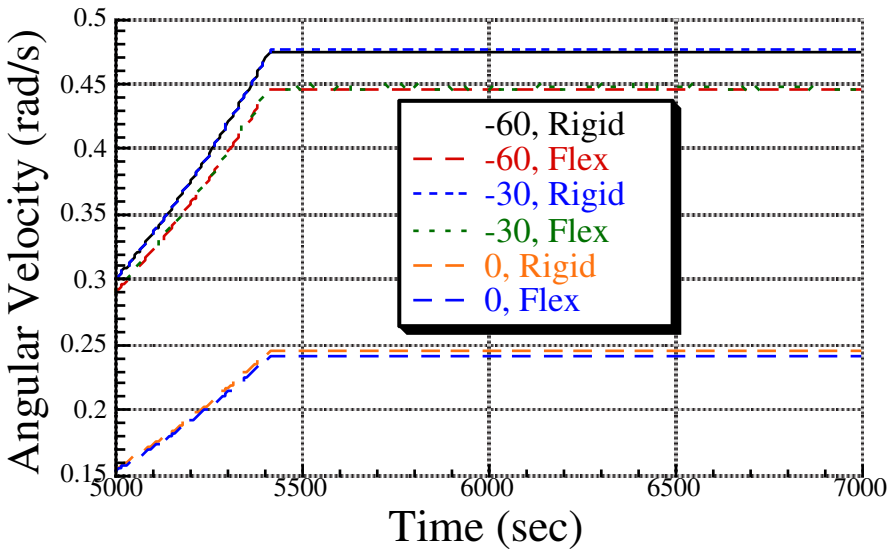

Figure 132: Angular Velocity using Extensible Tether Model, Negative Initial Swing Angles.

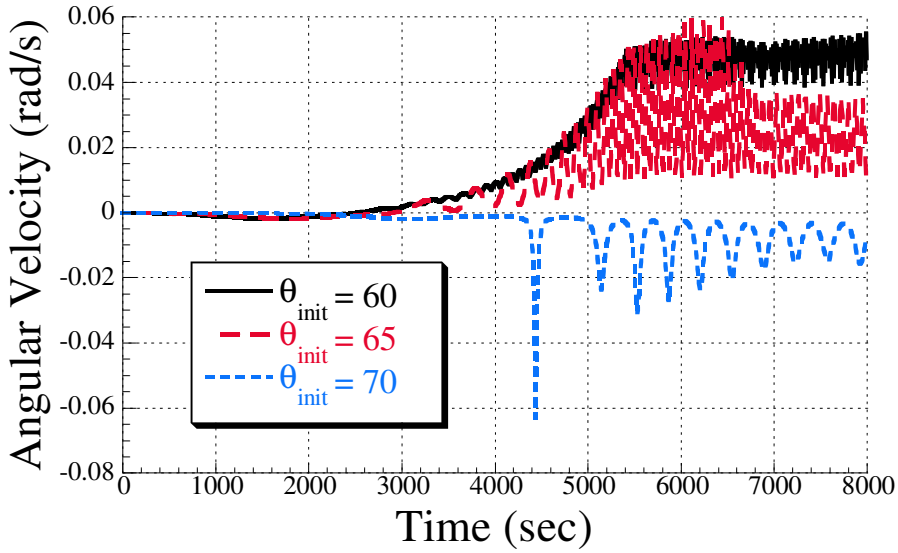

Figure 133: Angular Velocity using Extensible Tether Model, Positive Initial Swing Angles.

system.

Figure 134 shows the length profile for these initial swing angles. There are large oscillations in the tether length and the amplitude of the oscillations increase with initial swing angle. The oscillations occur because the tether can only apply a force when it is in tension (i.e. when the length is greater than 100). The tether force is opposed by the centripetal force $f_c = m\omega^2 L$. Lower angular velocities require longer amounts of time to overcome the

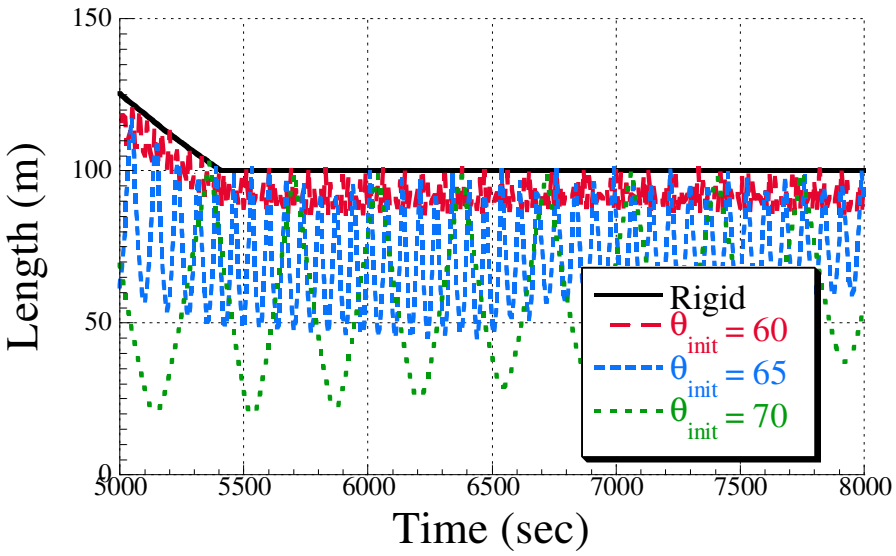

Figure 134: Length Profile using Extensible Tether Model, Positive Initial Swing Angles.

tension force applied by the tether. Higher angular velocities mean higher f_c, which would keep the tether length closer to the desired final length.

Figures 135, 136 and 137 show the effect of the retrieval rate, c, on the angular velocity. For the 60 degree initial swing angle shown in Figure 135, the fastest retrieval, $c = 7.5e-4$, has the highest angular velocity and the highest variation amplitude. Interestingly, the slowest retrieval has the second highest angular velocity and variation. These trends hold for the 65 degree initial swing angle shown in Figure 136, with $c = 6.5e-4$ having both the lowest angular velocity and variation amplitude. The 70 degree initial swing angle, shown in Figure 137, has different characteristics. Increasing the retrieval rate leads to positive angular velocities. Unfortunately, increasing the retrieval rate also leads to increased variation amplitudes.

The length profiles for the 60, 65 and 70 degree initial conditions are shown in Figures 138, 139 and 140, respectively. The slowest retrieval rate has the highest variations in length for the 60 degree initial condition in Figure 138. The faster retrieval has the second highest variation. For all retrieval rate except $c = 4.5e-4$, the tether is in tension. Increasing the retrieval rates leads to decreased variation amplitudes and increased tether length for initial conditions of 65 and 70 degrees. This section demonstrated the complicated dynamics that

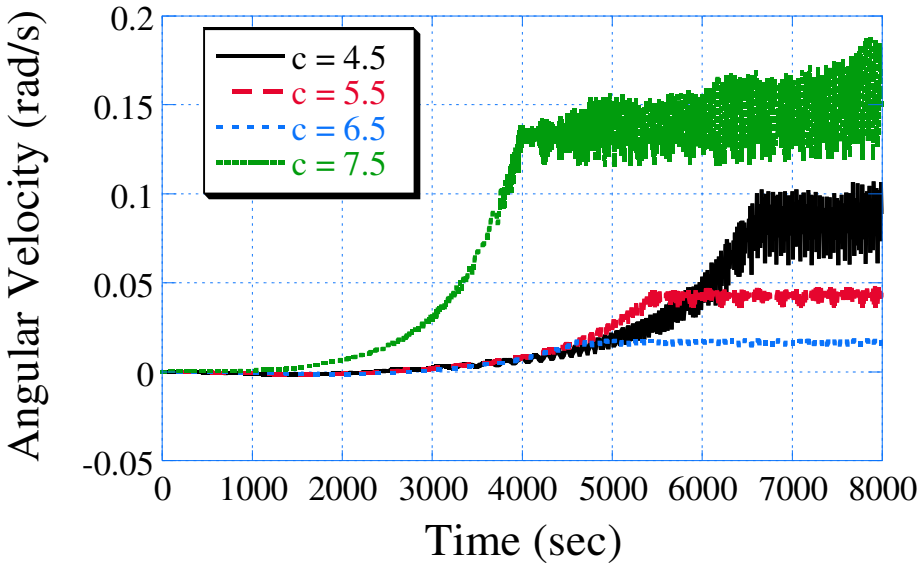

Figure 135: Angular Velocity using Extensible Tether Model, 60 Degree Initial Swing Angle.

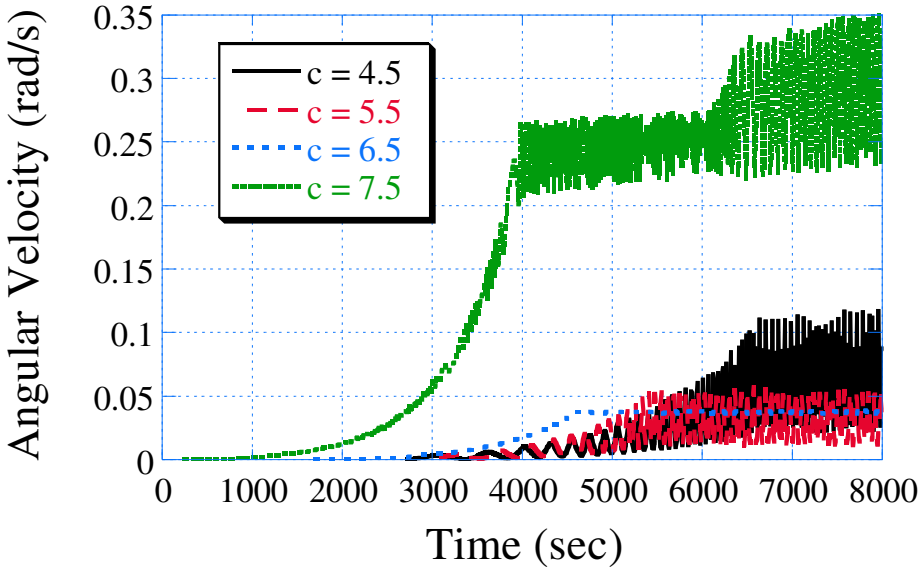

Figure 136: Angular Velocity using Extensible Tether Model, 65 Degree Initial Swing Angle.

exist during satellite spin-up. Both the initial angle and the retrieval rate greatly affect the final angular velocity and tether length. Arbitrarily setting the retrieval rate will, in general, not result in desired performance. In the next section, a command shaping scheme will be presented that will increase the final overall angular velocity of the system and decrease the variations in angular velocity and tether length.

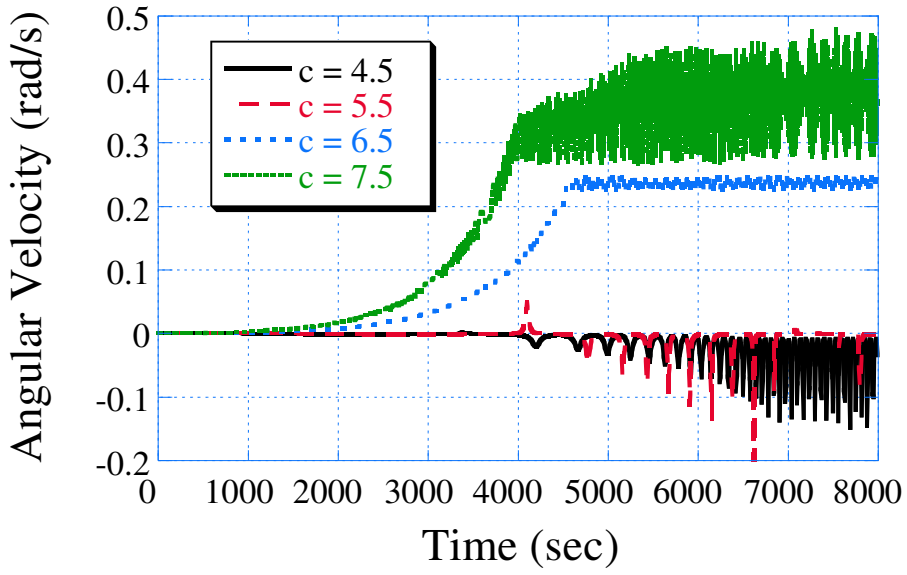

Figure 137: Angular Velocity using Extensible Tether Model, 70 Degree Initial Swing Angle.

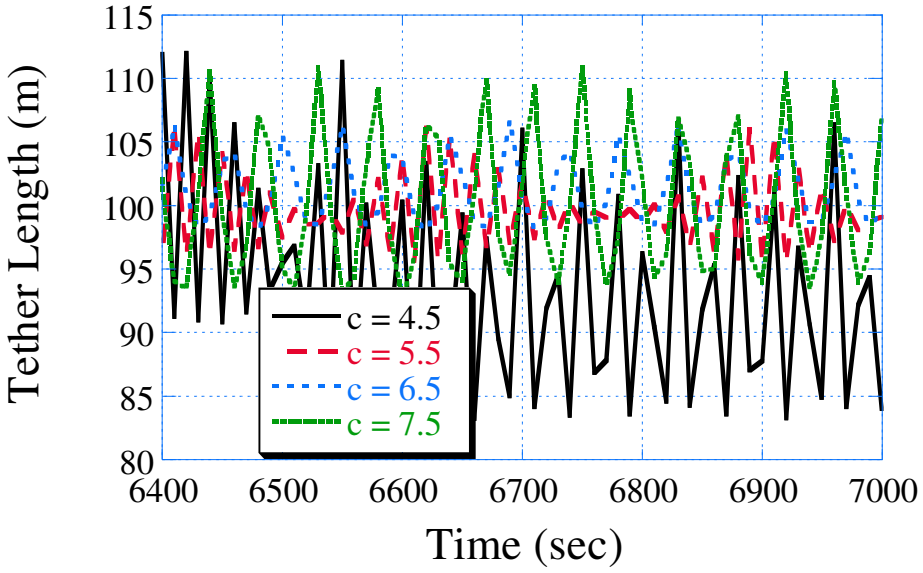

Figure 138: Tether Length using Extensible Tether Model, 60 Degree Initial Swing Angle.

5.3 Command Shaping for Extensible Tether

The previous section demonstrated the retrieval rate's effect on the final angular velocity, and the variations in the final angular velocity and the final tether length. Increasing the retrieval rate can have the desirable effect of increasing angular velocity and the undesirable effect of increasing variations. A shaping scheme to reduce the undesirable effects is

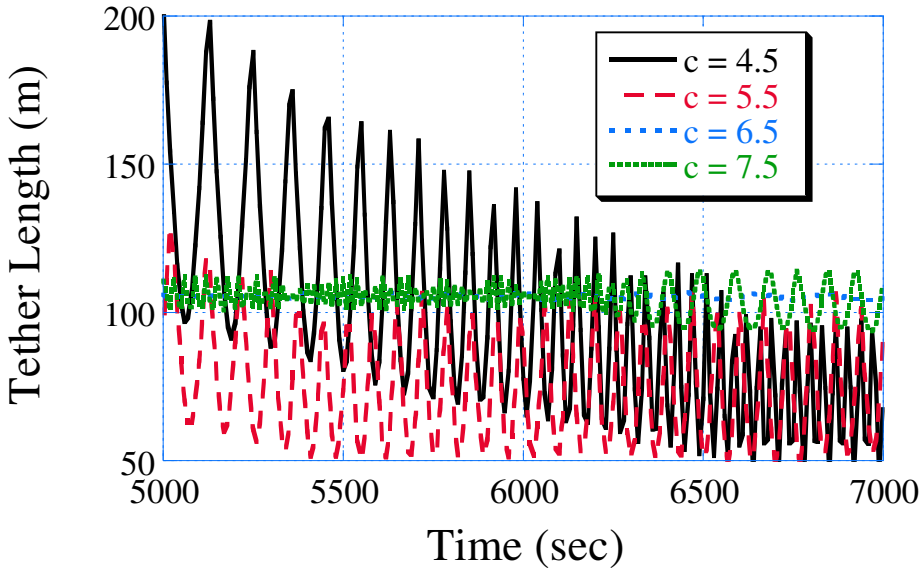

Figure 139: Tether Length using Extensible Tether Model, 65 Degree Initial Swing Angle.

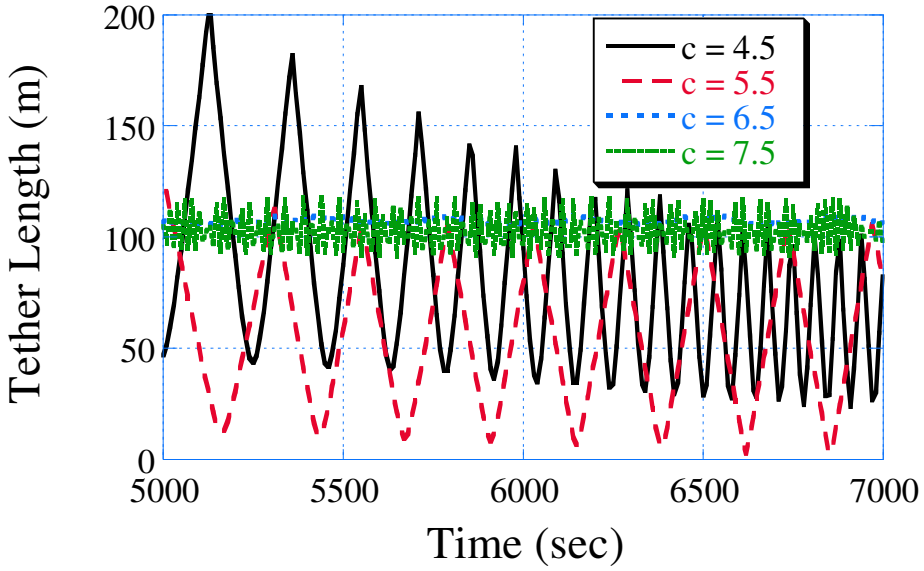

Figure 140: Tether Length using Extensible Tether Model, 70 Degree Initial Swing Angle.

presented in this section.

Based on observations of Figures 135 - 140, the following methodology is used to create retrieval profiles: 1) use a retrieval rate, c_1, that results in high angular velocity for a brief amount of time to initiate retrieval, 2) use a retrieval rate, c_2, that results in low variations to complete the retrieval 3) the time to switch from the first to the second retrieval rate is

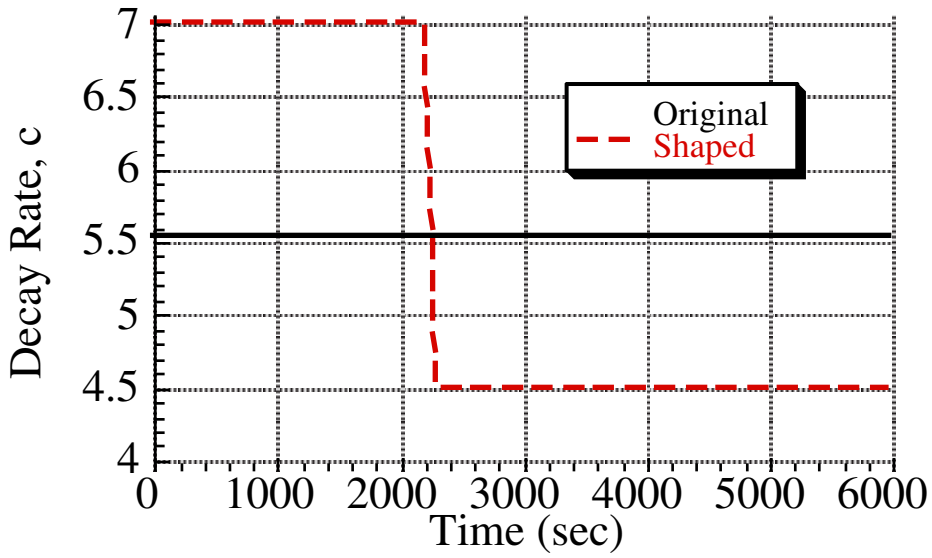

Figure 141: Shaped Retrieval Rate Example.

given by

$$t_{switch} = \frac{\log(l_{init}/l_{switch})}{c_1 - c_2} \tag{118}$$

where it is assumed that $c_1 > c_2$. The tether length when the retrieval rate changes, l_{switch}, is given by

$$l_{switch} = \exp(c_2 t_r) l_{final} \tag{119}$$

Figure 141 shows an example of a shaped retrieval rate. The values of c_1 and c_2 are chosen using an optimization routine with the goal of maximizing angular velocity while keeping variations in angular velocity and tether length low. The retrieval must be completed in 90 minutes, the retrieval time of the unshaped case.

Figure 142 compares the angular velocities resulting from the original and the shaped retrieval profiles. The retrieval rates for the shaped profiles are given in Table 5. For the 60 degree initial swing angle, the shaped profile's angular velocity is slightly less than three times that of the original, with no significant increase in the variation of the angular velocity. For the 65 degree initial swing angle, the shaped profile's angular velocity is approximately nine times that of the original, with a 40% decrease in the variation of the final angular velocity. The 70 degree initial has the largest increase in and overall value of and variation in angular velocity.

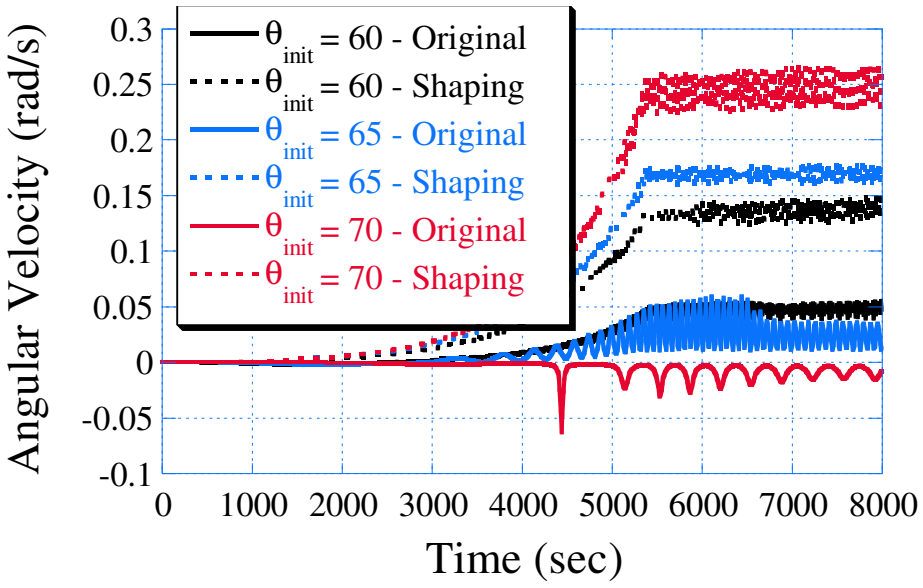

Figure 142: Angular Velocity.

Table 5: Retrieval Rates for Shaped Profiles.

	c_1	c_2
60	7.5e-4	5.0e-4
65	7.0e-4	5.0e-4
70	6.5e-4	5.5e-4

Figure 143 shows the tether lengths resulting from the original and the shaped retrieval profiles. The shaped profiles result in tether lengths with variations of approximately six meters, a great improvement of the variations in length exhibited by the original profiles.

Given the nonlinearity of the system, there are no substantial correlations between initial swing angle and the values c_1 and c_2 used to create the shaped profile. The effect of the retrieval rate, which has been shown to effect each initial swing angle differently, must first be determined before the retrieval rates can be chosen. Once this effect is known, the shaping procedure can then be applied.

5.4 Summary

In this chapter a model of a spinning tether satellite system was used to investigate the effect of command shaping the spin-up process has on the final angular velocity. The major findings can be summarized as follows:

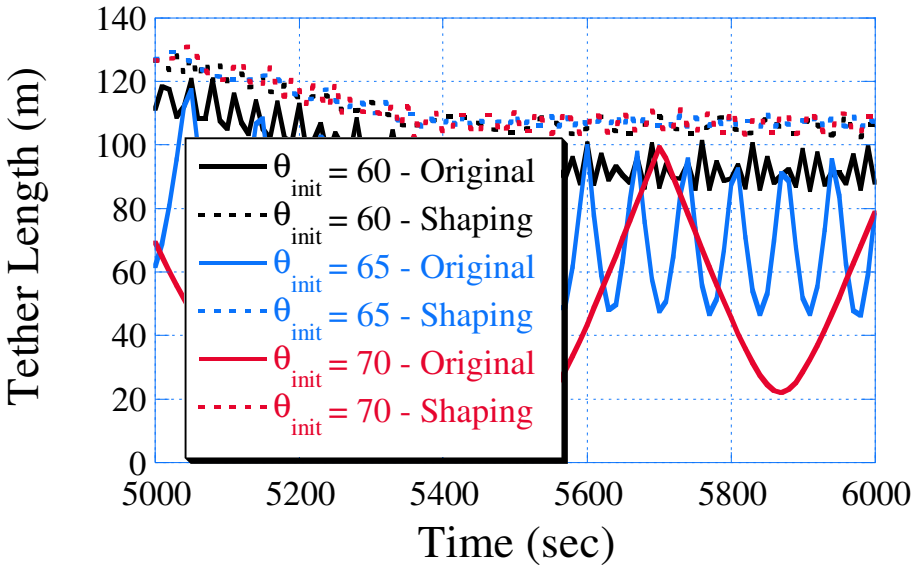

Figure 143: Tether Length.

- Command generation can increase the final angular velocity for a spinning systems.
- Command shaping the retrieval rate reduces vibration in the extensible model.

CHAPTER VI

CONCLUSION

This dissertation has examined a number of issues in command generation for tethered satellite systems and the more general area of limiting transient deflection of flexible systems. The improvements in these fields can be summarized as follows:

Deflection-Limiting Commands

The simplest satellite models assume the satellite is a point mass. For this model, trajectory tracking is the major objective. For satellite models that account for the flexibility in the system, commands that move the system with limited transient deflection in addition to zero residual vibration are desired. This dissertation presented the following contributions to this area:

- Creation of Specified Deflection, Zero Vibration (SD-ZV) command shapers for a mass under PD control
- Derivation of Analytic Deflection-Limiting Commands
- Experimental Verification of Analytic Deflection-Limiting Commands
- Development of analysis tools for rest-to-rest deflection-limiting commands
- Creation of robust transitions for analytic deflection-limiting commands
- Demonstration of the utility of deflection-limiting command shapers for Electrodynamic Reboost

The SD-ZV shapers and analytic deflection-limiting commands were developed for systems with one flexible mode. The effectiveness of these commands will be reduced if implemented on a system whose with multiple flexible modes. Future work includes developing these analytic commands for multi-mode systems.

Tethered Satellite Retrieval

The retrieval of tethered satellites is an inherently unstable process. Feedback controllers have been developed to ensure convergence, but the controller gains must be selected to balance retrieval time and in-plane swing angle. Out-of-plane motion can affect the retrieval process. Most current controllers assume that the out-of-plane swing angle can be actively controlled by a variable amplitude thruster. This dissertation presented the following contributions to this area:

- A technique for combining command shaping and controller feedback gain selection to reduce tether retrieval time and swing angle
- Verification that command shaping developed for full retrieval can be used for partial tether retrieval
- A procedure for creating a command shaping scheme developed to reduce the effect of initial swing angle
- A simple open-loop control law based on the initial out-of-plane swing angle produces commands that can be easily reproduced using traditional thrusters and reduces the out-of-plane swing angle by 80%

A simple tether model was used to develop command shapers for tether retrieval. Using a more representative tether model may result in different values of retrieval time and swing angle reduction. Future work includes simulations using a model that accounts for the tether's flexibility and extensibility and developing shaper design methods less dependant on numerical optimization routines.

Spinning Tethered Satellite Systems

Spinning tethered satellite system have great potential in the areas of artificial gravity generation and momentum exchange between satellites. Spinning the system up to the desired angular velocity with low levels of longitudinal vibration and angular velocity variations is major goal. This dissertation presented the following contributions to this area:

- Development of a methodology to generate shaped retrieval profiles

- Creation of retrieval profiles to increase final angular velocity and reduce tether vibration

The retrieval profiles develop are only applicable to the TAG current system model. Different TAG system models or spin-up strategies will require new retrieval profiles. Future work includes the testing of the current retrieval profile development procedure on different models and the creation of profiles that are effective for a wide range of initial conditions.

These results make a significant contribution to the field of command generation for tethered satellite systems and have developed a framework for future solutions using more representative satellite and tether models.

REFERENCES

[1] Ahedo, E. and Sanmartin, J. R., "Analysis of bare-tether system for deorbiting low-earth-orbit satellite," *Journal of Spacecraft and Rockets*, vol. 39, no. 2, pp. 198–205, 2002.

[2] Banerjee, A. K., "Dynamics and control of the wisp shuttle-antennae syste,," *The Journal of the Astronautical Sciences*, vol. 41, no. 1, pp. 73–90, 1993.

[3] Banerjee, A. K. and Kane, T. R., "Tethered satellite retrieval with thruster augmentation," *Journal of Guidance*, vol. 7, no. 1, pp. 45–50, 1984.

[4] Barkow, B., Steindl, A., Troger, H., and Wiedermann, G., "Various methods of controlling the deployment of a tethered satellite," *Journal of Vibration and Control*, vol. 9, pp. 187–208, 2003.

[5] Ben-Asher, J., Burns, J. A., and Cliff, E. M., "Time-optimal slewing of flexible spacecraft," *Journal of Guidance, Control, and Dynamics*, vol. 15, no. 2, pp. 360–367, 1992.

[6] Bhat, S. P. and Miu, D. K., "Precise point-to-point positioning control of flexible structures," *Journal of Dynamic Systems, Measurement, and Control*, vol. 112, no. 4, pp. 667–674, 1990.

[7] Biswell, B. and Puig-Suari, J., "Stability and control of an atmospheric tether with a lifting probe," *Journal Guidance, Control, and Dynamics*, vol. 22, no. 5, pp. 664–670, 1999.

[8] Bolz, R. E. and Tuve, G. L., *CRC Handbook of Tables for Applied Engineering Science*. Boca Raton, FL: CRC Press, Inc., 1973.

[9] Cannon, R. H. and Schmitz, E., "Initial experiments on the end-point control of a flexible one link robot," *International Journal of Robotics Research*, vol. 3, no. 3, 1984.

[10] Cho, S. and McCamroch, N. H., "Optimal orbit transfer of a spacecraft with fixed length tether," *The Journal of the Astronautical Sciences*, vol. 51, no. 2, pp. 195–204, 2003.

[11] Estes, R. D., Lorenzini, E. C., Sanmartin, J., Pelaez, J., Martinez-Sanchez, M., Johnson, C. L., and Vas, I. E., "Bare tethers for electrodynamic spacecraft propulsion," *Journal of Spacecraft and Rockets*, vol. 37, no. 2, pp. 205–211, 2000.

[12] Feddema, J., Dohrmann, C., Parker, G., Robinett, R., Romero, V., and Schmitt, D., "A comparison of maneuver optimization and input shaping filters for robotically controlled slosh-free motion of an open container of liquid," in *American Control Conference*, (Albuquerque, NM), 1997.

[13] Forward, R. and Nordley, G., "Mars-earth rapid interplanetary tether transport (meritt) system: Initial feasibility analysis," in *35th AIAA/ASME/ASEE Joint Propulsion Conference*, 1999.

[14] Forward, R. L., "Tether transport from leo to the lunar surface," in *27th AIAA/ASME/ASEE Joint Propulsion Conference*, (Sacramento, CA), 1991.

[15] Forward, R. L., Hoyt, R. P., and Uphoff, C. W., "Terminator tether: A spacecraft deorbit device," *Journal of Spacecraft and Rockets*, vol. 37, no. 2, pp. 187–196, 2000.

[16] Fujii, H. A. and Anazawa, S., "Deployment/retrieval control of tethered satellite through an optimal path," *Journal of Guidance, Control and Dynamics*, vol. 17, no. 6, pp. 1292–1298, 1994.

[17] Fujii, H. A., Fujiki, T., Watanabe, T., Taira, W., Murase, T., and Trivailo, P., "Control of tethered system by using transverse motion of tether," in *AIAA/AAS Astrodynamics Specialist*, 2001.

[18] Fujii, H. A. and Kojima, H., "Optimal trajectory analysis for deployment/retrieval of tethered satellite using metric," *Journal of Guidance*, vol. 26, no. 1, pp. 177–179, 2002.

[19] Heide, E. J. v. d. and Kruijff, M., "Tethers and debris mitigation," *Acta Astonautica*, vol. 48, pp. 503–516, 2001.

[20] Hoyt, R., "Commercial development of a tether transport system," in *36th AIAA/ASME/ASEE Joint Propulsion Conference*, 2000.

[21] Hoyt, R. P., "Momentum-exchange/electrodynamic-reboost tether facility for deployment of microssatellites to geo and the moon," in *Space Technology and Applications International Forum*, 2001.

[22] Hoyt, R. P. and Uphoff, C., "Cislunar tether transport system," *Journal of Spacecraft and Rockets*, vol. 37, no. 2, pp. 177–186, 2000.

[23] Johnson, L., Gilchrist, B., Estes, R. D., and Lorenzini, E., "Overview of future nasa tether applications," *Adv. Space Res.*, vol. 24, no. 4, pp. 1055–1063, 1999.

[24] Johnson, L., Estes, R. D., Lorenzini, E., Martinez-Sanchez, M., and Sanmartin, J., "Propulsive small expendable deployer system experiment," *Journal of Spacecraft and Rockets*, vol. 37, no. 2, pp. 173–176, 2000.

[25] Kim, E. and Vadali, S. R., "Modeling issues related to retrieval of flexible tethered satellite systems," *Journal of Guidance, Control and Dynamics*, vol. 18, no. 5, pp. 1169–1176, 1995.

[26] Kokubun, K. and Fujii, H. A., "Deployment/retrieval control of a tethered subsatellite under effect of tether elasticity," *Journal of Guidance, Control and Dynamics*, vol. 19, no. 1, pp. 84–90, 1996.

[27] Kumar, K. D., "Payload deployment by reusable launch vehicle using tether," *Journal of Spacecraft and Rockets*, vol. 38, no. 2, pp. 291–294, 2001.

[28] Kumar, K. D. and Kumar, K., "Attitude maneuver of dual tethered satellite platforms through tether offset change," *Journal of Spacecraft and Rockets*, vol. 38, no. 2, pp. 237–242, 2001.

[29] Lanoix, E. L. M. and Misra, A. K., "Near-earth asteriod missions using tether sling shot assist," *Journal of Spacecraft and Rockets*, vol. 37, no. 4, pp. 475–480, 2000.

[30] Leamy, M. J., Noor, A. K., and Wasfy, T. M., "Dynamic simulation of a tethered satellite system using finite elements and fuzzy sets," *Computer Methods in Applied Mechanics and Engineering*, vol. 190, pp. 4847–4870, 2001.

[31] Liaw, D.-C. and Abed, E. H., "Stabilization of tethered satellites during station keeping," *IEEE Transations of Automatic Control*, vol. 35, no. 11, pp. 1186–1196, 1990.

[32] Licata, R., "Tethered system deployment controls by feedback fuzzy logic," *Acta Astonautica*, vol. 40, no. 9, pp. 619–634, 1997.

[33] Liu, Q. and Wie, B., "Robust time-optimal control of uncertain flexible spacecraft," *Journal of Guidance, Control, and Dynamics*, vol. 15, no. 3, pp. 597–604, 1992.

[34] Lorenzini, E. C., Cosmo, M. L., Kaiser, M., Bangham, M. E., Vonerwell, D. J., and Johnson, L., "Mission analysis of spinning systems for transfers from low orbits to geostationary," *Journal of Spacecraft and Rockets*, vol. 37, no. 2, pp. 165–170, 2000.

[35] Mazzoleni, A. P. and Hoffman, J. H., "Planar attitude dynamics of the end-bodies of a tethered satellite system during spin-up," in *AIAA/AAS Space Flight Mechanics Meeting*, 2001.

[36] Mazzoleni, A. P. and Hoffman, J. H., "Effect of damping on planar spin-up dynamics of artificial-gravity-generating tethered satellite system," in *14th AAS/AIAA Space Flight Mechanics Mechanics Conference*, (Maui, HI), 2004.

[37] Mills, B. W., Singhose, W. E., and Seering, W. P., "Closed-form generation of specified-fuel commands for flexible systems," in *American Control Conference*, (Philadelphia, PA), 1998.

[38] Misra, A. K. and Modi, V. J., "Deployment and retrieval of shuttle supported tethered satellites," *Journal of Guidance*, vol. 5, no. 3, 1982.

[39] Modi, V. J., Gilardi, G., and Misra, A. K., "Attitude control of space platform based tethered satellite system," *Journal of Aerospace Engineering*, vol. 11, no. 2, pp. 24–31, 1998.

[40] Murphy, B. R. and Watanabe, I., "Digital shaping filters for reducing machine vibration," *IEEE Transactions on Robotics and Automation*, vol. 8, no. April, pp. 285–289, 1992.

[41] Netzer, E. and Kane, T. R., "Deployment and retrieval optimization of a tethered satellite system," *Journal of Guidance, Control and Dynamics*, vol. 16, no. 6, pp. 1085–1091, 1993.

[42] Nohmi, M., Nenchev, D. N., and Uchiyama, M., "Tethered robot casting using a spacecraft-mounted manipulator," *Journal of Guidance, Control and Dynamics*, vol. 24, no. 4, pp. 827–833, 2001.

[43] Pao, L. Y. and Singhose, W. E., "Verifying robust time-optimal commands for multi-mode flexible spacecraft," *AIAA J. of Guidance, Control, and Dynamics*, vol. 20, no. 4, pp. 831–833, 1997.

[44] Pao, L. Y. and Singhose, W. E., "Robust minimum time control of flexible structures," *Automatica*, vol. 34, no. 2, pp. 229–236, 1998.

[45] Pascal, M., Djebli, A., and Bakkali, L. E., "Laws of deployment/retrieval in tether connected satellites systems," *Acta Astonautica*, vol. 45, no. 2, pp. 61–73, 1999.

[46] Pelaez, J. and Lorenzini, E. C., "Sensitivity analysis of tether-mediated orbital injection," *The Journal of the Astronautical Sciences*, vol. 44, no. 4, pp. 491–514, 1996.

[47] Pelaez, J., Lorenzini, E. C., Lopez-Rebollal, O., and Ruiz, M., "A new kind of dynamic instability in electrodynamic tether," *The Journal of the Astronautical Sciences*, vol. 48, no. 4, pp. 449–476, 2000.

[48] Pelaez, J., Ruiz, M., Lopez-Rebollal, O., Lorenzini, E. C., and Cosmo, M. L., "Two-bar model for the dynamic and stablility of electrodynamic tethers," *Journal Guidance, Control, and Dynamics*, vol. 25, no. 6, pp. 1125–1135, 2002.

[49] Pines, D. J., Flotow, A. H. v., and Redding, D. C., "Two nonlinear control approaches for retrieval of a thrusting tethered subsatellite," *Journal of Guidance*, vol. 13, no. 4, pp. 651–658, 1990.

[50] Pradhan, S., Modi, V. J., and Misra, A. K., "On the inverse control of the tethered satellite system," *The Journal of the Astronautical Sciences*, vol. 43, no. 2, pp. 179–193, 1995.

[51] Robertson, M. and Singhose, W., "Initial guess schemes for generating deflection-limiting commands," in *AAS/AIAA Astrodynamics Specialist Conference*, (Girdwood, AK), 1999.

[52] Robertson, M. and Singhose, W., "Generating deflection-limiting commands in the digital domain," in *AAS/AIAA Astrodynamics Specialist Conference*, (Quebec City, Quebec), 2001.

[53] Robertson, M. and Singhose, W., "Multi-level optimization techniques for designing digital shapers," in *American Control Conference*, (Pittsburgh, PA), 2001.

[54] Rogers, K. and Seering, W. P., "Input shaping for limiting loads and vibration in systems with on-off actuators," in *AIAA Guidance, Navigation, and Control Conference*, (San Diego, CA), 1996.

[55] Roy, R. I. S., Hastings, D. E., and Ahedo, E., "Systems analysis of electrodynamic tethers," *Journal of Spacecraft and Rockets*, vol. 29, no. 3, pp. 415–424, 1992.

[56] Ruiz, M. and Pelaez, J., "On the deployment of a tether from an elliptical orbit," *The Journal of the Astronautical Sciences*, vol. 46, no. 2, pp. 119–133, 1998.

[57] Ruiz, M., Pelaez, J., and Lorenzini, E. C., "On the stability of a tethered system with a free end in elliptic orbit," *The Journal of the Astronautical Sciences*, vol. 49, no. 2, pp. 237–253, 2001.

[58] Ruiz, M. and Pelaez, J., "Influence of a small end mass on tether-mediated orbit injection," *Journal of Spacecraft and Rockets*, vol. 24, no. 6, pp. 1108–1117, 2001.

[59] Singer, N. C. and Seering, W. P., "Preshaping command inputs to reduce system vibration," *Journal of Dynamics, Measurement, and Control*, vol. 112, no. March, pp. 76–82, 1990.

[60] Singhose, W., Banerjee, A., and Seering, W., "Slewing flexible spacecraft with deflection-limiting input shaping," *Journal of Guidance, Control, and Dynamics*, vol. 20, no. 2, pp. 291–298, 1997.

[61] Singhose, W., Derezinski, S., and Singer, N., "Extra-insensitive input shapers for controlling flexible spacecraft," *AIAA J. of Guidance, Control, and Dynamics*, vol. 19, no. 2, pp. 385–91.

[62] Singhose, W., Mills, B., and Seering, W., "Closed-form methods for generating on-off commands for undamped flexible structures," *Journal of Guidance, Control, and Dynamics*, vol. 22, no. 2, 1999.

[63] Singhose, W., Seering, W., and Singer, N., "Residual vibration reduction using vector diagrams to generate shaped inputs," *ASME Journal of Mechanical Design*, vol. 116, no. June, pp. 654–659, 1994.

[64] Singhose, W. and Singer, N., "Effects of input shaping on two-dimensional trajectory following," *IEEE Transactions on Robotics and Automation*, vol. 12, no. 6, pp. 881–887, 1996.

[65] Singhose, W., Singer, N., and Seering, W., "Time-optimal negative input shapers," *Journal of Dynamic Systems, Measurement, and Control*, vol. 119, no. June, pp. 198–205, 1997. journal.

[66] Singhose, W. E., Seering, W. P., and Singer, N. C., "Input shaping for vibration reduction with specified insensitivity to modeling errors," in *Japan-USA Symposium on Flexible Automation*, (Boston, MA), 1996.

[67] Smith, O. J. M., *Feedback Control Systems*. New York: McGraw-Hill Book Co., Inc., 1958.

[68] Sorensen, K., "Conceptual design and analysis of an mxer tether boost station," in *37th AIAA/ASME/SAE/ASEE Joint Propulsion Conference*, (Salt Lake City, UT), 2001.

[69] Steindl, A. and Troger, H., "Optimal control of deployment of a tethered subsatellite," *Nonlinear Dynamics*, vol. 31, pp. 257–274, 2003.

[70] Stoen, J. D. and Kane, T. R., "Spin augmented deployment and retrieval of tethered artificial gravity spacecraft," in *AIAA/AAS Space Flight Mechanics Meeting*, 1993.

[71] Tallman, G. H. and Smith, O. J. M., "Analog study of dead-beat posicast control," *IRE Transactions on Automatic Control*, no. March, pp. 14–21, 1958.

[72] Tragesser, S. and San, H., "Orbital maneuvering with electrodynamic tethers," *Journal Guidance, Control, and Dynamics*, vol. 26, no. 5, pp. 805–810, 2003.

[73] Tuttle, T. and Seering, W., "Deriving and verifying time-optimal commands for linear systems," in *American Control Conf.*, (Albuquerque, NM), 1997.

[74] Tuttle, T. D. and Seering, W. P., "A zero-placement technique for designing shaped inputs to suppress multiple-mode vibration," in *American Control Conference*, vol. 3, (Baltimore, MD), pp. 2533–2537, ACC, 1994.

[75] Vadali, S. R. and Kim, E. S., "Feedback control of tethered satellites using lyapunov stability theory," *Journal Guidance, Control, and Dynamics*, vol. 14, no. 4, pp. 729–735, 1991.

[76] Vas, I. E., Kelly, T. J., and Scarl, E. A., "Space station reboost wil electrodynamic tethers," *Journal of Spacecraft and Rockets*, vol. 37, no. 2, pp. 154–164, 2000.

[77] Yu, S., "Dynamic model and control of mass-distributed tether satellite system," *Journal of Spacecraft and Rockets*, vol. 39, no. 2, pp. 213–218, 2002.

[78] Zhu, R., Misra, A. K., and Modi, V. J., "Dynamics and control of coupled orbital and librational motion of tethered satellite systems," *The Journal of the Astronautical Sciences*, vol. 42, no. 3, pp. 319–342, 1994.